White Rose Research Online

eprints@whiterose.ac.uk
https://eprints.whiterose.ac.uk
Universities of Leeds, Sheffield and York

Deposited via The University of Sheffield.

White Rose Research Online URL for this paper:
https://eprints.whiterose.ac.uk/id/eprint/239890/

Version: Accepted Version

Article:
Sullivan-Allsop, S., Clark, N., Wang, W. et al. (2026) Atomic-resolution imaging of gold species at organic liquid-solid interfaces. Science, 392 (6793). pp. 77-82. ISSN: 0036-8075

https://doi.org/10.1126/science.adw2469

© 2026 The Authors. Except as otherwise noted, this author-accepted version of a journal article published in Science is made available via the University of Sheffield Research Publications and Copyright Policy under the terms of the Creative Commons Attribution 4.0 International License (CC-BY 4.0), which permits unrestricted use, distribution and reproduction in any medium, provided the original work is properly cited. To view a copy of this licence, visit http://creativecommons.org/licenses/by/4.0/

Reuse
This article is distributed under the terms of the Creative Commons Attribution (CC BY) licence. This licence allows you to distribute, remix, tweak, and build upon the work, even commercially, as long as you credit the authors for the original work. More information and the full terms of the licence here: https://creativecommons.org/licenses/

Takedown
If you consider content in White Rose Research Online to be in breach of UK law, please notify us by emailing eprints@whiterose.ac.uk including the URL of the record and the reason for the withdrawal request.

UNIVERSITY OF LEEDS
University of Sheffield
UNIVERSITY of York

Atomic-resolution imaging of gold species at organic liquid-solid interfaces

Sam Sullivan-Allsop[1,2*], Nick Clark[1,2*]†, Wendong Wang[2,3*], Rongsheng Cai[1], William Thornley[1], David G. Hopkinson[4], James McHugh[2,3], Ben Davies[5], Samuel Pattisson[6], Nicholas F. Dummer[6], Rui Zhang[1,2], Matthew Lindley[1], Gareth Tainton[1], Jack Harrison[1,2], Hugo De Latour[1,2], Joseph Parker[1,2], Joshua Swindell[1], Eli G. Castanon[2,3], Amy Carl[2,3], David Lewis[1], Natalia Martsinovich[7], Christopher S. Allen[4,8], Mohsen Danaie[4], Andrew J. Logsdail[6], Vladimir Falko[2,3], Graham J. Hutchings[5], Alex Summerfield[2], Roman Gorbachev[2,3,9]†, Sarah J. Haigh[1,2]†

[1]Department of Materials, University of Manchester; Manchester M13 9PL, UK

[2]National Graphene Institute, University of Manchester; Manchester M13 9PL, UK

[3]Department of Physics and Astronomy, University of Manchester; Manchester M13 9PL, UK

[4]ePSIC, Diamond Light Source, Harwell Science and Innovation Campus; Didcot OX11 0DE, UK

[5]Max Planck–Cardiff Centre on the Fundamentals of Heterogeneous Catalysis FUNCAT, Cardiff Catalysis Institute, School of Chemistry, Cardiff University, Cardiff, CF24 4HQ, UK

[6]Cardiff Catalysis Institute, School of Chemistry, University of Cardiff; Cardiff CF10 3AT, UK

[7]School of Mathematical and Physical Sciences, University of Sheffield; Sheffield S3 7HF, UK

[8]Department of Materials, University of Oxford; Oxford OX1 3PH, UK

[9]Henry Royce Institute for Advanced Materials, University of Manchester; Manchester M13 9PL, UK

* These authors contributed equally to this work.

† Corresponding author. e-mail:

nick.clark@manchester.ac.uk, roman@manchester.ac.uk, sarah.haigh@manchester.ac.uk

The structure and dynamics of adsorbed atoms (adatoms) at solid-liquid interfaces determines the performance of advanced catalysts, electrochemical devices, molecular separation technologies, and metal extraction from waste streams. However, in situ investigations of atomically dispersed metals in various chemical environments have been prevented by insufficient imaging resolution and solvent incompatibility. We combine a new specimen design that provides atomic resolution in liquid-phase electron microscopy with deep learning-enabled analysis to explore the interactions between gold adatoms, graphite support, and the solvent collectively. We tracked the locations of > 10^6 graphite-supported Au adatoms, dimers and larger clusters in five solvents. Although their initial atomic dispersion was determined by the solvent polarity, fast drying kinetics at low temperature were required for optimising catalytic performance.

The dynamics of adsorbed atoms (adatoms) at solid-liquid interfaces inform many key industrial processes, including deposition and evolution of single atom catalysts (SACs), separation and waste recovery of valuable metals, and electrode performance in electrochemical systems(*1-8*). For catalysis, atomically dispersed metal species combine the beneficial properties of both heterogenous and homogeneous catalysts, providing higher efficiency and greater selectivity with reduced metal loading compared to supported nanoparticle equivalents(*5, 6, 9-11*). For separation technologies, understanding their atomic scale interactions enables tuning of the diffusion processes(*12-18*), because many precious metal recovery routes rely on preferential atomic adsorption of metal ions to surface sites(*19-22*). In energy storage devices, understanding atomic scale electrochemical deposition, migration, and interfacial reactions at the electrode surfaces can guide improvements in efficiency, energy density, and cycling stability(*23-28*).

Transmission electron microscopy (TEM) can visualise individual atomic species on a range of different supports exposed to the TEM vacuum(*29-31*). Combining TEM with graphene liquid cells (GLCs) has greatly advanced atomically-resolved imaging of solid particles(*32-35*) and adatoms(*23, 36, 37*) at solid-liquid interfaces. However, current GLC studies are limited to aqueous solutions with poor control over the solution concentration, and typically only a small number of images are analysed(*38*). We report a new graphene liquid cell technology and apply it, together with artificial intelligence (AI) enabled analysis, to perform atomic-resolution imaging and single-adatom tracking in a variety of non-aqueous solvent environments.

We studied metal-support interactions during wet impregnation synthesis of gold atoms on carbon supports (Au-C). Specifically, we obtained fundamental insights into production of Au-C SACs, which have shown exceptional performance for acetylene (C_2H_2) hydrochlorination(*39, 40*), providing a safer alternative to the mercury-based catalysts for the production of vinyl chloride monomer polyvinyl chloride (PVC)-based polymers(*41*). Recent studies have showed that low-polarity organic solvents results in highly active atomically dispersed Au catalysts(*9*). Scanning transmission electron microscopy (STEM) observations of the final dry catalysts in vacuum qualitatively verified the presence of atomically dispersed metal species(*9, 39*). Characterising how the metal interacts with the solid in the liquid phase, which is then modified by the drying process to determine the final catalyst structure, could lead to a better mechanistic understanding of this reaction.

Our imaging methodology and analysis workflow allowed us to quantitatively compare the atomic dispersion of > 10^6 gold atoms on thin graphite in water and organic liquids such as acetone, ethanol, butanol, and cyclohexanone. We show that both solvent polarity and the subsequent drying process play crucial roles in the atomic dispersal and the resulting catalytic activity. We observed formation and evolution of stable dimer, trimer and larger clusters, opening the discussion of what role these more complex configurations play in the synthesis(*42*). This study also provides a statistically meaningful understanding of SAC formation, which is an essential input for predictive modelling to optimise catalytic synthesis.

GLC fabrication and imaging capabilities.

Studying atomic-scale solid-liquid processes for the wide variety of solvents relevant to wet catalytic processing requires expansion of the capabilities of the graphene liquid-cell TEM platform beyond aqueous chemistry. Organic solvents are incompatible with the polymeric supports ubiquitous in conventional transfer techniques(30, 43), so we have used silicon nitride membranes(44) as both the heterostructure transfer carrier and TEM sample support. The resulting experimental platform enables atomic-resolution imaging for organic solvents as well as many acids and alkaline solutions.

In previous graphene liquid cell studies, uncontrolled drying of the solution during the liquid cell fabrication increased the concentration of the encapsulated solution by up to 3 orders of magnitude(*38*). To mitigate this effect, we have developed a liquid bath transfer process, whereby the final "filling and sealing" step was performed under immersion in a bulk quantity of the target liquid, (**Fig. 1A**). This process offers greater control over the concentration of the encapsulated solution than previous methods(*38*). Furthermore, by using cleaner and more chemically and thermally stable silicon nitride membranes we removed the dominant sources for hydrocarbon contamination of the cells, resulting in extremely clean surfaces and interfaces(*30*).

The liquid cells comprise of thin graphite (3-5 nm) windows encapsulating a 30 to 40 nm thick hexagonal boron nitride (hBN) spacer, with pre-patterned holes in the spacer serving as the "wells" containing liquid (**Fig. 1B)**. The total cell thickness (36-50 nm) is thin enough for high-resolution STEM imaging and also allows us to image dynamics on only one thin graphite window at a time by making use of the limited depth-of-field. The thin and uniform layer of encapsulated liquid and thin graphite windows of our samples mean that, when imaged with a high spatial resolution STEM instrument, atomic resolution information was obtained in both high-angle annular dark-field (HAADF) and bright-field (BF) STEM images (Fourier ring correlation resolution of 0.129 and 0.152 nm respectively, see Figs. S16 and S17). A wide range of samples that can be characterised by the platform as both atomic number (Z) contrast (HAADF) and phase contrast (BF) STEM imaging modes can be accessed simultaneously. Full details of specimen preparation can be found in Supplementary Information (SI) section 3 including verification of the presence of trapped liquid by electron energy loss spectroscopy.

Gold adatom catalysts at the graphite-solvent interface

A compound HAADF/BF STEM image of a graphene liquid cell filled with a solution of acetone and 16 mM $HAuCl_4$ (**Fig. 1C)** demonstrates the strength of combining HAADF and BF STEM. We identified both the individual Au atomic species (shown as pink dots, mainly provided by the HAADF signal) and the underlying graphite lattice (shown as a regular mesh of purple dots, mainly provided by the BF phase contrast image). Raw BF and HAADF images and the compound image provided a good match to image simulations and lent confidence in our interpretation of the atomic structure of the catalyst (see inset in **Fig. 1C** and SI section 2 for further details).

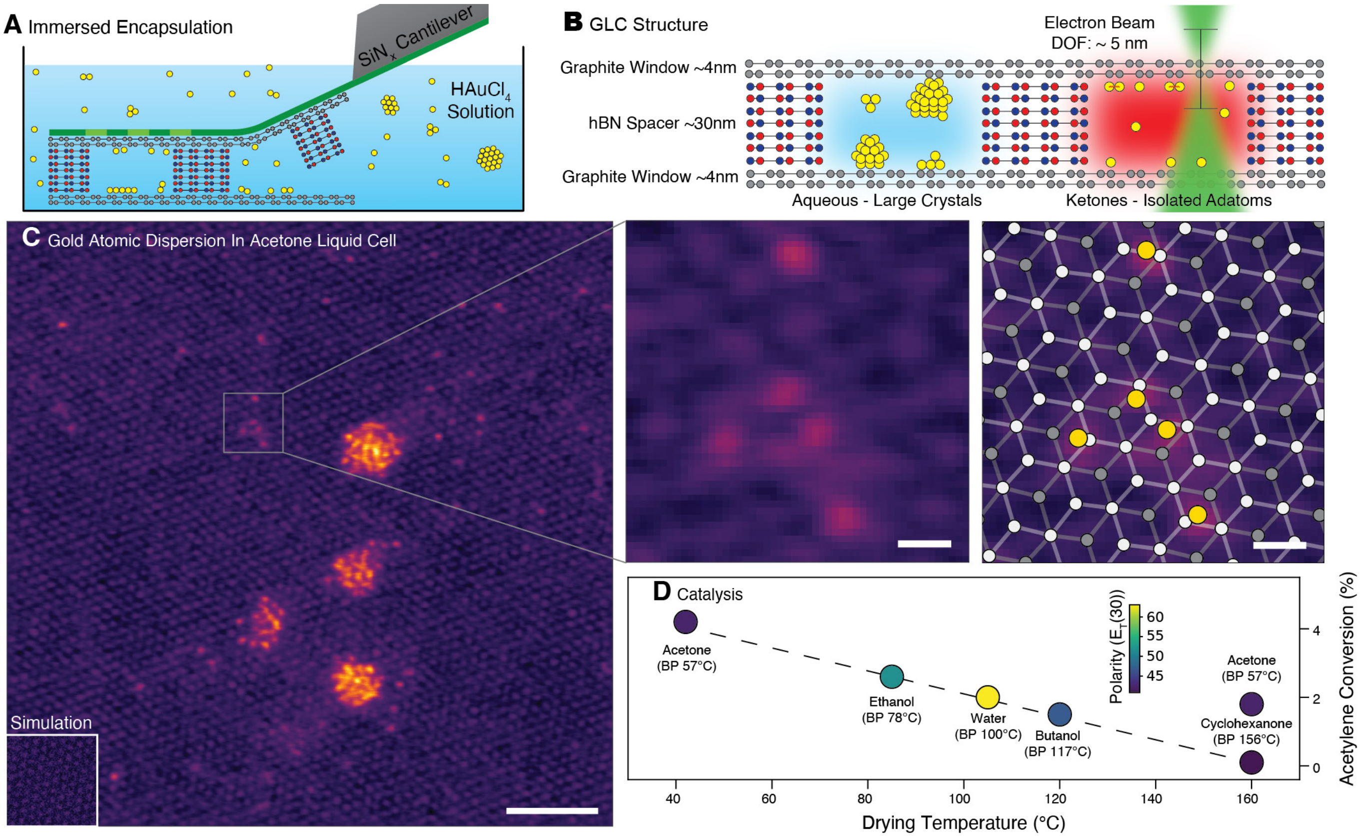

Figure 1: Gold adatoms at the graphite-solvent interface. *(A) Schematic of the fabrication of the graphene liquid cell (GLC) using a Si/SiNx cantilever. (B) Schematic cross section of the GLC structure. The thickness of each of the graphite windows is 3-5nm, while the thickness of the hBN spacer is chosen to be 30—40 nm to control the thickness of the encapsulated liquid. (C) Combined HAADF-STEM and BF-STEM micrographs of the final GLC containing atomically dispersed gold on the graphite lattice in contact with liquid acetone. Only one window is in focus due to the limited depth of field of the STEM probe. The inset in the bottom left of the image shows a simulated image of a graphite window at the same scale. The right top panel shows an enlarged area of the image in C highlighted by the grey square. Right lower panel is the measured positions of the gold (yellow) and the graphite lattice (alternative AB stacked graphene layers in white and grey) from the selected location. Data has been denoised to improve SNR as described in SI section 4. (D) Initial acetylene conversion and polarity values for Au/graphite catalysts prepared by wet impregnation in acetone, ethanol, butanol, cyclohexanone, and water (see SI section 6 for further details). Scalebars in (C) left: 2 nm, right: 200 pm.*

The Au adatoms we observed were adsorbed onto the thin graphite window and freely diffuse across it, while those in solution move too fast to be resolved (videos and image series are provided in SI section 1). The ability to simultaneously resolve both metal adatoms and graphite lattice allowed us to map out the position of the gold adatoms with respect to the graphite lattice sites, as shown for the enlarged region in **Fig. 1C**. In previous TEM graphene liquid-cell imaging, the liquid background and relatively weak electron signal from carbon atoms prevented resolving the lattice carbon sites for metal adsorbed on the graphene window (see Figs. S1-4)(*33, 45*).

Along with atomically dispersed species, amorphous clusters of Au ranging from few-atom to a few nanometres in diameter (**Fig. 1C**), were also observed in the GLC, as well as several larger crystalline particles (see Fig. S5). In contrast, when the GLC is filled with water instead of acetone and the same 16 mM concentration of $HAuCl_4$ gold salt, no atomically dispersed Au species were observed. The Au was only present as large crystalline nanoparticles with diameters >5 nm (Fig. S5). The absence of any atomically resolved Au species in the aqueous GLC explains the poor catalytic function of the Au-C catalysts synthesised with water for acetylene hydrochlorination, as this reaction is thought to depend on the presence of isolated adatoms(*39, 40*) (**Fig. 1D**). Indeed, the aqueous Au-C catalyst resulted in conversion values equal to the graphite support with no Au.

We attributed the atomic dispersion of the gold in acetone solvent to the much lower polarity of acetone over water, leading to stronger Coulomb repulsion of gold ions in bulk liquid. However, this explanation raises the question of why cyclohexanone is not a similarly effective solvent for wet impregnation synthesis of Au-C SAC, having similar chemical functionality and polarity to acetone, but generating Au-C catalysts with no activity towards acetylene hydrochlorination (**Fig. 1D,** see SI section 6 for further details of catalytic testing). Furthermore, the catalyst activity depended not only on the solvent used during synthesis but also on the drying temperature, with acetone dried at 42°C providing much higher activity for acetylene conversion when dried at room temperature than when dried at 160°C (**Fig. 1D**).

AI-enabled image analysis

To quantify the differences in the distribution of Au atomic species on graphite in contact with the acetone and cyclohexanone, we have compared more than 4,000 HAADF- and BF-STEM images for GLCs in both solvents. A semi-automated, AI-enabled image-analysis methodology was used that located Au species and assigned them to clusters based on a cut-off search radius of 0.4 nm (full details in SI section 4). Example HAADF STEM images of such clusters with their assigned number of atomic species (n) in acetone and cyclohexanone are shown **Fig. 2A**. Quantification of the cluster size distributions for acetone and cyclohexanone (**Fig. 2B)** was based on measurement of >5,000 clusters for each solvent. Although STEM imaging is a two-dimensional (2D) projection, the Z contrast dependence of the HAADF image enabled estimation of the local thickness of the gold cluster that was calibrated on the intensity of a single atom(*46-48*) (see Fig. S22).

The acetone and cyclohexanone atomic species follow the distribution expected for a random dispersion (black line on **Fig. 2B**) up to three atoms. For more than three atoms, the probability of finding the Au sites together in a cluster increased significantly compared to a random distribution, demonstrating the earliest stages of solid nanoparticle nucleation. Both solvents showed a plateau in the probability of nanoparticle occurrence around n=30, corresponding to diameters of ~1.1 nm, with both acetone and cyclohexanone falling off at higher values of n. We therefore categorised locations with $4 \leq n \leq 30$ atomic sites as "small amorphous clusters," $n \geq 31$ as "large amorphous clusters," and any particles with a regular atomic arrangement as "crystalline particles." The latter were found for diameters > 1.1 nm and feature a 3D morphology, whereas the amorphous clusters were much flatter (**Fig. 2A**). Notably, no systematic changes in the atomic distributions or structure in the acetone or cyclohexanone GLCs were observed for samples produced and imaged after different periods of time (Fig. S23), suggesting a steady state was present at the solid-liquid interface. In contrast, in the aqueous systems, the crystalline particles were qualitatively observed to be larger if more time had elapsed between preparation and imaging.

The probability of observing an adatom in a cluster of a certain size for the different solvents (**Fig. 2C)** reveals that cyclohexanone has a significantly larger number of crystalline nanoparticles, with 72% contributing to these compared to 8% in acetone. The remaining atoms in both acetone and cyclohexanone had a roughly equal ratio of isolated species to amorphous clusters with the mean cluster size, $\bar{n}$, also smaller in acetone, $\bar{n}$=21, compared to cyclohexanone, $\bar{n}$=25. Overall, the total Au found to be atomically dispersed was much larger for the acetone solvent (42%), versus only 12% for cyclohexanone (for details see SI section 5.2). This observation helped to explain the difference in their catalytic performance (**Fig. 1D**). For the same Au concentration in higher polarity solvents (ethanol and butanol), a much higher proportion of the Au was present as crystalline nanoparticles (80% and 87 %) for ethanol and butanol, respectively (**Fig. 2C**).

We used the calculated total amount of Au for the full area imaged to estimate the concentration of Au in the liquid cell. Assuming the cell had a uniform thickness of 30 nm and most of the ions were adsorbed to one of the two thin graphite windows, we obtained a solution concentration of ~30 mM for both acetone and cyclohexanone, which was ~2 times greater than the bulk solutions nominal value. The difference is likely caused by preferential adsorption of Au adatoms on the graphite surface in the bulk solution prior to cell closure, resulting in the graphite surface "storing" a larger number of atoms than can be nominally contained in the GLC solvent. Thus, the studied system was a "snapshot" of the bulk-interface equilibrium, compared to previous drying-based encapsulation techniques where the solute density was unreliable(*36, 38*).

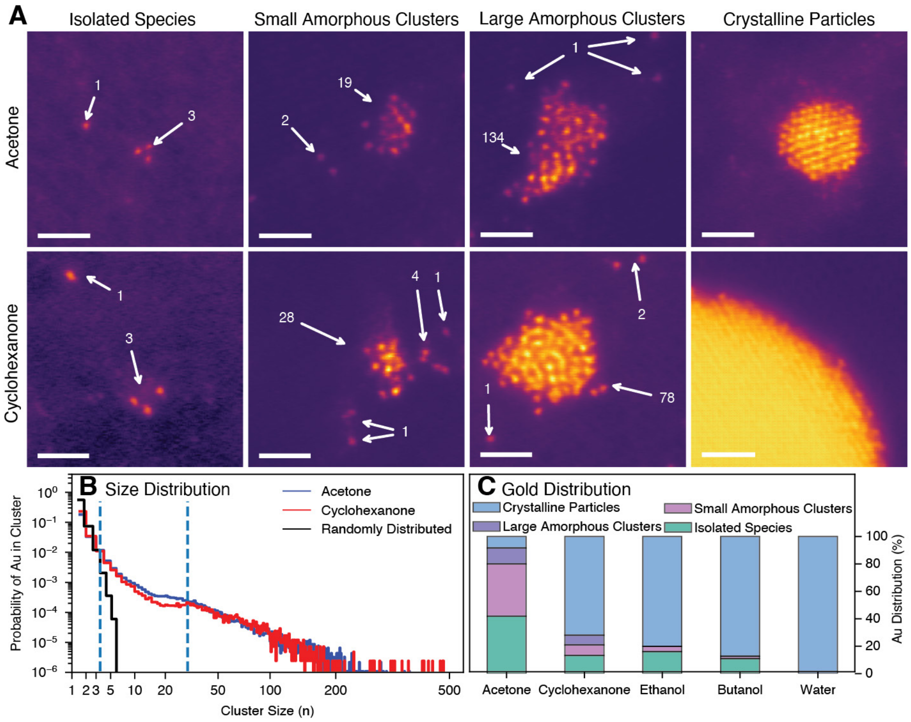

Figure 2: Quantification of gold structures inside the GLCs. *(A) HAADF STEM images showing the structural states of the gold within the acetone and cyclohexanone solutions (isolated species, amorphous cluster and crystalline particles). The assigned number of atomic sites for each cluster, n, visible in these example images is indicated (showing n=1,2,3,19,134 for acetone and n=1,2,3,4,28, and 78). (B) Size distributions of the gold species and their corresponding areal density. The vertical lines at n = 3 and 30 correspond to the separation of the categories of isolated species, small amorphous and large amorphous clusters. (C) Proportions of the total measured gold existing in each structural state for acetone, cyclohexanone, ethanol, butanol and water. Scalebars in (A) are 1 nm.*

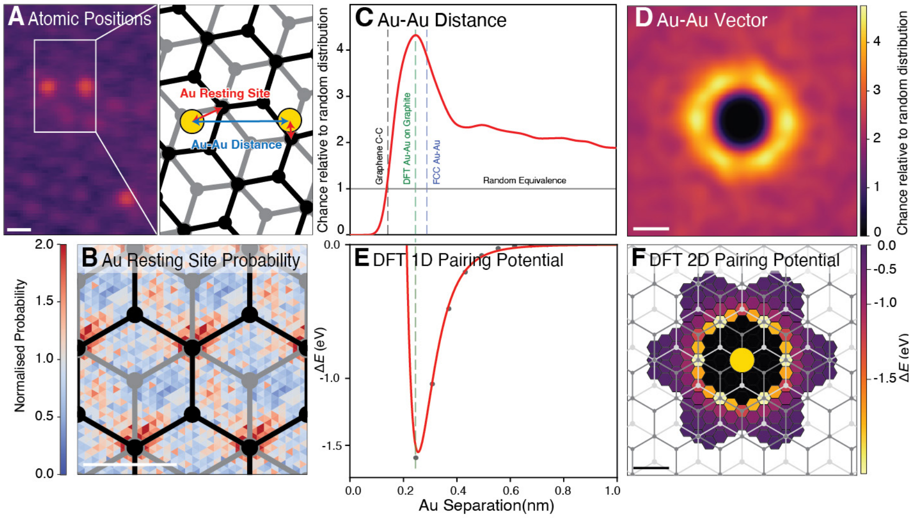

Figure 3: Gold adatom-adatom-substrate interactions. *(A) Left: a cropped region of a combined HAADF/BF STEM image. Right: schematic of the atomic positions, and the Au resting site and the Au-Au distances for the location highlighted by the white rectangle (the graphite sublattices are shown in black and grey, and the gold adatoms in yellow). (B) The Au adatom resting site probability on the graphite lattice within an acetone environment, with the lattice stucture overlaid. (C) Au-Au 1D pair distribution function (PDF) relative to a random distribution for the isolated Au species in acetone filled GLCs. The graphene carbon-carbon separation, DFT predicted stable Au-Au distance on graphite(49) and the the face-center cubic crystal Au-Au bond length(54) are plotted as dashed lines for reference. Inset shows the PDF at larger Au-Au separation distances. (D) Au-Au 2D PDF relative to the random distribution for the isolated Au species in acetone liquid filled GLCs. The isolated species are characterised by n= 1,2 or 3. (E) DFT calculation of potential energy for dimer as a function of Au-Au separation on graphite, with one gold atom fixed at the* A_1 *site and with the other moving along the zig-zag direction (C and E have a shared x-axis). (F) The DFT potential energies for the second gold atom placement in different sites on the graphite lattice, when the first gold atom is in the most energetically favourable* A_1 *position. The graphene lattices are overlaid in light and dark grey, and the gold atom in yellow. All the scalebars are 200 pm.*

Gold adatom structures on graphite

We analysed the preferred resting sites of gold adatom on the graphite surface (**Fig. 3A**). Our density functional theory (DFT) analysis as well as earlier studies indicate that four preferential adhesion sites exist for gold on graphite in vacuum(*49, 50*): A_1, atop the carbon atom for the sublattice where there is another carbon immediately beneath it; A_2, atop the carbon atom where there is no carbon in the layer directly beneath it; B (bridge), in the middle of the C-C bond; and H (hollow), in the centre of the carbon hexagon. By comparing experimental data from 3,365 gold adatom positions (determined from HAADF images) to the nearest identified carbon column position (from the simultaneously acquired BF images), we plot 2D histograms showing the experimental probability of finding a gold adatom at a specific resting location relative to graphene's unit cell (**Fig. 3B**).

In both acetone and cyclohexanone, there was a strong preference for Au to occupy the A_1 site, with all other locations being equally less likely to occur. While this is of lesser catalytic importance for this specific Au/C system, more broadly in catalysis this is important for determining the coordination and activity(*51-53*). To exclude sample tilt as a variable, a control simulation verified that tilt was < 2°, as no changes were observed in image features or resting site patterns (see Fig. S10). This experimental observation agreed with our DFT calculations that predicted A_1 is the most favourable resting site, but disagreed with an earlier DFT study that predicted both A_1 and A_2 to have similar binding energies(*49*). The difference can be attributed to the absence of solvent molecules in the DFT problems solved.

We observed that isolated gold species exhibited strong collective interactions. Almost half of the Au adatoms in acetone were in dimers or trimers. These metastable formations were seen for extended periods of time (minutes) and diffused in the flat configuration across the graphite surface. Dimers have been recently suggested to be particularly effective "correlated" SACs(*42*). We analysed adatom-adatom distances using 1D radially-averaged pair-distribution functions (normalised by a simulated random distribution) (**Fig. 3C;** see SI section 4 for further details). A strong preference existed for pairing with an Au-Au distance of 0.25 nm, matching the next-nearest-neighbour distance of the graphite lattice (peak in **Fig. 3C** and brightest ring feature in **Fig. 3D**).

This result generally agreed with our DFT calculations in vacuum, which showed large, ~2 eV, favourable gold dimer formation energies arising from both gold-gold and gold-graphite interactions (see SI Section 7). In our model, Au-Au pair formation energy peaked when both gold atoms are situated in adjacent A_1-A_1 sites, with second most preferred being the A_1-A_2 configuration before it decayed according to $\sim r^{-3}$ for a dimer length r (**Fig. 3E**). Negligible charge transfer occurred between gold adatoms and graphite, indicating that the gold ions present in bulk liquid most likely become neutral upon adsorption onto the graphite surface. This result was also confirmed by the remarkable stability of the dimers under electron beam irradiation, which would separate by Coulomb repulsion if the gold adatoms bore substantial charge (see SI section 5.3 and 10 for further consideration of electron beam effects).

We further analysed the directionality of the observed dimers using the 2D pair distribution function aligned relative to the underlying graphene lattice. A 6-fold rotational symmetry was observed at the A_1-A_1 configurations, with a noticeable azimuthal spread towards the adjacent A_1-A_2 and A_1-H configurations (**Fig. 3D**). These results were in good agreement with DFT-calculated 2D dimer formation energy map (**Fig. 3F).**

The amorphous clusters showed the same peak Au-Au interatomic distance as the isolated adatoms (0.25 nm) confirming that their interaction is more similar to that of isolated species (see Fig. S27), rather than crystalline face-centred cubic nanoparticles, which have larger peak interatomic distances (0.29 nm for imaging along the [111] plane)(*54*). Additional peaks were observed at larger interatomic distances approximately corresponding to the later nearest neighbours. The influence of the graphite support was less apparent in the angular distribution of the cluster data, likely because of the competing influence from the larger number of Au adatoms.

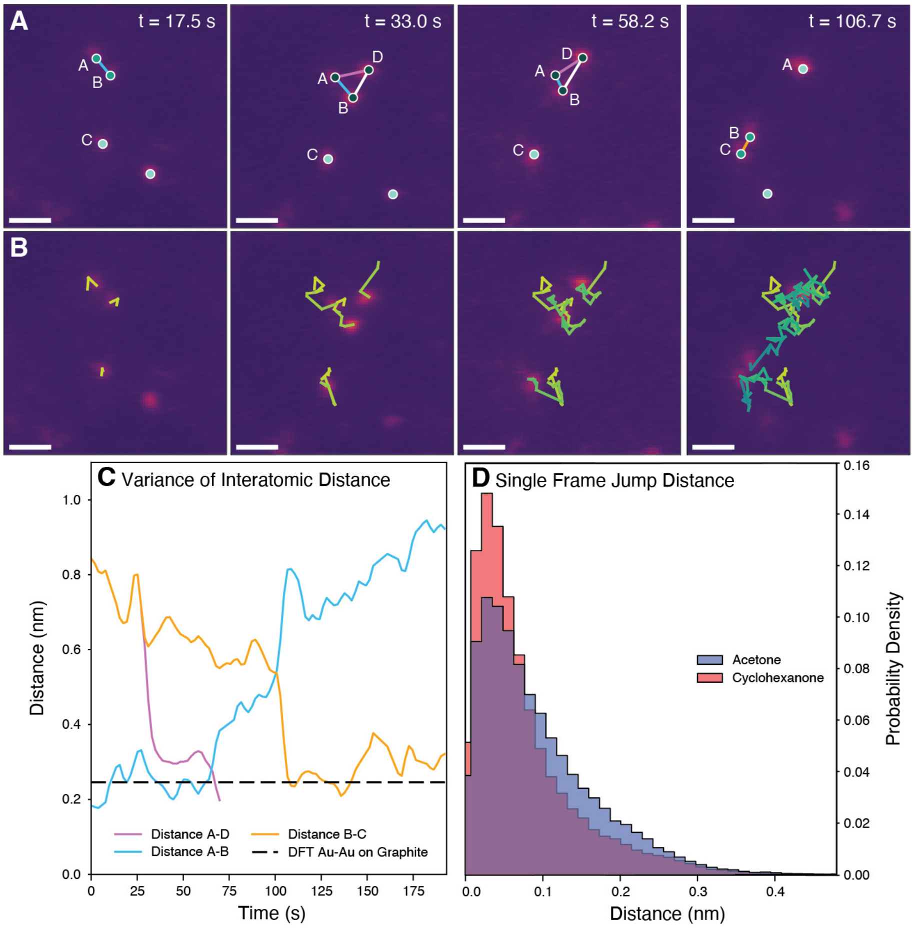

Figure 4: Gold adatom dynamic interactions. *(A,B) HAADF-STEM images from a video sequence of the gold adatoms in acetone at times of 17.5, 33.0, 58.2, and 106.7 s. (A) Highlighted locations of the Au adatoms, showing the transitions between monomer, dimer and trimer states. (B) Highlighted traces of the movement of the gold adatoms over the time period shown (coloured yellow to blue with increasing time). (C) The interatomic distances from (A) shown over the entire video sequence, AB (blue), BC (orange) and AD (purple). The black dashed line indicates the DFT Au-Au on graphite bond distance(49). (D) Single-frame adatom displacement histogram for Au in liquid GLC environments of acetone and cyclohexanone. All scalebars are 400 pm.*

Gold species dynamics and diffusion

The dimers, trimers, and larger clusters in the liquid cells were highly dynamic. We acquired video sequences of ~100 HAADF/BF STEM images (~1.8 s per frame, see Movies S1 and S2) and linked the nearest neighbours into atomic trajectories (further details in SI section 4). The Au adatoms diffused on the graphite surface, transitioning between monomer, dimer, and trimer configurations interchangeably, as can be seen in **Fig. 4A,B**. Adatoms also disappear from the field of view, either because of desorption into the solution or migration outside the imaged area in a single frame. Analysis of the interatomic distances as a function of time (**Fig. 4C**) highlights the dynamic nature of the process, although the preferred Au-Au spacing on graphite of 0.25 nm was again visible as the baseline interatomic distance (dashed line in **Fig. 4C**). Both acetone and cyclohexanone showed dynamic interplay between different atomic configurations in the isolated adatom species, but no structural changes in the gold developed over time during the imaging (SI section 5.4).

Quantification of frame-to-frame jump distances revealed that the distribution of frame-to-frame displacements in acetone was broader than the cyclohexanone, with larger jump distances more common in acetone (**Fig. 4D**). A control experiment at a lower electron flux confirmed that the reduction of the flux (by about an order of magnitude) had a negligible effect of the single-frame jump distances (see Fig. S39). Variations in the contrast caused by contamination across the window had a negligible impact upon the single-frame jump distances (see Fig. S29).

Atomistic simulations revealed that both acetone and cyclohexanone molecules adsorbed onto the graphene surface, with the first solvation shell of both solvents oriented parallel to the surface(*55*). Our simulations have shown that, for both cyclohexanone and acetone, the adsorption of the solvent molecules was preferable to the adsorption of Au species, but the adsorption of the Au-solvent pairs was even more favourable. Isolated adsorbed Au species and small clusters would be capped by solvent, which would stabilize them and prevent large cluster growth. When the organic solvents were replaced by water, our calculations showed that Au was more likely to adsorb on graphene than water, consistent with the observed formation of Au crystals in water-filled liquid cells (see SI section 7 for full details of our DFT calculations).

Imaging atomic species at the solvent-solid interface allows the separation of the liquid-phase adhesion step from the drying step for mechanistic understanding and prediction of the final structure for heterogeneous catalyst synthesis with wet chemical techniques. **Fig. 5** compares the relative areal densities for isolated monomer, dimer, and trimer adatoms in the acetone and cyclohexanone liquid cells with those for dried controls. Dried controls were prepared with the GLC approach but without a top graphene window and dried in air under ambient conditions. Statistically relevant measurements were obtained from 1000s of ex situ HAADF/BF STEM images of the catalyst, analysing > 1,000,000 isolated gold adatom positions (further details in SI section 4). This number of measurements is notable because even conventional ex situ TEM imaging (in vacuum) of SAC atomic assemblies typically only considers tens of atomic sites(*5, 6, 39, 56*) and with the previous largest ex situ analysis having considered up to 20,000 adatom positions(*31*). The dry samples retained their atomic dispersion when stored at ambient conditions for >6 months, likely because residual solvents stabilised the isolated Au (see Fig. S37). Neither solvent showed any change in the atomic coordination for the clusters after drying, with the same 0.25 nm peak preferred Au-Au interatomic distance observed for all samples, suggesting that this result was independent of the presence of solvent and dominated by adatom-substrate interactions (Fig. S24).

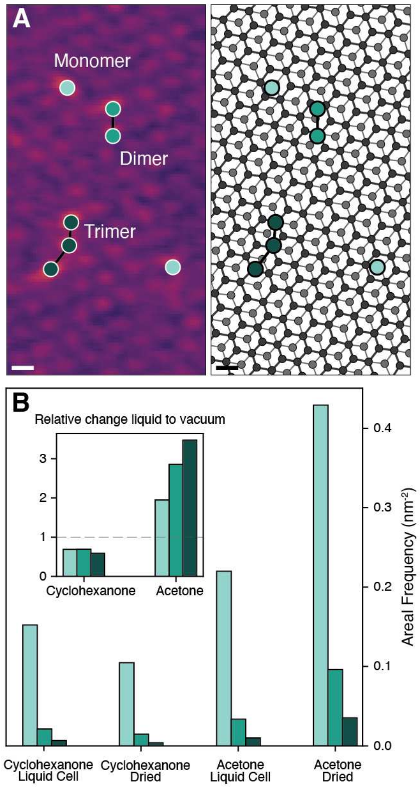

Figure 5: Atomic dispersion of Au on graphite with and without solvent. *(A) Combined HAADF & BF STEM image (left) and corresponding schematic (right) showing the measured graphene lattice and Au adatom positions. Examples of monomer, dimer and trimer configurations are indicated. (B) Areal Frequency (nm^{-2}) of monomer, dimer, and trimer gold adatom formations on the graphite surface in the cyclohexanone and acetone liquid cells and for the graphite support after drying (measured by conventional ex situ imaging in the TEM vacuum). The inset shows the relative change liquid to vacuum for both solvents. Scalebars in (A) are 200 pm. Data for ethanol and butanol liquid cells is shown in SI Fig. S28.*

Fig. 5B shows that although the acetone liquid cells have a proportionally higher areal density of all atomically dispersed species than cyclohexanone liquid cells, both have similar ratios of the areal frequency of monomer: dimer: trimer of 82±4: 13±3: 4±1. After drying, the areal density of isolated gold adatoms almost doubled for the acetone solvent compared to in the GLC. Monomer species increased by a factor of 2, dimers by a factor of 3 and trimers by a factor of 4, with the larger relative increase in dimers and trimers assigned simply to the greater density of atomic species on the support. This result showed that drying the Au in the acetone solvent at room temperature 40°C (compared to its boiling point of 57°C) has preserved the atomic dispersion brought about by the adatom-solvent-support interactions and provided an active SAC material (**Fig. 1D**). In contrast, drying at 160°C led to lower activity, as the increased temperature drove off the solvent and provides energy needed for the gold to aggregate into larger particles (Fig. S30).

For cyclohexanone, the opposite trend was observed. The number of atomically dispersed species decreasing by 30% after drying at room temperature, and the Au content instead formed larger Au clusters and crystalline particles. These particles were visible at the edge of liquid droplets (see Fig. S38) demonstrating the potential of drying processes like the coffee ring effect(*57, 58*) to destroy the favourable atomic dispersion formed by solvent interactions. Drying was a less important step when water was used as the solvent because the poor activity resulted from the absence of atomic dispersion in the liquid state. Thus, the effect of the drying temperature is simply to induce further agglomeration of Au.

As the binding affinities of the Au(I) to acetone and cyclohexanone are similar, we attributed the difference in the drying to acetone's lower boiling point and lower surface tension compared to cyclohexanone. The more rapid evaporation of the acetone solvent preserved the favourable atomic dispersion of the organic liquid-solid interface even at room temperature. Drying at higher temperatures has previously been used as a route to suppress the coffee ring effect but the increased temperature also provides energy to induce nanoparticle nucleation and growth, lowering the availability of atomically dispersed species that drive high activities(*59*). This latter effect is what we observe with the reduced activity shown in **Fig. 1D** and Fig. S31). The key to wet synthesis of an atomically dispersed Au catalyst was the combination of acetone's low boiling point with its low polarity that enabling the favourable atomic dispersion achieved in the liquid phase (42%) to be preserved during drying to form the synthesised catalyst with exceptionally high efficiency of active sites (54% of the active metal present as atomic species).

Summary and outlook

Our graphene liquid cell fabrication method enabled atomic resolution studies of the solid-liquid interface for non-aqueous solvents. We demonstrated the ability to encapsulate a known volume and concentration of liquid allowing quantitative comparison of the distribution of gold into atomic species, amorphous clusters, and nanoparticles in the liquid phase for five common solvents. We further revealed statistically representative quantification of the resulting metal configurations and dynamics at the solvent-graphene interface for Au-C SACs, using > 1 million identified adatom locations.

We observed complex correlations emerging from interactions between adatoms, their substrate, and the surrounding environment. The relative areal densities for isolated Au adatoms on graphite in acetone and cyclohexanone were similar. However, differences in their boiling points and surface tension caused a 5-fold difference in the isolated species synthesised through drying (0.12 atoms nm^{-2} for the dried cyclohexanone versus 0.56 atoms nm^{-2} for the acetone).

Our results demonstrate new capabilities to understand the solvent environment during wet impregnation synthesis, helping separate the contributions of solvent dispersion and drying conditions for optimising synthesis of catalysts with high stability and activity. We present a characterisation platform that enables representative atomic resolution imaging of dynamic structures in liquids for known solute concentrations, and across a wide range of important solvents. The new tool may benefit the development of materials for applications in catalysis, metal recovery from e-wastes, healthcare, and clean energy systems.

References and Notes

1. W. Gao, Z. D. Hood, M. Chi, Interfaces in Heterogeneous Catalysts: Advancing Mechanistic Understanding through Atomic-Scale Measurements. *Acc. Chem. Res.* **50**, 787-795 (2017). doi:10.1021/acs.accounts.6b00596.
2. Y. Yuan, K. Amine, J. Lu, R. Shahbazian-Yassar, Understanding materials challenges for rechargeable ion batteries with in situ transmission electron microscopy. *Nat. Commun.* **8**, 15806 (2017). doi:10.1038/ncomms15806.
3. A. Kosari, H. Zandbergen, F. Tichelaar *et al.*, Application of In Situ Liquid Cell Transmission Electron Microscopy in Corrosion Studies: A Critical Review of Challenges and Achievements. *Corrosion* **76**, 4-17 (2019). doi:10.5006/3369.
4. F. M. Alcorn, P. K. Jain, R. M. van der Veen, Time-resolved transmission electron microscopy for nanoscale chemical dynamics. *Nat. Rev. Chem.* **7**, 256-272 (2023). doi:10.1038/s41570-023-00469-y.
5. A. Wang, J. Li, T. Zhang, Heterogeneous single-atom catalysis. *Nat. Rev. Chem.* **2**, 65-81 (2018). doi:10.1038/s41570-018-0010-1.
6. X. F. Yang, A. Wang, B. Qiao *et al.*, Single-atom catalysts: a new frontier in heterogeneous catalysis. *Acc. Chem. Res.* **46**, 1740-1748 (2013). doi:10.1021/ar300361m.
7. Y. Li, Y. Li, A. Pei *et al.*, Atomic structure of sensitive battery materials and interfaces revealed by cryo-electron microscopy. *Sci* **358**, 506-510 (2017). doi:10.1126/science.aam6014.
8. F. Li, J. Zhu, P. Sun *et al.*, Highly efficient and selective extraction of gold by reduced graphene oxide. *Nat. Commun.* **13**, 4472 (2022). doi:10.1038/s41467-022-32204-4.
9. X. Sun, S. R. Dawson, T. E. Parmentier *et al.*, Facile synthesis of precious-metal single-site catalysts using organic solvents. *Nat. Chem.* **12**, 560-567 (2020). doi:10.1038/s41557-020-0446-z.
10. E. D. Boyes, A. P. LaGrow, M. R. Ward, R. W. Mitchell, P. L. Gai, Single Atom Dynamics in Chemical Reactions. *Acc. Chem. Res.* **53**, 390-399 (2020). doi:10.1021/acs.accounts.9b00500.
11. E. D. Boyes, P. L. Gai, Visualizing Dynamic Single Atom Catalysis. *Adv. Mater.* **36**, e2314121 (2024). doi:10.1002/adma.202314121.
12. H. Wang, Y. Zhai, Y. Li *et al.*, Covalent organic framework membranes for efficient separation of monovalent cations. *Nat. Commun.* **13**, 7123 (2022). doi:10.1038/s41467-022-34849-7.
13. X. Li, J. Liu, R. Qu *et al.*, Universal and tunable liquid-liquid separation by nanoparticle-embedded gating membranes based on a self-defined interfacial parameter. *Nat. Commun.* **12**, 80 (2021). doi:10.1038/s41467-020-20369-9.
14. Y. Jiang, R. Hu, C. Yang *et al.*, Surface diffusion enhanced ion transport through two-dimensional nanochannels. *Sci. Adv.* **9**, eadi8493 (2023). doi:10.1126/sciadv.adi8493.
15. T. Emmerich, K. S. Vasu, A. Nigues *et al.*, Enhanced nanofluidic transport in activated carbon nanoconduits. *Nat. Mater.* **21**, 696-702 (2022). doi:10.1038/s41563-022-01229-x.
16. F. Liou, H. Z. Tsai, Z. A. H. Goodwin *et al.*, Gate-Switchable Molecular Diffusion on a Graphene Field-Effect Transistor. *ACS Nano* **18**, 24262-24268 (2024). doi:10.1021/acsnano.4c05808.

17. X. Lin, J. C. Lu, Y. Shao *et al.*, Intrinsically patterned two-dimensional materials for selective adsorption of molecules and nanoclusters. *Nat. Mater.* **16**, 717-721 (2017). doi:10.1038/nmat4915.
18. J. Peng, D. Cao, Z. He *et al.*, The effect of hydration number on the interfacial transport of sodium ions. *Nature* **557**, 701-705 (2018). doi:10.1038/s41586-018-0122-2.
19. B. Feng, C. Yao, S. Chen *et al.*, Highly efficient and selective recovery of Au(III) from a complex system by molybdenum disulfide nanoflakes. *Chemical Engineering Journal* **350**, 692-702 (2018). doi:10.1016/j.cej.2018.05.130.
20. T. Wu, Z. Wang, Y. Lu *et al.*, Graphene Oxide Membranes for Tunable Ion Sieving in Acidic Radioactive Waste. *Adv. Sci.* **8**, 2002717 (2021). doi:10.1002/advs.202002717.
21. A. Y. Romanchuk, A. S. Slesarev, S. N. Kalmykov, D. V. Kosynkin, J. M. Tour, Graphene oxide for effective radionuclide removal. *Phys. Chem. Chem. Phys.* **15**, 2321-2327 (2013). doi:10.1039/c2cp44593j.
22. D. T. Sun, N. Gasilova, S. Yang, E. Oveisi, W. L. Queen, Rapid, Selective Extraction of Trace Amounts of Gold from Complex Water Mixtures with a Metal-Organic Framework (MOF)/Polymer Composite. *J. Am. Chem. Soc.* **140**, 16697-16703 (2018). doi:10.1021/jacs.8b09555.
23. Q. Zhang, Z. Song, X. Sun *et al.*, Atomic dynamics of electrified solid-liquid interfaces in liquid-cell TEM. *Nature* **630**, 643-647 (2024). doi:10.1038/s41586-024-07479-w.
24. Z. Zeng, X. Zhang, K. Bustillo *et al.*, In Situ Study of Lithiation and Delithiation of MoS_2 Nanosheets Using Electrochemical Liquid Cell Transmission Electron Microscopy. *Nano Lett.* **15**, 5214-5220 (2015). doi:10.1021/acs.nanolett.5b02483.
25. W. Dachraoui, R. Pauer, C. Battaglia, R. Erni, Operando Electrochemical Liquid Cell Scanning Transmission Electron Microscopy Investigation of the Growth and Evolution of the Mosaic Solid Electrolyte Interphase for Lithium-Ion Batteries. *ACS Nano* **17**, 20434-20444 (2023). doi:10.1021/acsnano.3c06879.
26. D. Cheng, J. Hong, D. Lee, S. Y. Lee, H. Zheng, In Situ TEM Characterization of Battery Materials. *Chem. Rev.* **125**, 1840-1896 (2025). doi:10.1021/acs.chemrev.4c00507.
27. M. J. Zachman, Z. Tu, S. Choudhury, L. A. Archer, L. F. Kourkoutis, Cryo-STEM mapping of solid-liquid interfaces and dendrites in lithium-metal batteries. *Nature* **560**, 345-349 (2018). doi:10.1038/s41586-018-0397-3.
28. C. Ma, Y. Cheng, K. Yin *et al.*, Interfacial Stability of Li Metal-Solid Electrolyte Elucidated via in Situ Electron Microscopy. *Nano Lett.* **16**, 7030-7036 (2016). doi:10.1021/acs.nanolett.6b03223.
29. N. de Jonge, L. Houben, R. E. Dunin-Borkowski, F. M. Ross, Resolution and aberration correction in liquid cell transmission electron microscopy. *Nat. Rev. Mater.* **4**, 61-78 (2018). doi:10.1038/s41578-018-0071-2.
30. M. Textor, N. de Jonge, Strategies for Preparing Graphene Liquid Cells for Transmission Electron Microscopy. *Nano Lett.* **18**, 3313-3321 (2018). doi:10.1021/acs.nanolett.8b01366.
31. S. Mitchell, F. Pares, D. Faust Akl *et al.*, Automated Image Analysis for Single-Atom Detection in Catalytic Materials by Transmission Electron Microscopy. *J. Am. Chem. Soc.* **144**, 8018-8029 (2022). doi:10.1021/jacs.1c12466.
32. D. J. Kelly, M. Zhou, N. Clark *et al.*, Nanometer Resolution Elemental Mapping in Graphene-Based TEM Liquid Cells. *Nano Lett.* **18**, 1168-1174 (2018). doi:10.1021/acs.nanolett.7b04713.

33. J. Hong, J. H. Bae, H. Jo *et al.*, Metastable hexagonal close-packed palladium hydride in liquid cell TEM. *Nature* **603**, 631-636 (2022). doi:10.1038/s41586-021-04391-5.
34. B. H. Kim, J. Heo, S. Kim *et al.*, Critical differences in 3D atomic structure of individual ligand-protected nanocrystals in solution. *Sci* **368**, 60-67 (2020). doi:10.1126/science.aax3233.
35. X. Ye, M. R. Jones, L. B. Frechette *et al.*, Single-particle mapping of nonequilibrium nanocrystal transformations. *Sci* **354**, 874-877 (2016). doi:10.1126/science.aah4434.
36. N. Clark, D. J. Kelly, M. Zhou *et al.*, Tracking single adatoms in liquid in a transmission electron microscope. *Nature* **609**, 942-947 (2022). doi:10.1038/s41586-022-05130-0.
37. W. Dachraoui, R. Erni, Nonclassical Nucleation and Growth of Pd Nanocrystals from Aqueous Solution Studied by In Situ Liquid Transmission Electron Microscopy. *Chem. Mater.* **35**, 1201-1208 (2023). doi:10.1021/acs.chemmater.2c03226.
38. M. F. Crook, I. A. Moreno-Hernandez, J. C. Ondry *et al.*, EELS Studies of Cerium Electrolyte Reveal Substantial Solute Concentration Effects in Graphene Liquid Cells. *J. Am. Chem. Soc.* **145**, 6648-6657 (2023). doi:10.1021/jacs.2c07778.
39. G. Malta, S. A. Kondrat, S. J. Freakley *et al.*, Identification of single-site gold catalysis in acetylene hydrochlorination. *Sci* **355**, 1399-1403 (2017). doi:10.1126/science.aal3439.
40. G. Malta, S. A. Kondrat, S. J. Freakley *et al.*, Deactivation of a Single-Site Gold-on-Carbon Acetylene Hydrochlorination Catalyst: An X-ray Absorption and Inelastic Neutron Scattering Study. *ACS Catal.* **8**, 8493-8505 (2018). doi:10.1021/acscatal.8b02232.
41. P. Johnston, N. Carthey, G. J. Hutchings, Discovery, Development, and Commercialization of Gold Catalysts for Acetylene Hydrochlorination. *J. Am. Chem. Soc.* **137**, 14548-14557 (2015). doi:10.1021/jacs.5b07752.
42. J. Shan, C. Ye, Y. Jiang *et al.*, Metal-metal interactions in correlated single-atom catalysts. *Sci. Adv.* **8**, eabo0762 (2022). doi:10.1126/sciadv.abo0762.
43. R. Frisenda, E. Navarro-Moratalla, P. Gant *et al.*, Recent progress in the assembly of nanodevices and van der Waals heterostructures by deterministic placement of 2D materials. *Chem. Soc. Rev.* **47**, 53-68 (2018). doi:10.1039/c7cs00556c.
44. W. Wang, N. Clark, M. Hamer *et al.*, Clean assembly of van der Waals heterostructures using silicon nitride membranes. *Nat. Electron.* **6**, 981-990 (2023). doi:10.1038/s41928-023-01075-y.
45. S. Kang, J. H. Kim, M. Lee *et al.*, Real-space imaging of nanoparticle transport and interaction dynamics by graphene liquid cell TEM. *Sci. Adv.* **7**, eabi5419 (2021). doi:10.1126/sciadv.abi5419.
46. T. Altantzis, I. Lobato, A. De Backer *et al.*, Three-Dimensional Quantification of the Facet Evolution of Pt Nanoparticles in a Variable Gaseous Environment. *Nano Lett.* **19**, 477-481 (2019). doi:10.1021/acs.nanolett.8b04303.
47. S. Van Aert, K. J. Batenburg, M. D. Rossell, R. Erni, G. Van Tendeloo, Three-dimensional atomic imaging of crystalline nanoparticles. *Nature* **470**, 374-377 (2011). doi:10.1038/nature09741.
48. Z. Y. Li, N. P. Young, M. Di Vece *et al.*, Three-dimensional atomic-scale structure of size-selected gold nanoclusters. *Nature* **451**, 46-48 (2008). doi:10.1038/nature06470.
49. T. P. Hardcastle, C. R. Seabourne, R. Zan *et al.*, Mobile metal adatoms on single layer, bilayer, and trilayer graphene: An *ab initio* DFT study with van der Waals corrections

correlated with electron microscopy data. *Phys. Rev. B* **87**, 195430 (2013). doi:10.1103/PhysRevB.87.195430.

50. J. P. Jalkanen, M. Halonen, D. Fernandez-Torre, K. Laasonen, L. Halonen, A computational study of the adsorption of small Ag and Au nanoclusters on graphite. *J. Phys. Chem. A* **111**, 12317-12326 (2007). doi:10.1021/jp074969m.
51. C. Zhang, Z. Fu, Q. Zhao *et al.*, Single-atom-Ni-decorated, nitrogen-doped carbon layers for efficient electrocatalytic CO_2 reduction reaction. *Electrochem. Commun.* **116**, 106758 (2020). doi:10.1016/j.elecom.2020.106758.
52. K. Liu, J. Fu, Y. Lin *et al.*, Insights into the activity of single-atom Fe-N-C catalysts for oxygen reduction reaction. *Nat. Commun.* **13**, 2075 (2022). doi:10.1038/s41467-022-29797-1.
53. A. Zitolo, V. Goellner, V. Armel *et al.*, Identification of catalytic sites for oxygen reduction in iron- and nitrogen-doped graphene materials. *Nat. Mater.* **14**, 937-942 (2015). doi:10.1038/nmat4367.
54. H. E. Swanson, H. F. McMurdie, M. C. Morris, E. H. Evans, Standard x-ray diffraction powder patterns, National Bureau of Standards, (1969). doi: 10.6028/nbs.mono.25-7.
55. U. Patil, N. M. Caffrey, The role of solvent interfacial structural ordering in maintaining stable graphene dispersions. *2D Mater.* **11**, 015017 (2023). doi:10.1088/2053-1583/ad10ba.
56. L. Liu, A. Corma, Metal Catalysts for Heterogeneous Catalysis: From Single Atoms to Nanoclusters and Nanoparticles. *Chem. Rev.* **118**, 4981-5079 (2018). doi:10.1021/acs.chemrev.7b00776.
57. R. D. Deegan, O. Bakajin, T. F. Dupont *et al.*, Capillary flow as the cause of ring stains from dried liquid drops. *Nature* **389**, 827-829 (1997). doi:10.1038/39827.
58. P. J. Yunker, T. Still, M. A. Lohr, A. G. Yodh, Suppression of the coffee-ring effect by shape-dependent capillary interactions. *Nature* **476**, 308-311 (2011). doi:10.1038/nature10344.
59. T. Otanicar, J. Hoyt, M. Fahar, X. Jiang, R. A. Taylor, Experimental and numerical study on the optical properties and agglomeration of nanoparticle suspensions. *J. Nanoparticle Res.* **15**, 2039 (2013). doi:10.1007/s11051-013-2039-x.
60. S. Sullivan-Allsop, Experimental data and analysis code, Figshare, (2026). doi: DOI:10.48420/30998680.
61. R. V. Gorbachev, I. Riaz, R. R. Nair *et al.*, Hunting for monolayer boron nitride: optical and Raman signatures. *Small* **7**, 465-468 (2011). doi:10.1002/smll.201001628.
62. W. Wang, G. R. Tainton, N. J. Clark *et al.*, Atomic Imaging of 2D Transition Metal Diiodides. *ACS Nano*, (2026). doi:10.1021/acsnano.5c19196.
63. S. Somnath, C. R. Smith, S. V. Kalinin *et al.*, Feature extraction via similarity search: application to atom finding and denoising in electron and scanning probe microscopy imaging. *Adv. Struct. Chem. Imaging* **4**, 3 (2018). doi:10.1186/s40679-018-0052-y.
64. D. B. Allan, T. Caswell, N. C. Keim, C. M. van der Wel, R. W. Verweij, soft-matter/trackpy: v0.6.3, Zenodo, (2024). doi: 10.5281/ZENODO.11522100.
65. J. C. Crocker, D. G. Grier, Methods of Digital Video Microscopy for Colloidal Studies. *J. Colloid Interface Sci.* **179**, 298-310 (1996). doi:10.1006/jcis.1996.0217.
66. J. Madsen, T. Susi, The abTEM code: transmission electron microscopy from first principles. *Open Res. Eur.* **1**, 24 (2021). doi:10.12688/openreseurope.13015.2.

67. P. Giannozzi, O. Andreussi, T. Brumme *et al.*, Advanced capabilities for materials modelling with Quantum ESPRESSO. *J. Phys.: Condens. Matter* **29**, 465901 (2017). doi:10.1088/1361-648X/aa8f79.
68. P. Giannozzi, S. Baroni, N. Bonini *et al.*, QUANTUM ESPRESSO: a modular and open-source software project for quantum simulations of materials. *J. Phys.: Condens. Matter* **21**, 395502 (2009). doi:10.1088/0953-8984/21/39/395502.
69. J. M. Soler, E. Artacho, J. D. Gale *et al.*, The SIESTA method forab initioorder-Nmaterials simulation. *J. Phys.: Condens. Matter* **14**, 2745-2779 (2002). doi:10.1088/0953-8984/14/11/302.
70. K. Lee, É. D. Murray, L. Kong, B. I. Lundqvist, D. C. Langreth, Higher-accuracy van der Waals density functional. *Phys. Rev. B* **82**, 081101 (2010). doi:10.1103/PhysRevB.82.081101.
71. Simune Atomistics, ASAP: Atomistic Simulation Advanced Platform - SIESTA Pseudopotential and Basis Set Database, url: https://www.simuneatomistics.com/dft-toolkit/, (Accessed: 2025-01-08).
72. Cornell University, NNIN/C Pseudopotential Virtual Vault, url: https://nninc.cnf.cornell.edu, (Accessed: 2025-01-08).
73. M. J. Frisch, G. W. Trucks, H. B. Schlegel *et al.*, Gaussian 16 Revison. C.01, (2016).url:https://gaussian.com/gaussian16/.
74. A. D. Becke, Density-functional thermochemistry. III. The role of exact exchange. *J. Chem. Phys.* **98**, 5648-5652 (1993). doi:10.1063/1.464913.
75. T. H. Dunning, Gaussian basis sets for use in correlated molecular calculations. I. The atoms boron through neon and hydrogen. *J. Chem. Phys.* **90**, 1007-1023 (1989). doi:10.1063/1.456153.
76. P. J. Hay, W. R. Wadt, Ab initio effective core potentials for molecular calculations. Potentials for K to Au including the outermost core orbitals. *J. Chem. Phys.* **82**, 299-310 (1985). doi:10.1063/1.448975.
77. J. Tomasi, B. Mennucci, E. Cancès, The IEF version of the PCM solvation method: an overview of a new method addressed to study molecular solutes at the QM ab initio level. *J. Mol. Struct. THEOCHEM* **464**, 211-226 (1999). doi:10.1016/s0166-1280(98)00553-3.
78. P. Blake, E. W. Hill, A. H. Castro Neto *et al.*, Making graphene visible. *Appl. Phys. Lett.* **91**, 063124 (2007). doi:10.1063/1.2768624.
79. M. J. Hamer, D. G. Hopkinson, N. Clark *et al.*, Atomic Resolution Imaging of $CrBr_3$ Using Adhesion-Enhanced Grids. *Nano Lett.* **20**, 6582-6589 (2020). doi:10.1021/acs.nanolett.0c02346.
80. S. Keskin, C. Pawell, N. de Jonge, Verification of water presence in graphene liquid cells. *Micron* **149**, 103109 (2021). doi:10.1016/j.micron.2021.103109.
81. F. de la Peña, E. Prestat, V. T. Fauske *et al.*, hyperspy/hyperspy: v1.7.6, Zenodo, (2023). doi: 10.5281/ZENODO.10151686.
82. F. Pedregosa, G. Varoquaux, A. Gramfort *et al.*, Scikit-learn: Machine Learning in Python. *J. Mach. Learn. Res.* **12**, 2825-2830 (2011). doi:10.5555/1953048.2078195.
83. T. Malis, S. C. Cheng, R. F. Egerton, EELS log-ratio technique for specimen-thickness measurement in the TEM. *J. Electron Microsc. Tech.* **8**, 193-200 (1988). doi:10.1002/jemt.1060080206.
84. B. Rieger, I. Droste, F. Gerritsma, T. Ten Brink, S. Stallinga, Single image Fourier ring correlation. *Opt. Express* **32**, 21767-21782 (2024). doi:10.1364/OE.524683.

85. S. van der Walt, J. L. Schonberger, J. Nunez-Iglesias *et al.*, scikit-image: image processing in Python. *PeerJ* **2**, e453 (2014). doi:10.7717/peerj.453.
86. A. Paszke, S. Gross, F. Massa *et al.*, PyTorch: An Imperative Style, High-Performance Deep Learning Library. *arXiv/cs*, (2019). doi:10.48550/arXiv.1912.01703.
87. A. Krull, T.-O. Buchholz, F. Jug, in *2019 IEEE/CVF Conference on Computer Vision and Pattern Recognition (CVPR)*. (IEEE, 2019), pp. 2124-2132.
88. W. Thornley, S. Sullivan-Allsop, R. Cai *et al.*, Noise2Void for denoising atomic resolution scanning transmission electron microscopy images. *npj Comput. Mater.*, (2026). doi:10.1038/s41524-025-01939-1.
89. G. T. Martinez, K. H. W. van den Bos, M. Alania, P. D. Nellist, S. Van Aert, Thickness dependence of scattering cross-sections in quantitative scanning transmission electron microscopy. *Ultramicroscopy* **187**, 84-92 (2018). doi:10.1016/j.ultramic.2018.01.005.
90. A. Garcia, A. M. Raya, M. M. Mariscal *et al.*, Analysis of electron beam damage of exfoliated MoS_2 sheets and quantitative HAADF-STEM imaging. *Ultramicroscopy* **146**, 33-38 (2014). doi:10.1016/j.ultramic.2014.05.004.
91. P. Jensen, X. Blase, P. Ordejón, First principles study of gold adsorption and diffusion on graphite. *Surf. Sci.* **564**, 173-178 (2004). doi:10.1016/j.susc.2004.06.188.
92. N. M. Schneider, M. M. Norton, B. J. Mendel *et al.*, Electron–Water Interactions and Implications for Liquid Cell Electron Microscopy. *J. Phys. Chem. C* **118**, 22373-22382 (2014). doi:10.1021/jp507400n.
93. P. Abellan, B. L. Mehdi, L. R. Parent *et al.*, Probing the degradation mechanisms in electrolyte solutions for Li-ion batteries by in situ transmission electron microscopy. *Nano Lett.* **14**, 1293-1299 (2014). doi:10.1021/nl404271k.
94. T. J. Woehl, P. Abellan, Defining the radiation chemistry during liquid cell electron microscopy to enable visualization of nanomaterial growth and degradation dynamics. *J. Microsc.* **265**, 135-147 (2017). doi:10.1111/jmi.12508.
95. M. Wang, C. Park, T. J. Woehl, Quantifying the Nucleation and Growth Kinetics of Electron Beam Nanochemistry with Liquid Cell Scanning Transmission Electron Microscopy. *Chem. Mater.* **30**, 7727-7736 (2018). doi:10.1021/acs.chemmater.8b03050.
96. L. A. J. Garvie, P. R. Buseck, Determination of Ce^{4+}/Ce^{3+} in electron-beam-damaged CeO_2 by electron energy-loss spectroscopy. *J. Phys. Chem. Solids* **60**, 1943-1947 (1999). doi:10.1016/s0022-3697(99)00218-8.

Funding: The authors acknowledge funding from the European Research Council (ERC) under the European Union's Horizon 2020 research and innovation programme (Grant ERC-2016-STG-EvoluTEM-715502 and ERC-2020-COG-QTWIST-101001515). We also thank the Engineering and Physical Sciences Research Council (EPSRC) for funding under grants EP/Y024303, EP/S021531/1, EP/M010619/1, EP/V007033/1, EP/S030719/1, EP/V001914/1, EP/V036343/1 and EP/P009050/1, access to ARCHER2 supercomputer through the Materials Chemistry Consortium (EP/X035859), and also for the EPSRC Centre for Doctoral Training (CDT) Graphene-NOWNANO. TEM access was supported by the Henry Royce Institute for Advanced Materials, funded through EPSRC grants EP/R00661X/1, EP/S019367/1, EP/P025021/1, and EP/P025498/1. RVG. and VIF. acknowledge funding from the European Quantum Flagship Project 2DSIPC (no. 820378). We thank Diamond Light Source for access and support in use of the electron Physical Science Imaging Centre (Instrument E02 and proposal numbers MG33252 and MG35552) that contributed to the results presented here. SJH acknowledges funding from BP through the BP-International Centre for Advanced Materials. BD, SP, NFD and GJH would like to thank the Max Planck Centre on the Fundamentals of Heterogeneous Catalysis (FUNCAT) for funding. AJL acknowledges funding by the UKRI Future Leaders Fellowship program (MR/T018372/1, MR/Y034279/1).

Author contributions:

Conceptualization: SSA, NC, RG, SJH

Methodology: SSA, NC, WW

Investigation: SSA, NC, WW, RC, WT, DGH, JM, BD, SP, NFD, RZ, ML, GT, JH, HDL, JP, JS, EC, AC, DL, NM, AS

Formal Analysis: SSA, NC

Funding Acquisition: CSA, MD, AJL, VF, GJH, RG, SJH

Supervision: CSA, MD, AJL, VF, GJH, RG, SJH

Writing: SSA, NC, RG, SJH

Competing interests: Authors declare that they have no competing interests.

Data and materials availability: Raw data, denoised data and analysis code are freely from a permanent repository(*60*).

Supplementary materials:
Materials and Methods
Figs. S1 to S39
Tables S1 to S6
Movies S1 to S8
References (61-96)

Science
AAAS

Supplementary Materials for

Atomic-resolution imaging of gold species at organic liquid-solid interfaces

Sam Sullivan-Allsop, Nick Clark, Wendong Wang, Rongsheng Cai, William Thornley, David G. Hopkinson, James McHugh, Ben Davies, Samuel Pattisson, Nicholas F. Dummer, Rui Zhang, Matthew Lindley, Gareth Tainton, Jack Harrison, Hugo De Latour, Joseph Parker, Joshua Swindell, Eli Castanon, Amy Carl, David Lewis, Natalia Martsinovich, Christopher S. Allen, Mohsen Danaie, Andrew J. Logsdail, Vladimir Falko, Graham J. Hutchings, Alex Summerfield, Roman Gorbachev, Sarah J. Haigh

Correspondence to:

nick.clark@manchester.ac.uk, roman@manchester.ac.uk, sarah.haigh@manchester.ac.uk

Supplementary information contains:

Materials and Methods

Supplementary Text

Figures S1 to S39

Tables S1 to S6

Other Supplementary Materials for this manuscript include the following:

Movies S1 to S8

Supporting Movie Legends

Movie S1: Simultaneously acquired HAADF- (left panels) and BF-STEM (right panels) image series for a GLC containing liquid acetone and gold salt.

Movie S2: Simultaneously acquired HAADF- (left panels) and BF-STEM (right panels) image series for a GLC containing liquid cyclohexanone and gold salt.

Movie S3: Simultaneously acquired HAADF- (left panels) and BF-STEM (right panels) image series for a GLC which was filled with acetone and gold salt, but was not sealed, so the liquid has evaporated to give our 'Acetone Vacuum' control data.

Movie S4: Simultaneously acquired HAADF- (left panels) and BF-STEM (right panels) image series for a GLC which was filled with cyclohexanone and gold salt, but was not sealed, so the liquid has evaporated to give our 'Cyclohexanone Vacuum' control data.

Movie S5: HAADF-STEM image series for a GLC containing liquid acetone and gold salt (Movie S1). The video progressively shows the cumulative processing stages for the analysis. The stages are: raw images, denoised images, drift corrected images, gold positions identified, lattice sites identified and the full atomic model.

Movie S6: Comparison of the raw (top row) and denoised (bottom row) simultaneously acquired HAADF- (left panels) and BF-STEM (right panels) image series for a GLC containing liquid acetone and gold salt (Movie S1).

Movie S7: Schematic image series of atomic models built from the measured positions within Movie S1.

Movie S8: HAADF-STEM image series for a GLC containing liquid acetone and gold salt (Movie S1), with the adatom dimer and trimer pairing highlighted.

Materials and Methods

Solutions

Tetrachloroauric (III) Acid Trihydrate was purchased in powder form from Merck UK (CAS 1691-25-4 99.9% trace metals basis) and dissolved in the chosen solvent at concentrations of 5-50 mM. Isopropanol was added to the aqueous solution at a ratio of 3:1 to suppress hydrogen evolution via radical scavenging. No additives were used for the acetone, cyclohexanone, ethanol, and 1-butanol solutions.

Liquid Cell fabrication

Graphene liquid cells (GLCs) were fabricated by stacking mechanically exfoliated crystals. hBN crystals of the correct thickness were identified by their optical contrast(*61*), and patterned with ~500 nm diameter microwells using electron beam lithography and reactive ion etching. The hBN was then encapsulated using graphitic windows of appropriate thickness via direct stamping with a metallized SiN_x cantilever which had been prepatterned with ~2 µm through-holes(*62*). The final transfer was performed while immersed in the target liquid, causing it to be encapsulated within the hBN microwells where the 3 crystals overlapped. The silicon nitride cantilever was then deposited on a custom SiN_x TEM support. Non-overlapping regions with no liquid present were used as controls. Full details in SI section 3.

Scanning Transmission Electron Microscopy (STEM) imaging

STEM imaging and electron energy loss spectroscopy (EELS) was carried out using an FEI Titan G2 80−200 S/TEM ChemiSTEM, operating in STEM mode with a 200 kV accelerating voltage, a 21 mrad convergence angle and a 48 mrad high angle annular dark field (HAADF) inner collection angle. The EELS was carried out with a beam current of 60 pA, with 0.1 eV/channel dispersion and dwell time of 0.1 s. High resolution STEM imaging was carried out using a JEOL GrandARM 300F using an 80 kV accelerating voltage and a 31.74 mrad convergence angle (minimum probe size of 0.62 nm at 10 nm defocus), condenser lens aperture of 40 µm, 9 cm camera length & BF aperture of 3 mm. A beam current of 46.5 pA was used, with an electron flux of approximately 1.67×10^6 e^- s^{-1} nm^{-2}. Bright field (BF) and HAADF images were simultaneously collected to enable identification of the atomic lattice positions of the graphitic windows and Au species respectively (BF collection semi-angle was 0 – 14.8 ± 1.2 mrad and HAADF collection semi-angle was 73.7 ± 1.8 – 155.4 ± 1.8 mrad). STEM image intensity is shown false coloured using an inferno colour palette (inferno colourmap is perceptually uniform).

Image processing

The denoised BF images were reconstructed by a patch-based template matching algorithm(*63*). Trackpy(*64*) was used to identify the atomic positions within the reconstructed BF image. The located positions were linked frame-to-frame on a nearest-neighbour basis, applying the Crocker-Grier algorithm(*65*) from within Trackpy. The linked trajectories were used to establish the framewise drift correction. Thresholding was applied to the HAADF-STEM images and then Trackpy(*64*) was also used to locate the gold atomic positions. The located positions were linked, and the drift correction established from the BF was applied to the positions and then the trajectories were established.

Image simulations methods

The STEM image simulations were obtained through the use of the Python package, abTEM(*66*). The simulation parameters were matched to that of the experimental conditions used (80 kV acceleration voltage, 31.74 mrad convergence angle, BF annular range was 0 – 31 mrad and HAADF annular range was 74 – 155 mrad, spherical aberrations of 1 μm). The simulations were obtained using the atomic positions for a single window of multilayer graphene with a gold adatom decorating the surface. A single adatom on the window is shown in Fig, S7. The simulated images that are based upon experimental data take the measured atomic positions and then use these as the input for the abTEM simulation, see Fig. S9.

Density functional theory methods

Au Graphite Sublattice Dependency: DFT calculations were performed using Quantum ESPRESSO code(*67, 68*). A spacing of 20 Å between repeated images in the out-of-plane direction was applied to avoid interactions between repeated images. Vanderbilt norm-conserving pseudopotentials were used to mimic the effect of core electrons, parameterized using the Perdew-Burke-Ernzerhof (PBE) Generalized Gradient Approximation (GGA) of the exchange-correlation functional. The Brillouin zone was sampled using a regular Monkhorst-Pack *k*-point grid of $28 \times 28 \times 1$ in a bilayer graphene (BLG) unit cell (2.46 x 2.46 Å); in larger cells the *k*-point spacing was varied to match this *k*-point density (see Fig. S32). The vdW-DF-c09 functional was used to model van der Waals interactions, and Coulomb interactions in the out-of-plane direction were truncated to avoid spurious long-range interactions.

Au, Graphite & Solvent Interactions: Density functional theory (DFT) calculations were carried out using SIESTA software(*69*) with the vdW-DF2 van der Waals density functional(*70*). The calculations employed localised atomic orbitals represented using numerical double-zeta polarised (DZP) basis sets: the basis sets for C, O and H provided on the Simune Atomistics website(*71*) and the basis set for Au generated by SIESTA with the energy shift of 5 meV; these were used in combination with Troullier-Martins pseudopotentials from the Simune Atomistics website for C, O and H(*71*) and from Cornell University Pseudopotential Virtual Vault for Au(*72*). A 5 x 6-extended hexagonal graphene unit cell with the dimensions of 12.30 x 14.76 Å (60 C atoms) was used for calculations; the height of the cell in the vertical dimension was set to 15 Å to avoid interaction with neighbouring cells. Carbon atoms of graphene were fixed at their ideal positions, while the adsorbates' atom positions were optimised until maximum atomic displacements were below 0.1 Å and maximum forces below 0.05 eV/Å.

Au-Solvent Interactions: DFT calculations of Au-solvent interactions were carried out using Gaussian16 software(*73*) with the B3LYP functional(*74*), cc-pVDZ basis sets for C, O and H(*75*) and LANL2DZ basis set and pseudopotential for Au(*76*). Implicit solvent environment was described using the Polarizable Continuum Model using the integral equation formalism variant (PCM-IEF) method(*77*).

Supplementary Text

Contents

1. Example Atomic Resolution HAADF- and BF-STEM Images and Combined HAADF/BF Composite Images

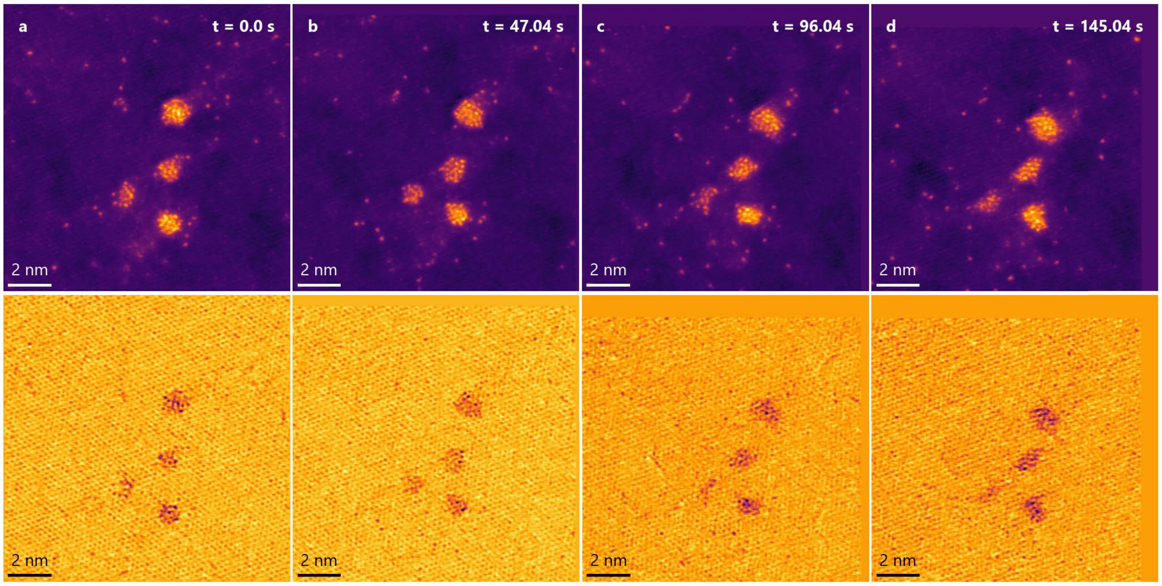

Figure S1: Example simultaneous HAADF- (upper panels) and BF-STEM (lower panels) frames from an image sequence acquired for a GLC containing liquid acetone and gold salt. *Borders appearing in the later images are artefacts of the drift correction process. The full video is shown in supplementary video 1.*

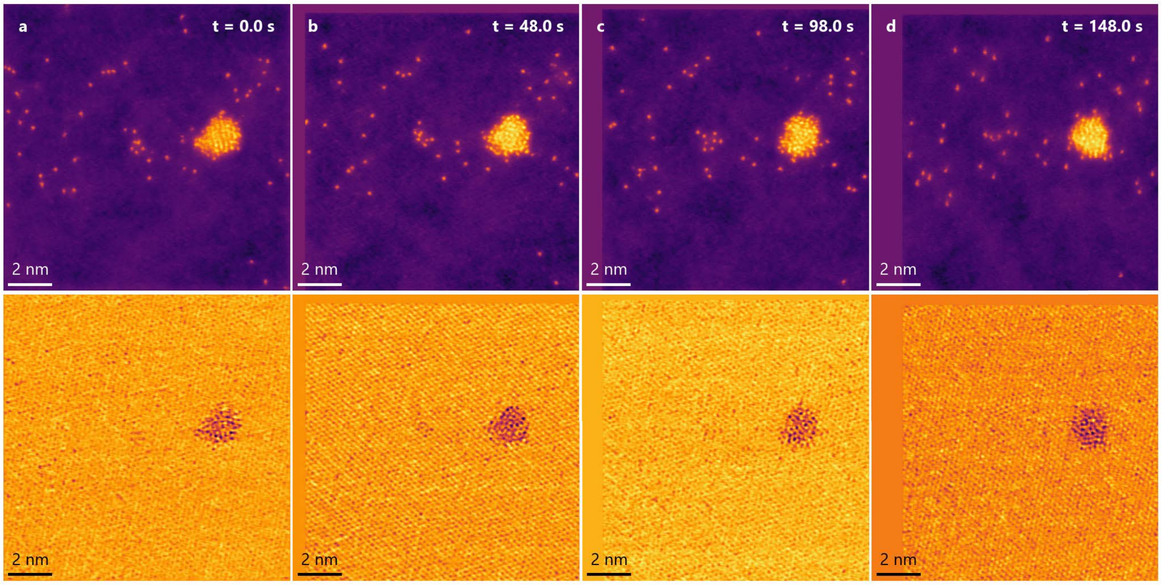

Figure S2: Example simultaneous HAADF- (upper panels) and BF-STEM (lower panels) frames from an image sequence acquired in a GLC containing liquid cyclohexanone and gold salt. *Borders appearing in some of the images are artefacts of the drift correction process. The full video is shown in supplementary video 2.*

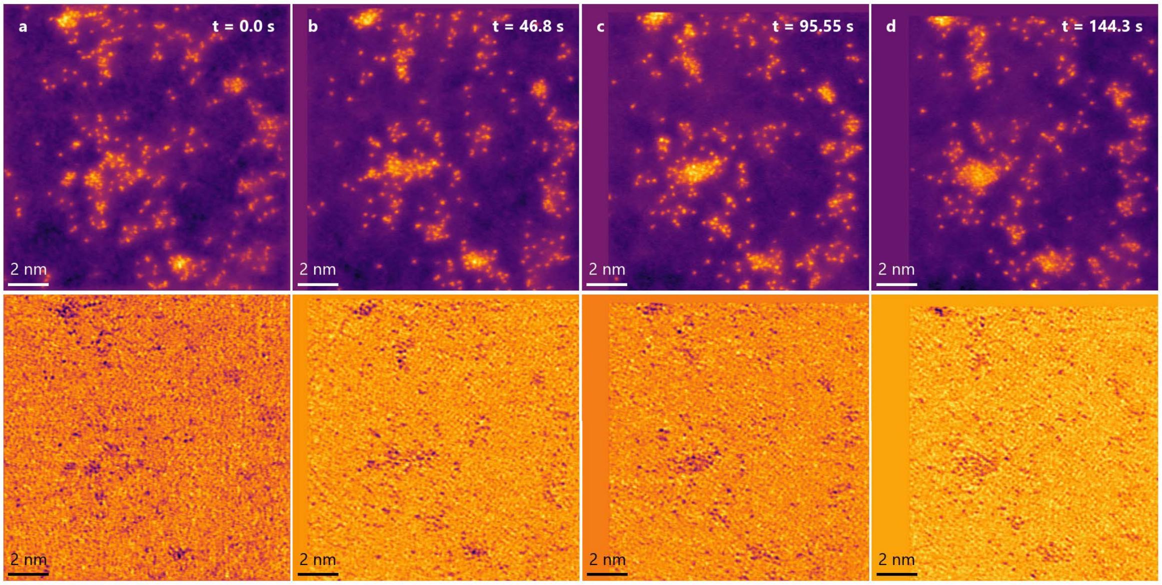

Figure S3: Example simultaneous HAADF- (upper panels) and BF-STEM (lower panels) frames from an image sequence acquired for a GLC which was filled with acetone and gold salt but was not sealed, so the liquid has evaporated to give our 'Acetone Vacuum' control data. *The borders appearing in the images are artefacts of the drift correction process. The full video is shown in supplementary video 3.*

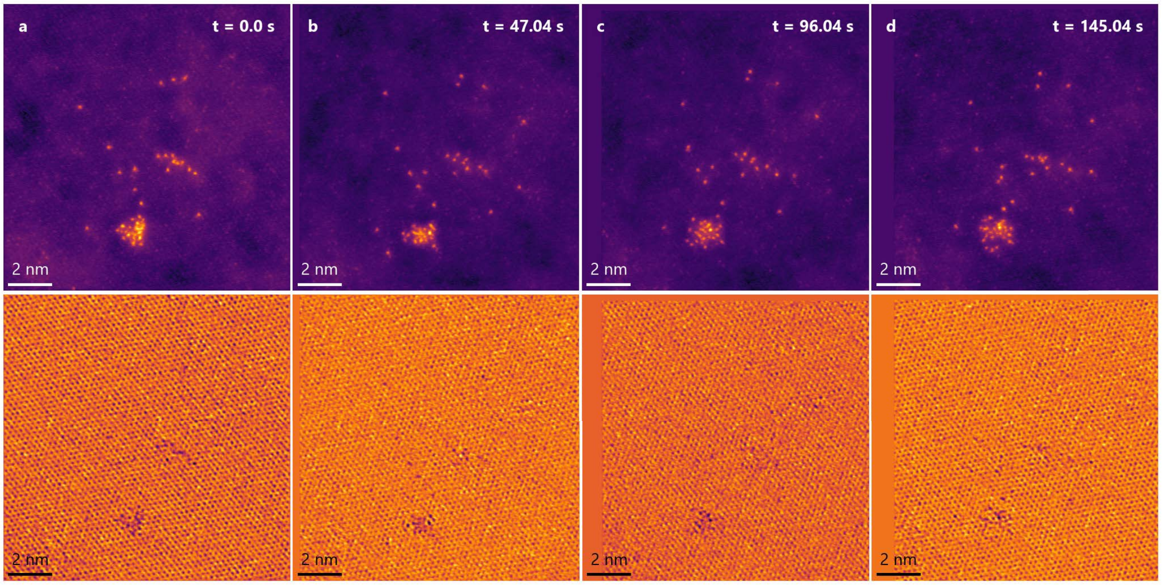

Figure S4: Example simultaneous HAADF- (upper panels) and BF-STEM (lower panels) frames from an image sequence acquired for a GLC which was filled with cyclohexanone and gold salt but was not sealed, so the liquid has evaporated to give our 'Cyclohexanone Vacuum' control data. *The borders appearing in the images are artifacts of the drift correction process. The full video is shown in supplementary video 4.*

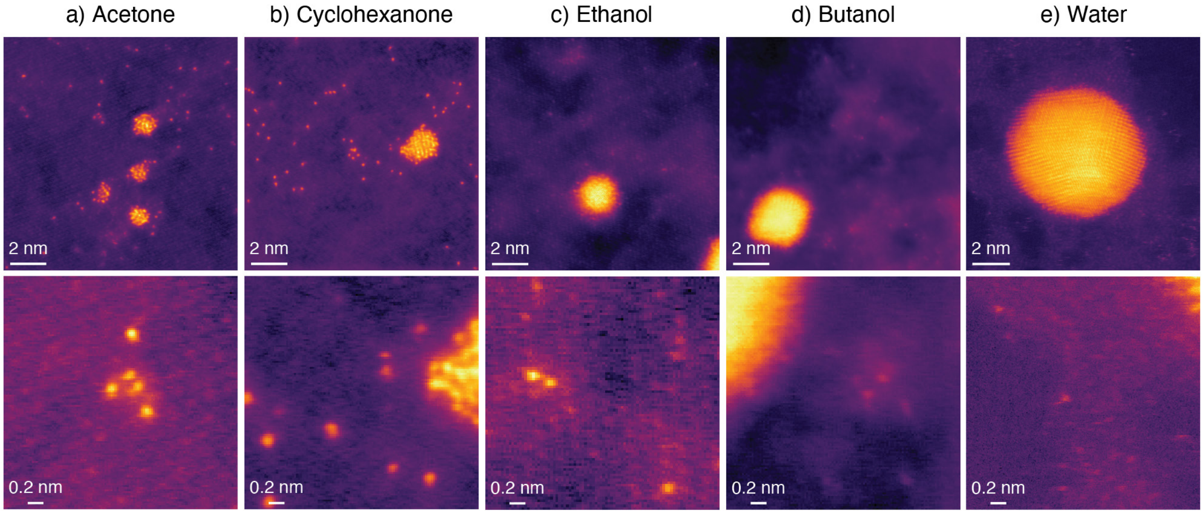

Figure S5: Example representative simultaneous HAADF- STEM images for a GLC filled with gold salt and a solvent. *The variety of the gold structures within the GLC include isolated species, small amorphous clusters, large amorphous clusters, and crystalline nanoparticles. The solvents are acetone, cyclohexanone, ethanol, butanol & water (a-e respectively). The bottom row shows a high magnification region containing the isolated species.*

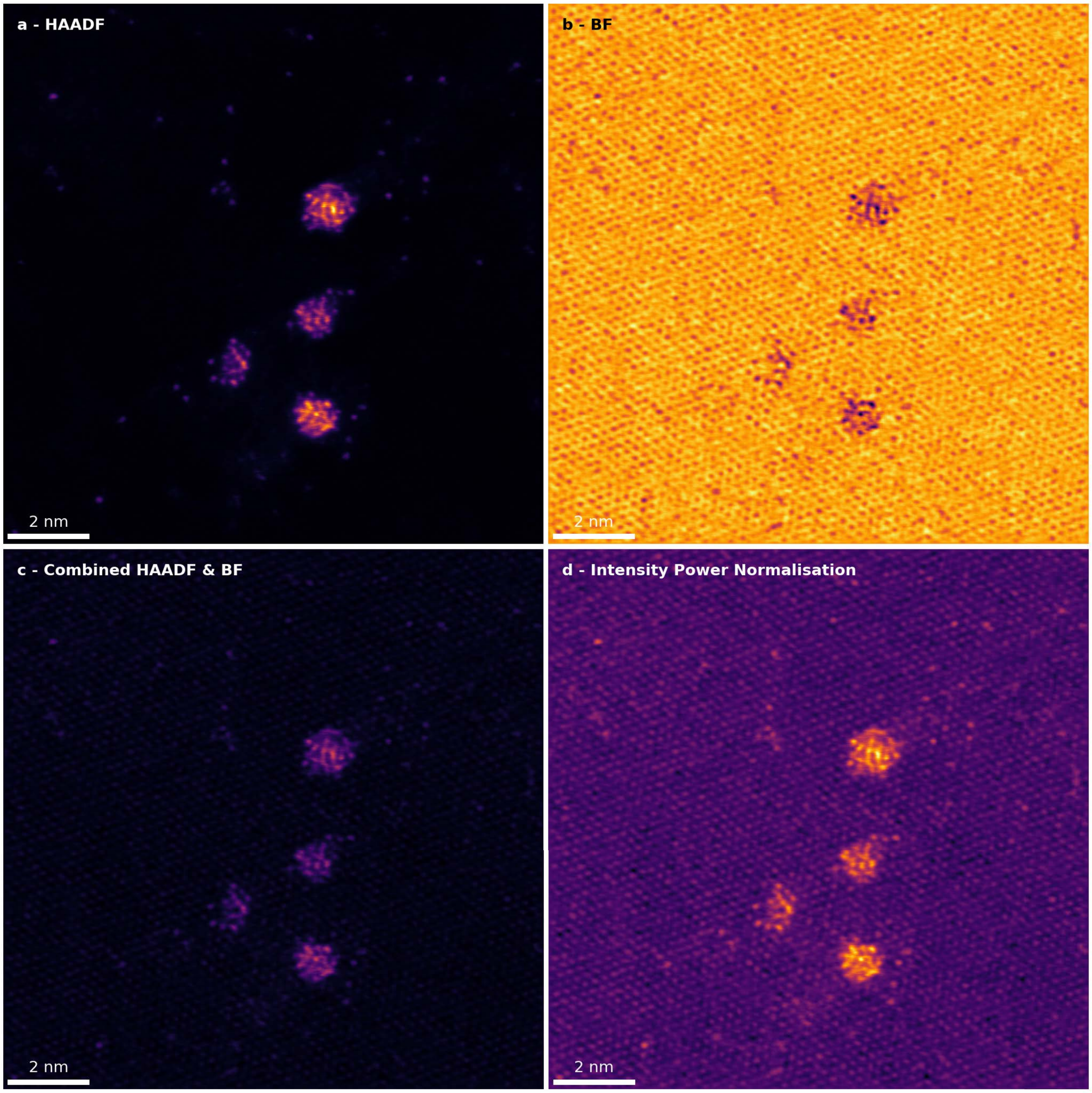

Figure S6: Combining simultaneous HAADF- and BF-STEM images. *(a,b) Denoised HAADF- and BF-STEM images. (c) Combined image of the HAADF- and BF-STEM (a) and (b). (d) Power law normalised version of the combination image (see SI section 3 for details of image processing).*

The *Z*-contrast sensitivity of the HAADF-STEM imaging mode reveals single atomic gold species with high contrast even in the presence of the graphene support and surrounding liquid. The phase contrast of the simultaneously acquired BF-STEM image is better able to reveal the crystal lattice of the underlying graphene support. The combined HAADF-/BF-STEM images therefore better illustrate both Au dispersion and the underlying graphene lattice. These images are produced by taking the HAADF image and summing with the inverted BF image and then applying a power law normalisation (see Fig. S6 and Section 3 for details of image processing).

2. Simulated Atomic Resolution BF- and HAADF-STEM Images

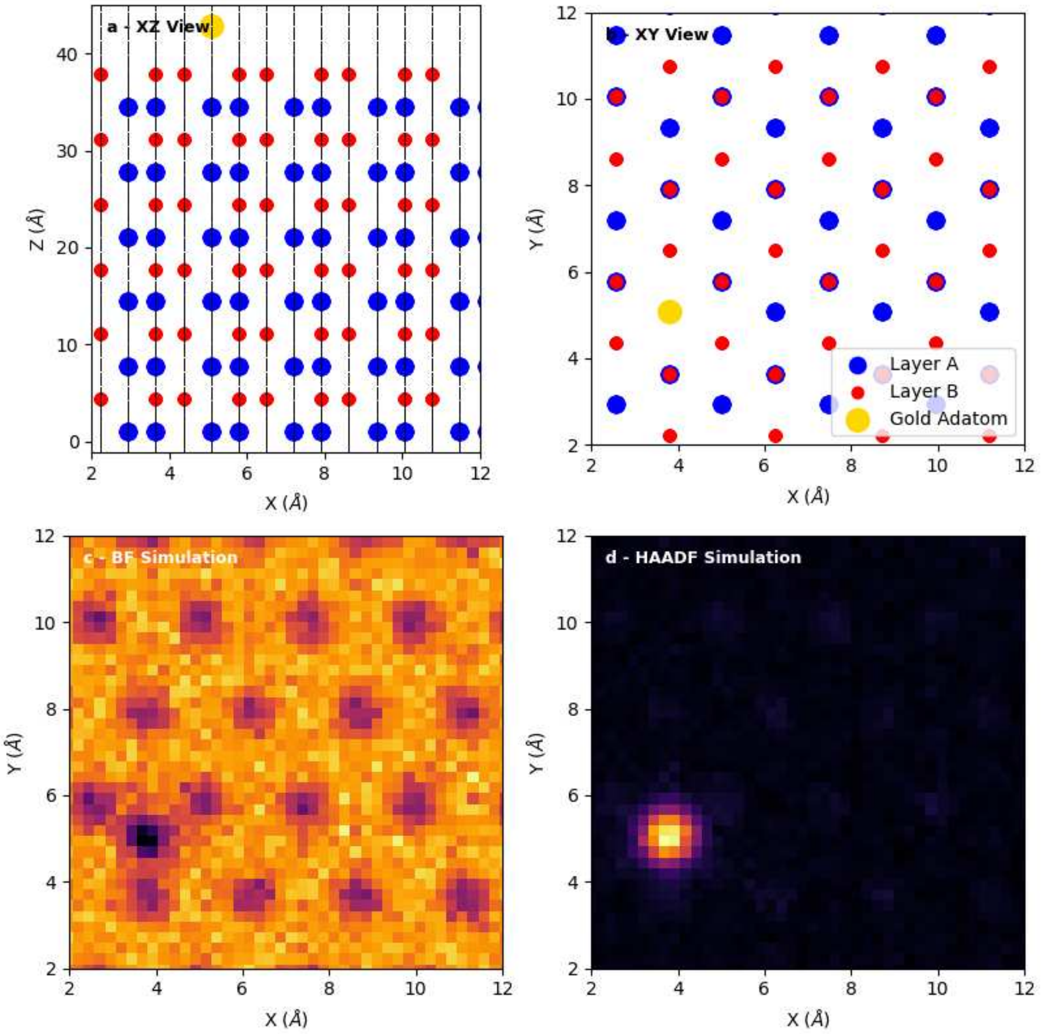

Figure S7: Atomic model and BF- and HAADF-STEM image simulations for graphite supporting atomically dispersed Au. *(a,b) The input atomic structure model used for generating the simulated images, shown for xz (cross sectional) and xy (plan view) orientations. The model consists of a 12 atomic layer (~4 nm) thick graphite slab with a single gold atom on the surface. The electron beam is incident along the negative Z direction. Vertical lines have been added to (a) to highlight the vertically aligned carbon atoms. To highlight the location of overlapping carbon atoms in the plan view images, carbon atoms in the A layers have been coloured blue and made larger than the carbon atoms in the B layers. For the image simulations the probe was focused on the xy plane containing the gold adatom, and the simulation was carried out using relevant experimental parameters (see Materials and Methods). (c,d) The output of the image simulations for BF- and HAADF-STEM, respectively. Within the BF images the lattice positions are only visible at the locations where carbon atoms from every layer of the graphene are vertically aligned.*

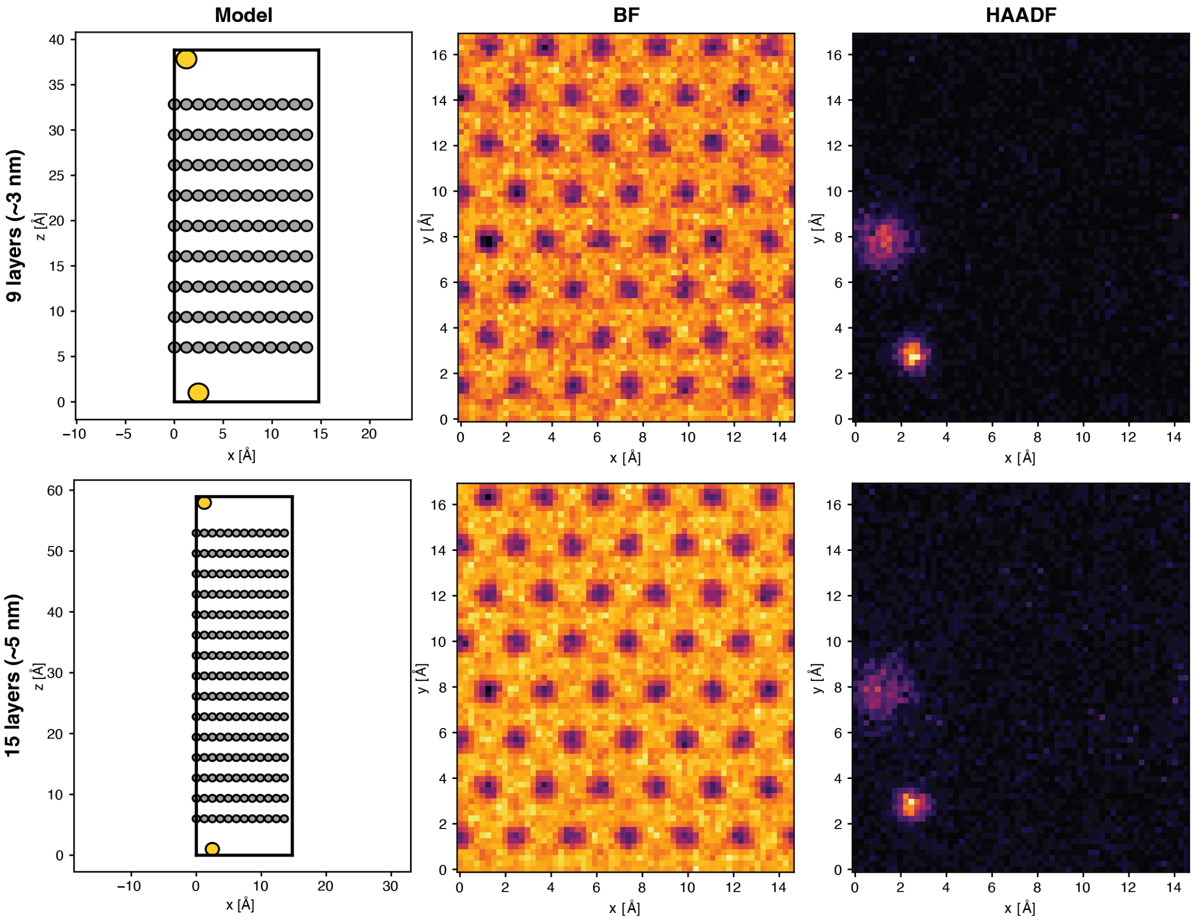

Figure S8: Atomic model and BF- and HAADF-STEM image simulations for 9 (~3 nm) & 15 (~5 nm) layer graphite windows.

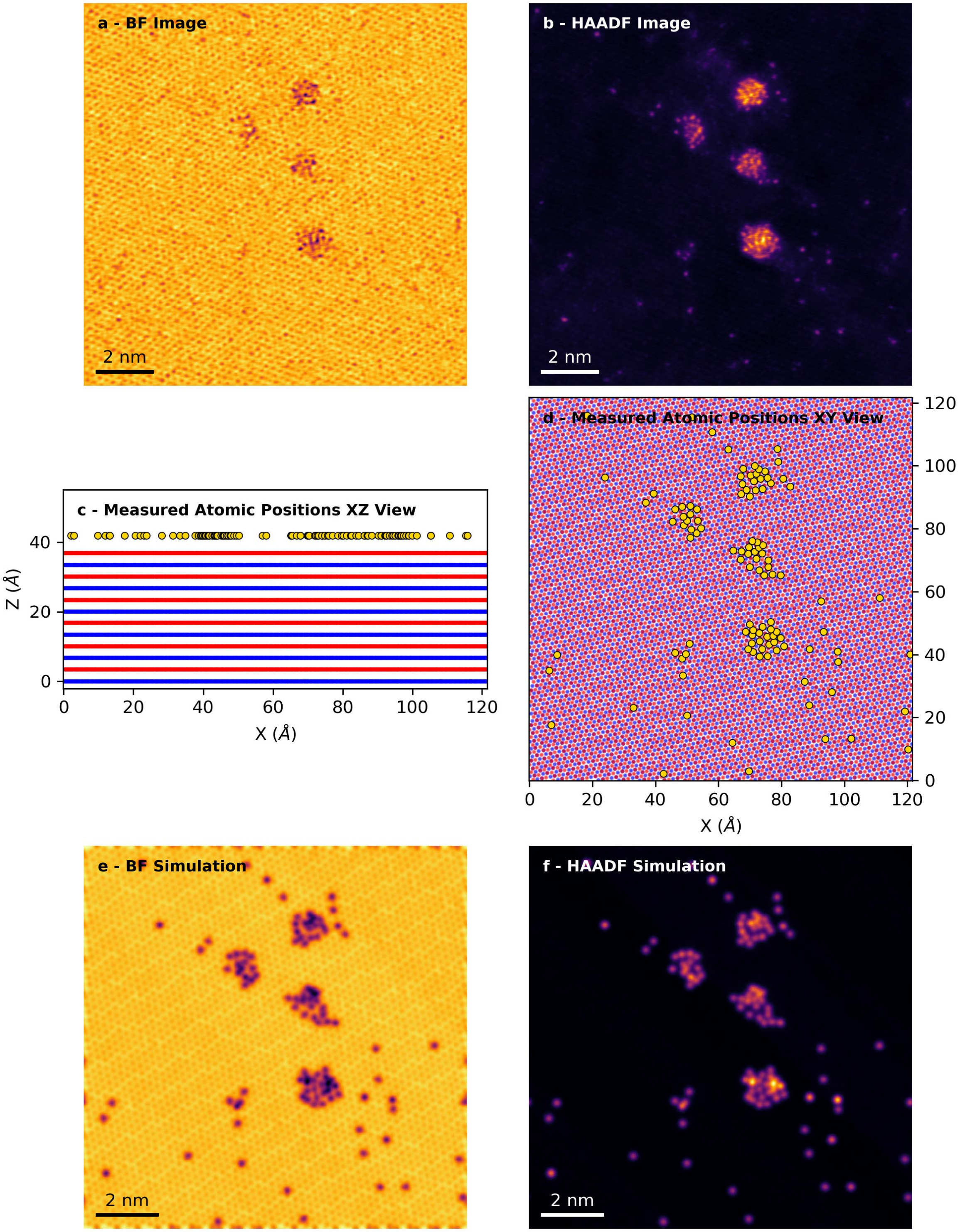

Figure S9: Simulating BF- and HAADF-STEM images based on the experimentally measured atomic positions. *(a,b) display the experimental BF- and HAADF-STEM images, respectively. (c,d) Atomic model matching the positions derived from the experimental images in (a) and (b), shown for xz and xy views, respectively. In these panels, the two sublattices of multilayer graphene are highlighted in red and blue, while the gold adatoms on the surface are depicted in yellow. (e,f) The simulated images based on these positions are given, (e) for BF and (f) for HAADF.*

STEM image simulations were used to probe the impact of sample tilt upon the atom tracking and the gold atom resting sites. The simulations were generated using atomic models built from measured atomic positions and artificially tilted. The models of the tilted samples (top row), the noise-free image simulation (middle row) and the simulations with realistic experimental noise (bottom row) are shown in Fig. S10. When the tilt is less than 2°, the image quality and atom-lattice correlation is broadly consistent with the un-tilted case(Fig. S10a&b). At 2° artifacts are introduced due the tilt, including an apparent smearing of the atom-lattice correlation and the atomic sites being visibly elongated. Increasing the tilt to 5° results in the failure of the lattice tracking algorithm, and a loss of the spatial frequencies corresponding to graphite in the fast Fourier transform (FFT). Comparison of the experimental data with the simulations using the BF appearance and the atom-lattice correlation implies that the tilt of our samples was below 2°.

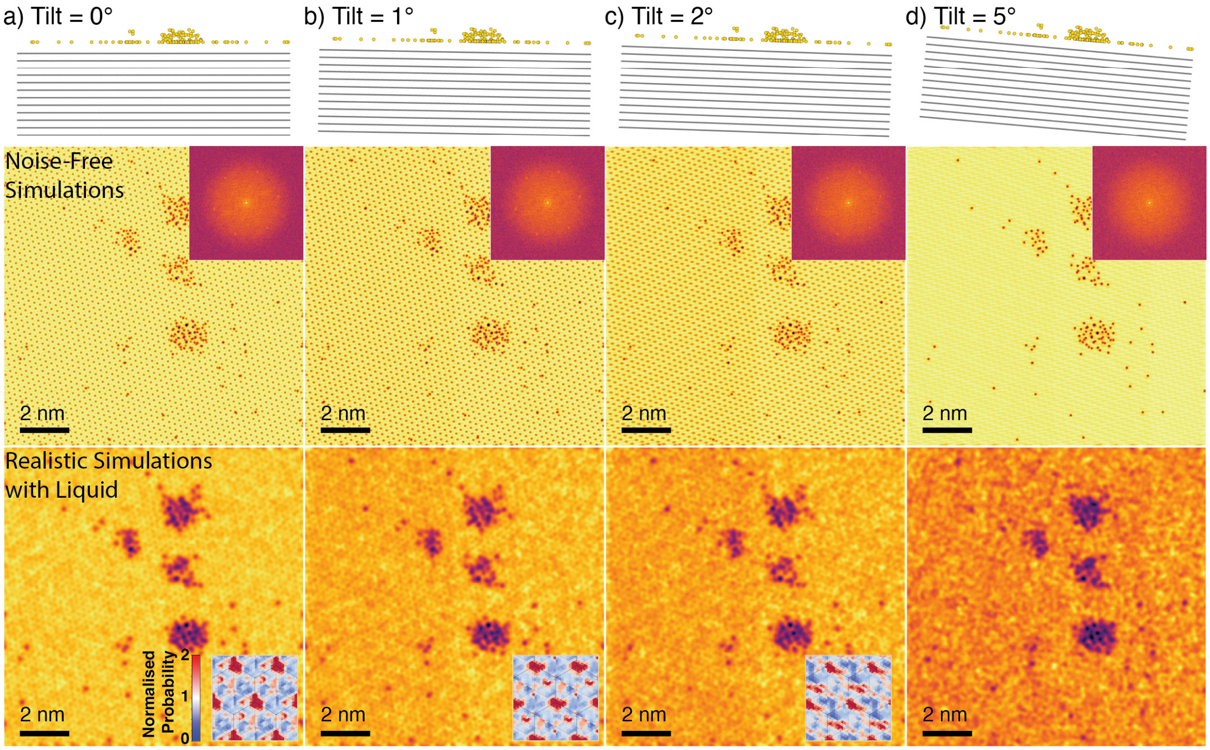

Figure S10: Simulated bright field STEM images at a variety of tilt angles. *Tilted atomic models of the structure have been simulated for tilt angles of 0°, 1°, 2° & 5° (a-d respectively). The top row shows atomic models used for the STEM simulations. The middle row shows noise-free BF STEM images, with the insets showing their FFTs. Simulations including a realistic noise level for imaging a in liquid cell are shown in the bottom row. The inset shows the gold adatom resting site probability based on the simulated image (not shown for the 5° as the lattice was not able to be tracked). Note the gold atom positions were tracked from the corresponding simulated HAADF STEM images.*

3. Liquid Cell Fabrication and Characterisation

The GLC structure consists of two few-layer graphite (FLG) windows either side of a lithographically etched hBN spacer layer. The structure is formed through the successive pickups of the mechanically exfoliated 2D materials using adapted silicon nitride cantilevers (Fig. S11)(*44*). Schematic illustrations of the fabrication steps are shown in Fig. S11.

This GLC fabrication approach detailed here significantly increases the GLC yield and reduces the fabrication time down from ~3 days(*32*) to ~1 hour. We show in this work that submerging the cantilever in the liquid intended for encapsulation offers a greater degree of control over the concentration within the GLC compared to the previous method of drying-mediated sealing. This earlier technique involved the addition of a small aliquot of liquid between the flakes before sealing, which did not allow for precise control over the liquid's concentration(*38*). Additionally, with our new GLC synthesis approach the encapsulated liquid is no longer limited to aqueous solutions, as the cantilevers do not exhibit the solvent restrictions that polymer-based transfers do. The removal of polymeric supports from the transfer process eliminates transfer residue as a potential source of contamination, and increases the cleanliness of the GLC(*30*). The development of the holey cantilevers has allowed for the direct imaging of the sample as suspended without removing it from the cantilever, as shown in Fig. S12.

Target flakes are mechanically exfoliated from bulk crystals onto an oxidized silicon wafer (290 nm) and selected using optical microscopy and atomic force microscopy (AFM)(*61*). The thickness of the hBN spacer layer can be chosen depending on experimental requirements, although the lateral size of the wells needs to be adjusted to the thickness as the windows can collapse if the cells aspect ratio is too low(*32*). Generally, for a 30-50 nm thick hBN we used a cell diameter of 500 nm. Circular cells are patterned into the hBN spacer using electron beam lithography to pattern a polymer etch mask, followed by reactive ion etching (using CHF_3 and O_2) to selectively remove hBN. A short oxygen etch is used to remove the top layers of fluorinated polymer and to functionalise the interior surface of the hBN cavities to make them more hydrophilic. The polymer etch mask is then removed by cleaning in organic solvents. The patterned hBN was then exposed to an alkaline developer (Microposit MF-319 from Kayaku UK) to slightly etch the surface oxide of the silicon wafer, making it easier to delaminate the flake during transfer. Subsequently, the patterned hBN was annealed in a reducing atmosphere (low pressure H_2/Ar) to remove any remaining polymeric contamination from the etch mask.

The optimal thicknesses for the FLG windows are in the 3–5 nm range, which provides stability under electron illumination without causing excessive scattering to degrade the achieved imaging resolution. Additionally, it is crucial that the selected crystals are flat and free from any visible bubbles or cracks to ensure a hermetic seal is formed(*78*). Firstly, the metal-coated cantilever is aligned, using a micromanipulator and optical microscope, so that the array of holes in the cantilever is directly over the target FLG crystal, with the cantilever held at an angle of 15° to the horizontal. Then the cantilever is lowered into the crystal with the substrate held at an elevated temperature of approximately 140 °C. After a few seconds in contact, the cantilever is raised, peeling away the crystal from the substrate (Fig. S11a). The cantilever (with top FLG crystal attached) is then aligned over the patterned hBN so that the cavities in the hBN overlap with the holes in the cantilever, then the cantilever with the FLG crystal is brought into contact with the patterned hBN (at approximately 140 °C). The cantilever is then slowly raised, delaminating the hBN from the substrate (Fig. S11b).

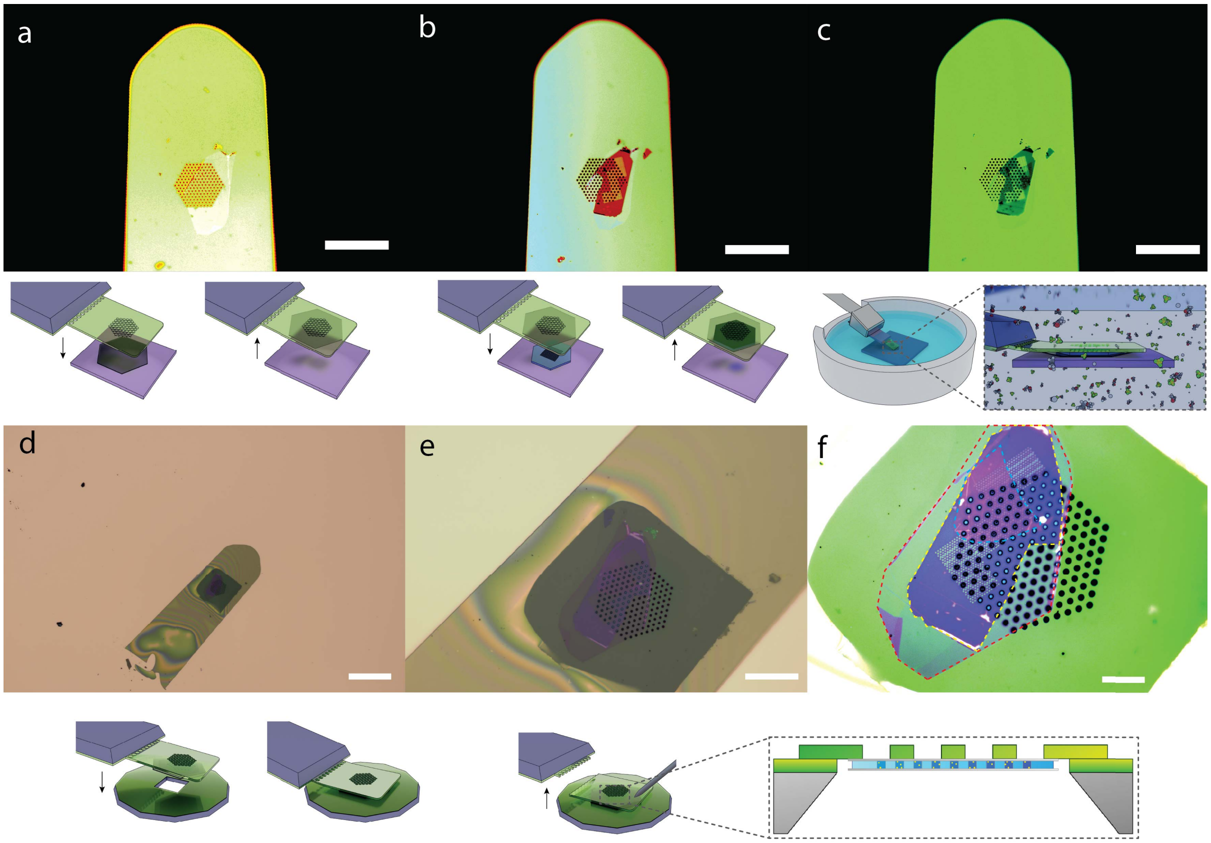

Figure S11: GLC fabrication process. *(a) Picking up the selected FLG flake using a perforated cantilever to act as top window. (b) Alignment and picking up of the patterned hBN spacer layer. (c) The cantilever is used to pick up the bottom FLG window while the system is immersed in the target liquid sample, trapping it inside the cavities in the hBN spacer layer, before being retracted to pick up the bottom window. (d-f) The cantilever is brought to a SiNx TEM grid with a central aperture and fractured such that the cantilever spans the aperture. The scalebars are: (a-c) 100 µm, (d) 200 µm, (e) 50 µm and (f) 20 µm.*

The cantilever containing the top FLG and the patterned hBN are aligned over the bottom FLG and brought near to contact. Then the whole system is submerged in the target liquid sample within the transfer container, as illustrated in Fig. S11c. The liquids encapsulated within the GLCs are all 16 mM $HAuCl_4.3H_2O$ (Sigma-Aldrich UK), using one of the three solvent systems (acetone, cyclohexanone or a 3:1 mixture of deionised water (DI) water and isopropanol). The cantilever is brought into contact with the bottom FLG, thereby trapping liquid within the cavities in the hBN and forming the sealed GLC. This step is performed at room temperature due to the volatile nature of the solvents used for the encapsulations, as any heat applied during the transfer would further exaggerate the evaporation. The cantilever is then lifted slowly so that the bottom FLG delaminates from the substrate and the entire sealed GLC remains on the cantilever (Fig. S11c). The area available for liquid cell TEM imaging comprises the area of overlap between the bottom FLG, the hBN cavities, the top FLG, and the cantilever perforations (four of these locations are highlighted within the inset in Fig. S12e).

To facilitate imaging in the TEM, the cantilever is then lowered onto a TEM-compatible custom fabricated Si/SiN_x 3 mm grids, with a central through-hole larger than the array of holes in the cantilever, but smaller than the width of the cantilever, such that the imaging area is maximised, but the cantilever has sufficient support to remain mounted. The SiN_x grids are based on those described by Hamer et al.(*79*) The TEM support is also sputter coated with metal (Ta 1 nm and Au 20 nm) to promote the adhesion of the metallized cantilever to the support. The metal coated grids are oxygen plasma cleaned immediately prior to the mounting of the cantilever to remove any residual contamination. The cantilever is aligned so that the holes overlay the large through-hole in the support, then lowered until in contact. A secondary manipulator with a needle attachment is used to fracture the cantilever at the base, resulting in the cantilever tip being removed from its support and left on the TEM-compatible grid for imaging (Fig. S11d).

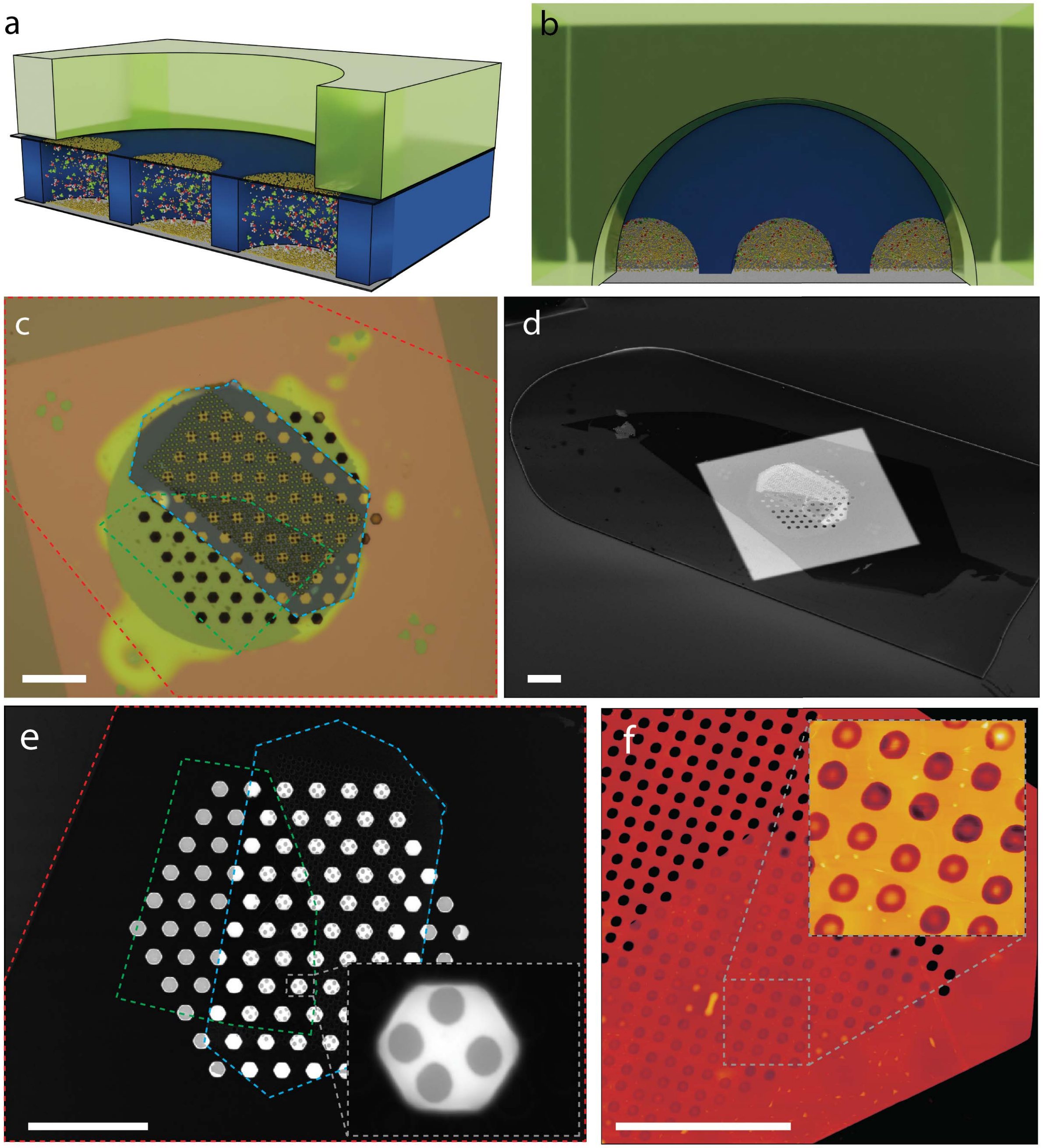

Figure S12: Graphene liquid cell structure. *(a,b) Schematics of the graphene liquid cell structure mounted on the silicon nitride cantilever. (c) Optical image of the GLC and cantilever mounted on the TEM grid. (d) Tilted scanning electron microscope (SEM) secondary electron images of a GLC on the cantilever. The cantilever is mounted on a TEM compatible grid. The bright region in the centre is the suspended region. (e) SEM images of a GLC on the cantilever. The hexagonal holes are in the cantilever, and the circular holes are in the hBN. The inset highlights a suspended region of the GLC for transmission-based imaging containing 4 individually sealed cells. (Green and red dashed lines in c and e indicate the few layer graphene flakes. Blue dashed line indicates the edge of the hBN spacer). (f) AFM image of the GLC. All scalebars are 20 µm.*

Confirmation of the liquid filling of the sealed wells in the GLCs for both acetone and cyclohexanone were performed using STEM EELS imaging. The oxygen K edge was used to map the distribution of the organic solvents as reported in previous GLC studies (see Fig. S13 and Fig. S14)(*32, 80*). Non-negative matrix functionalisation (NMF) decomposition(*81, 82*) was applied to the EELS signal to separate out components attributed to background, nitrogen, oxygen and noise (see Fig. S15). Decomposition with higher output dimensions resulted in only additional noise components.

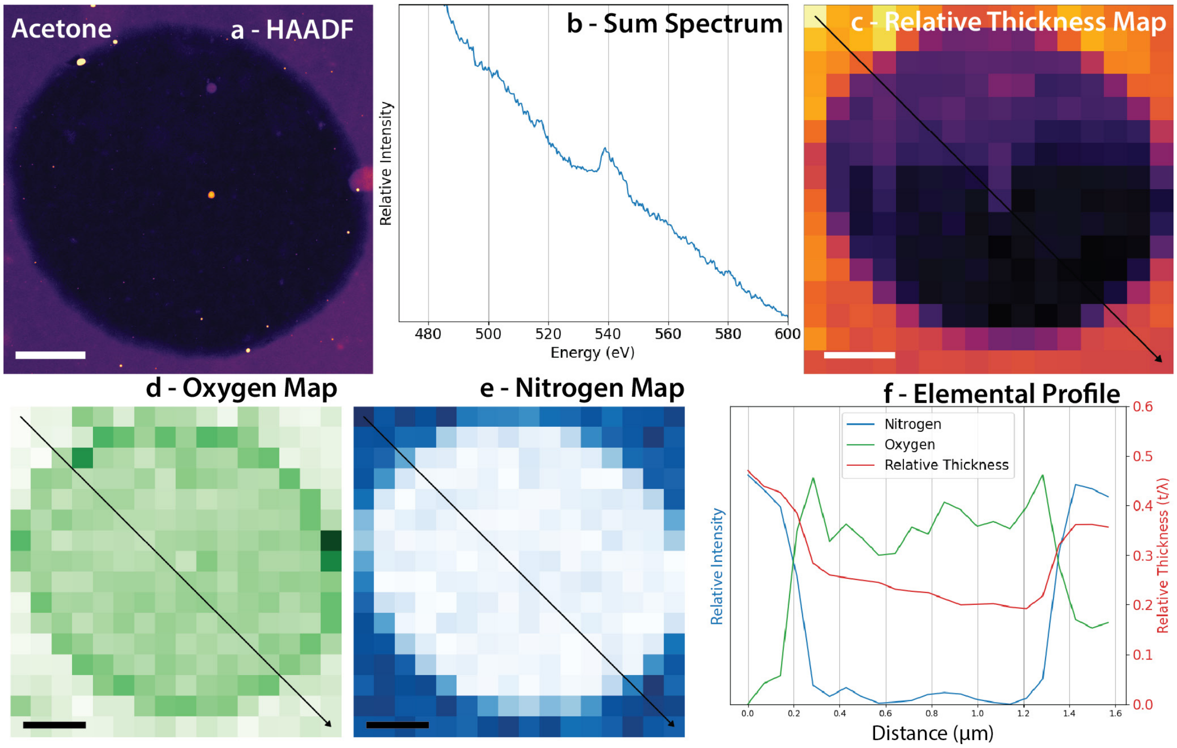

Figure S13: STEM electron energy loss spectroscopy characterisation of an acetone containing GLC. *(a) HAADF-STEM image of a complete well in the liquid cell. (b) Sum EEL spectra from the area shown in (a) exhibiting a clear oxygen K edge with onset ~532 eV. (c) Mapping of the relative thickness (normalised using electron mean free path, t/λ) determined from the low loss EEL spectra using the log ratio method(83). Intensity maps of the oxygen (d) and the nitrogen (e) K edges. The maps were extracted using a non-negative matrix factorisation decomposition using Hyperspy(81). (f) Profiles for the relative thickness, oxygen, and nitrogen mapping. The locations for the line scans plotted in (f) are depicted by the diagonal arrow in each of the respective plots ((d) and (e)). All the scalebars are 150 nm.*

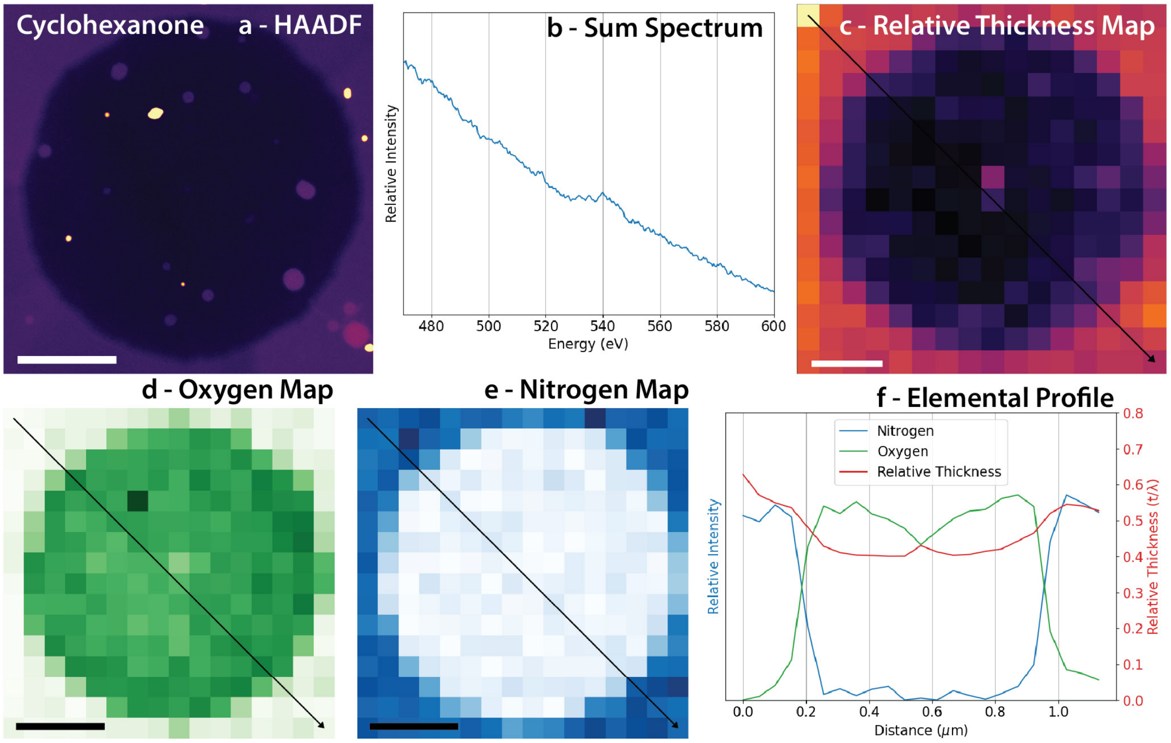

Figure S14: STEM electron energy loss spectroscopy characterisation of a cyclohexanone containing GLC. *(a) HAADF-STEM image of a complete well in the graphene liquid cell. (b) Sum EEL spectra from the area shown in (a), exhibiting oxygen K edge with onset ~532 eV. (c) Mapping of the relative thickness (normalised using electron mean free path, t/λ) calculated from the low loss EEL spectra using the log ratio method(83). Intensity maps of the oxygen (d) and the nitrogen (e) K edges. The maps were extracted using a non-negative matrix factorisation decomposition using Hyperspy(81). (f) Profiles for the relative thickness, oxygen, and nitrogen mapping. The locations used for the line scans plotted in (f) are depicted by the diagonal arrow in each of the respective plots in (d) and (e). All the scalebars are 150 nm.*

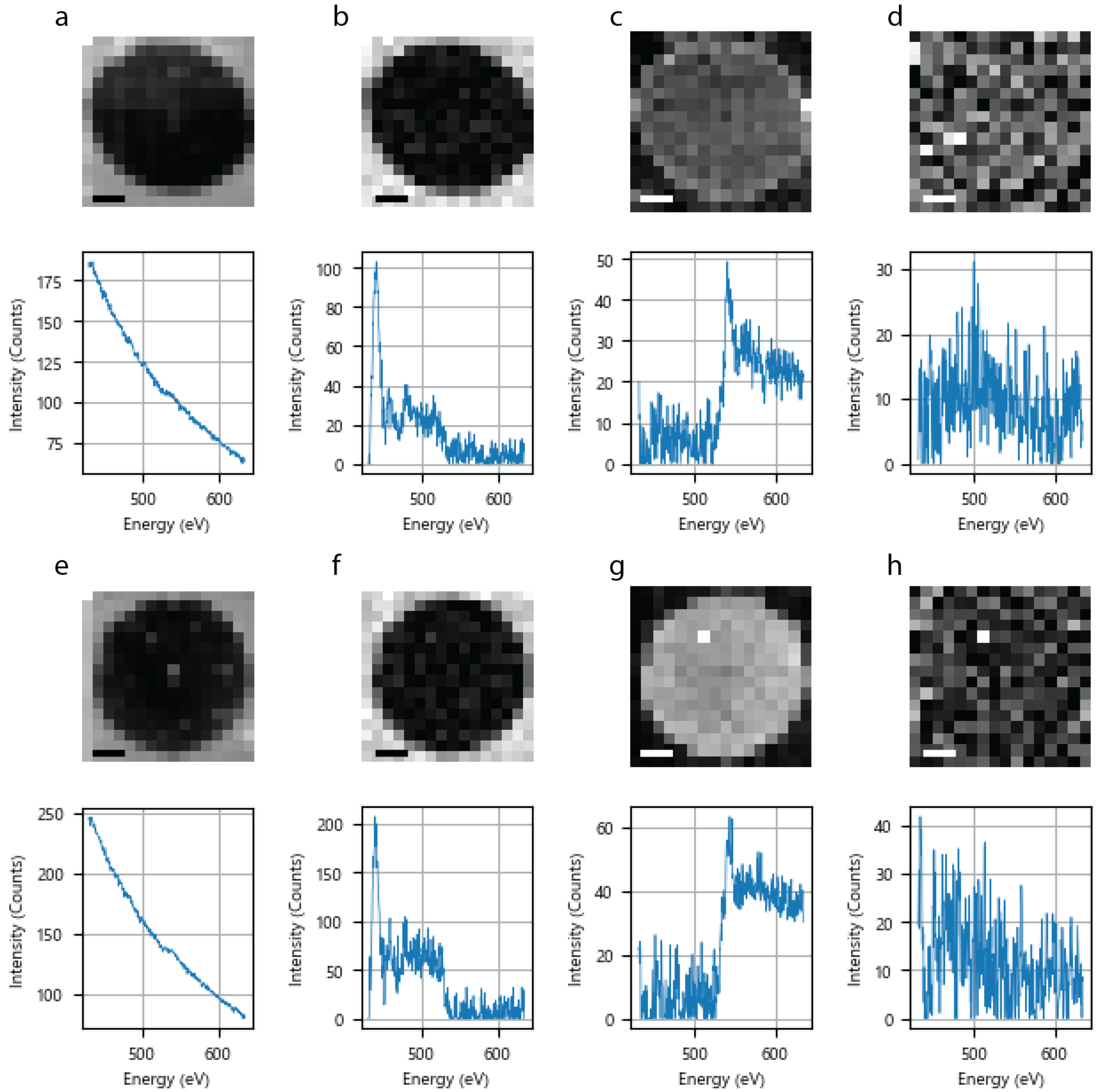

Figure S15: EELS signal decomposition. *The eigenvectors and eigenvalues from non-negative matrix functionalisation (NMF) decomposition of the EELS signal from the GLCs used within Fig. S13 (a-d) and Fig. S14 (e-h). The decomposed signals can be attributed to (a,e) background, (b,f) nitrogen, (c,g) oxygen and (d,h) noise. All scale bars are 150 nm.*

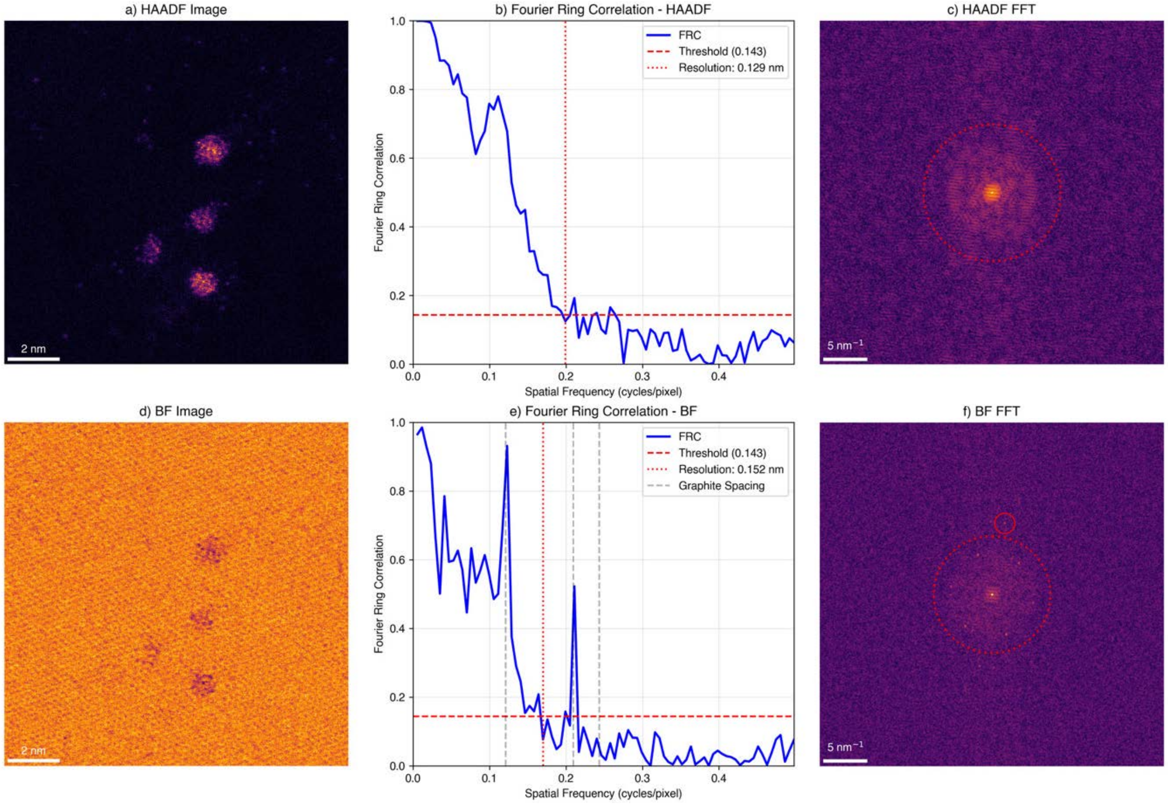

Figure S16: Fourier ring correlation in graphene liquid cell. *HAADF (a) & BF (d) STEM images. The Fourier ring correlation for the HAADF (b) & BF (e) images. FFTs for the HAADF (c) & BF (f) images, with the red dashed ring indicating the Fourier ring correlation resolution.*

The spatial resolution of the HAADF & BF images for the is established through the single image Fourier ring correlation(*84*). The image is split using the checkerboard approach, and a threshold for the ring correlation of 0.143 is used. The estimation of the resolution obtained for the example GLC image from this method is 0.129 & 0.152 nm for the HAADF & BF images respectively. While the vacuum is 0.160 nm for both the HAADF & BF. The resolution estimation is conservative as there is higher frequency lattice information outside the estimate, highlighted by the solid red circle in Fig. S16f & Fig. S17f.

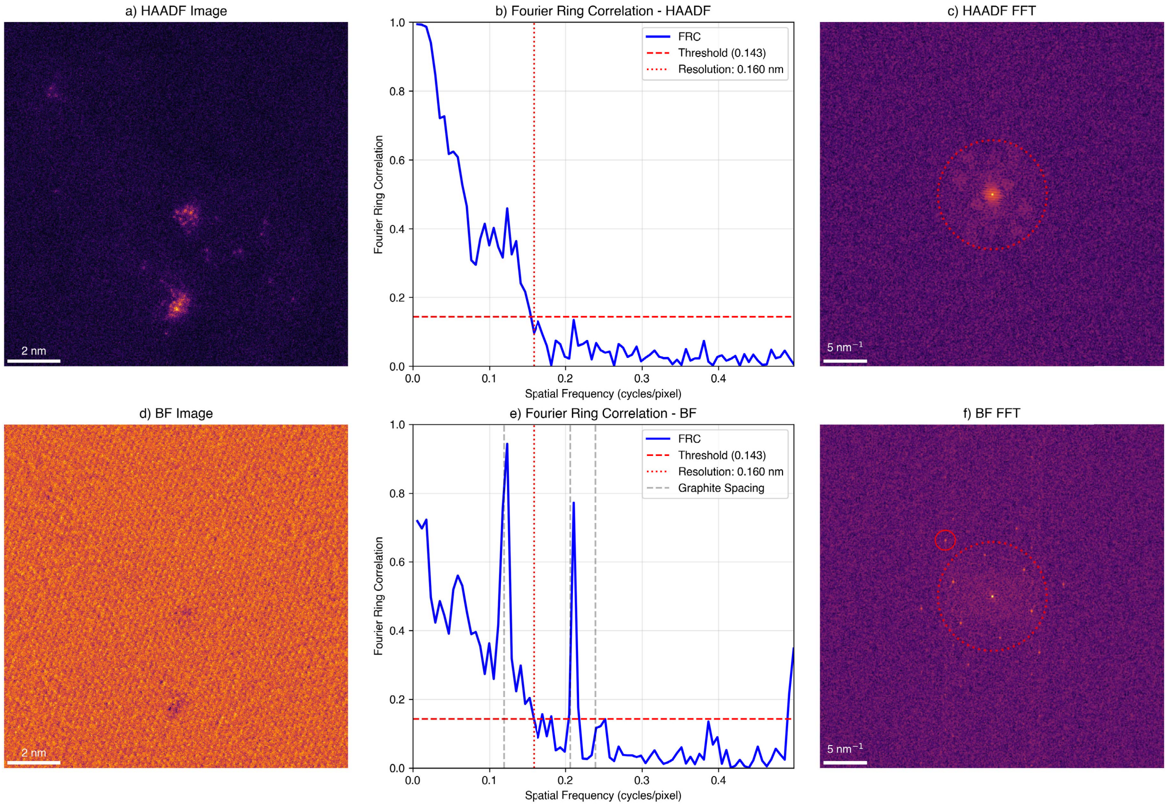

Figure S17: Fourier ring correlation in vacuum. *HAADF (a) & BF (d) STEM images. The Fourier ring correlation for the HAADF (b) & BF (e) images. FFTs for the HAADF (c) & BF (f) images, with the red dashed ring indicating the Fourier ring correlation resolution.*

4. Image Processing

The image processing and atom tracking workflow was employed to identify over 1,000,000 isolated gold adatom positions. The analysis was performed using Python, incorporating functionality from existing open source Python packages including: Hyperspy(*81*), Trackpy(*64*), Scikit image(*85*), Scikit learn(*82*), and Pytorch(*86*). This workflow was applied to all ~150 dual-channel (simultaneous) HAADF- and BF-STEM videos, resulting in the measurement of approximately 250,000 adatom positions per sample type. A detailed summary of this image processing workflow, which facilitated the precise determination of both gold adatom and graphene lattice positions from the HAADF- and BF-STEM images, is presented in Fig. S18. The initial preprocessing of the data is the denoising using a Noise2Void(*87, 88*) convolutional neural network (Fig. S18b). The network was trained on the experimental data, and then the trained network was applied to that data, to produce the denoised videos and images. A single network is used for both HAADF and BF channels.

The lattice sites corresponding to the atomic columns in the in-focus graphite window were extracted from the BF channel using patch-based template matching(*36, 63*) and Fourier filtering to average matching templates across the entire image(Fig. S18 g,h)(*63*). To achieve this, we first extract the templates on a grid, template size 0.82 × 0.82 nm – (32 × 32 pixels) from the denoised image. The magnitude spectrum (amplitude of the 2D Fourier transform) of each of the templates is compared to the averaged magnitude spectrum, to identify the templates most representative image. The best matching templates were selected (examples are shown in Fig. S18g) and cross correlated with the original image. Cross-correlated maps were then filtered in Fourier space, using a periodic mask derived from the original image, using the 6 characteristic graphene spots plus the central spot. Each spot in the mask has a radius of 5 pixels and has been Gaussian filtered. Peak finding is then performed on the Fourier-filtered cross-correlation maps, locating where the template is well correlated with the original image. The frame is rebuilt by placing the template at each of the identified locations matching locations, weighted by goodness of fit. The result of this is a rebuilt image frame per template. The reconstruction process is then completed by summing the rebuilt frames from a range of sample templates to form a unified reconstructed image, as shown in Fig. S18h. This process is repeated on a frame-by-frame basis for each video. This process improves the clarity of the periodic graphene lattice throughout the frames, through the removal of non-periodic or non-repeating features within the image. Generally, these are from contamination or particles. They reproduce the best matching lattice only locally, so this allows for a larger than mask scale strain, or imaging distortions. The lattice localisation is then used for drift correction as it allows for the comparison of adatom motion relative to substrate, as well as identifying the Au adatom resting sites on the lattice. Drift correction was performed by linking nearest neighbour lattice sites in adjacent image frames through the application of the Trackpy package(*64*) using a Crocker-Grier algorithm(*65*) contained within the package, and subtracting the ensemble motion from each frame. The comparison of the denoised BF image (Fig. S18c) to rebuilt BF image (Fig. S18h) shows enhanced lattice contrast, enabling the tracking of the graphite atomic structure even when the image has poor signal to noise ratio.

The gold adatom positions were established using peak finding on the Noise2Void denoised HAADF-STEM images with thresholding applied (Fig. S18 e,f). Similar to the BF case, the Crocker-Grier algorithm(*65*) within Trackpy(*64*) was used for the linking of the adatom positions into trajectories. The trajectories were then drift corrected using the drift values obtained from the BF signal (Fig. S18i).

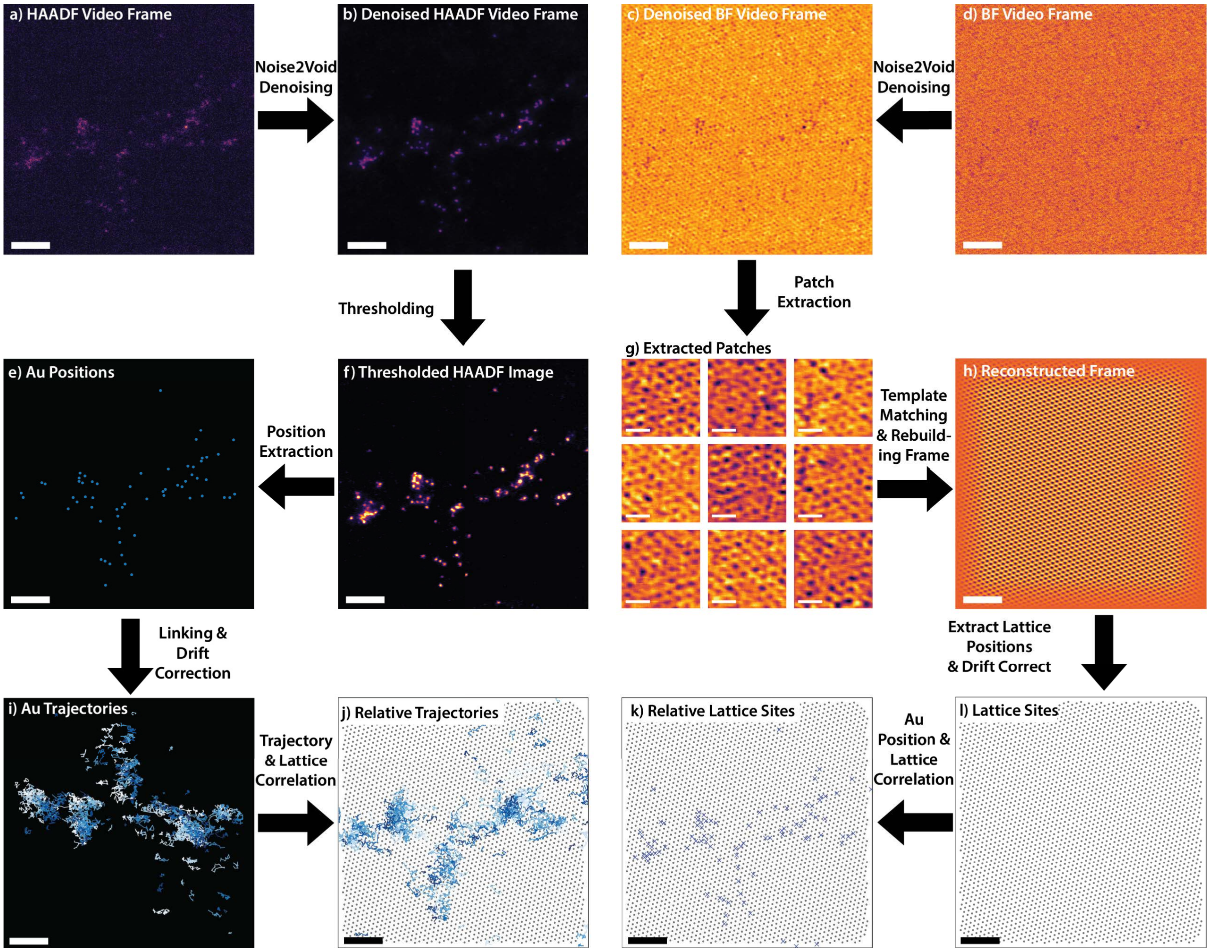

Figure S18: Image processing and atom tracking workflow. *The panels are described in section 4. The scalebars are 2 nm except in g which are 0.5 nm.*

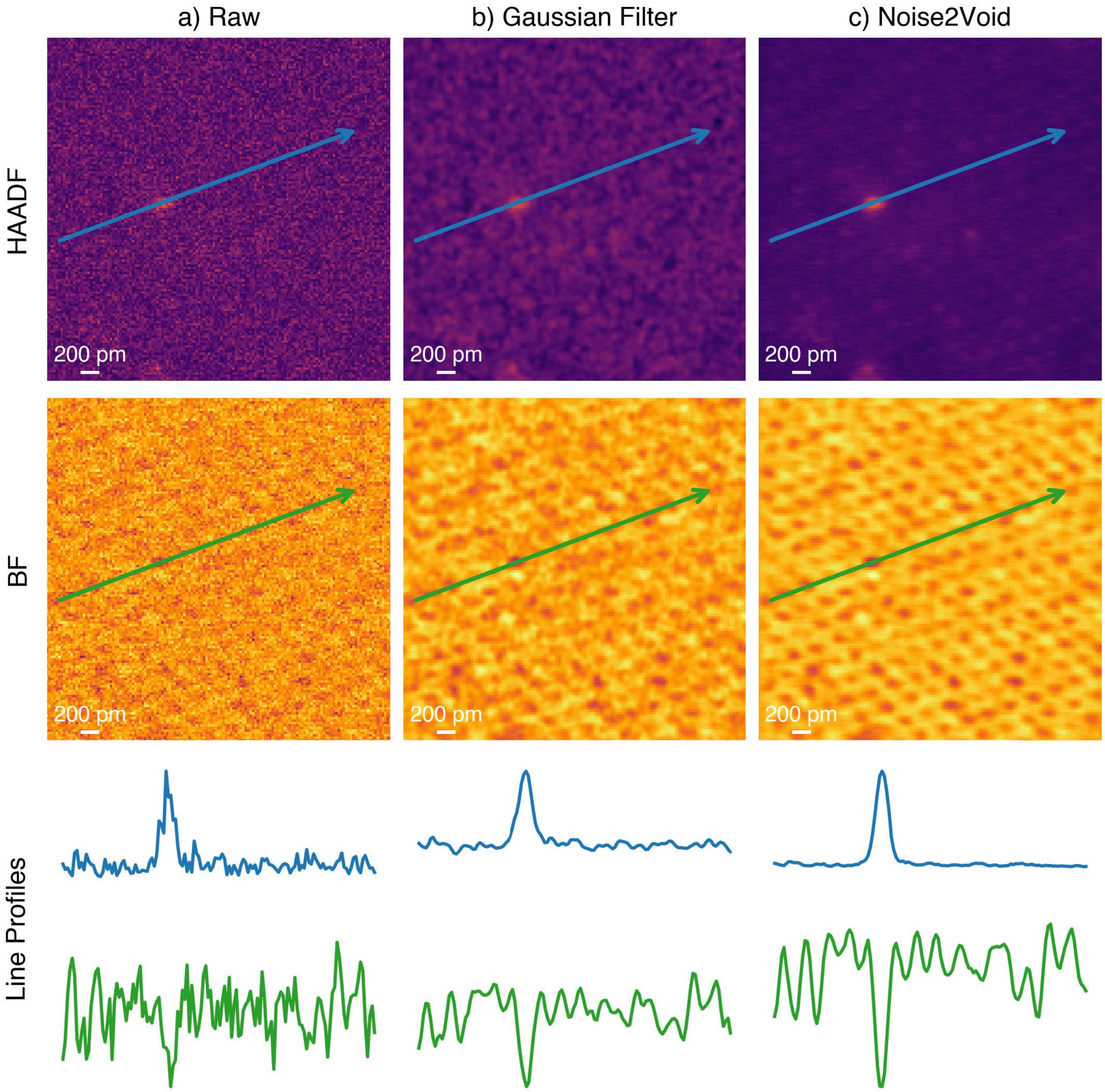

Figure S19: Denoising of the HAADF & BF STEM images from a graphene liquid cell. *An example cropped region of the HAADF & BF STEM images an isolated gold adatom, for the raw (a), gaussian filtered (b) & Noise2Void denoised (c). Line profiles are shown for the HAADF (blue) & BF (green) below to visualise the reduction in the noise in the images.*

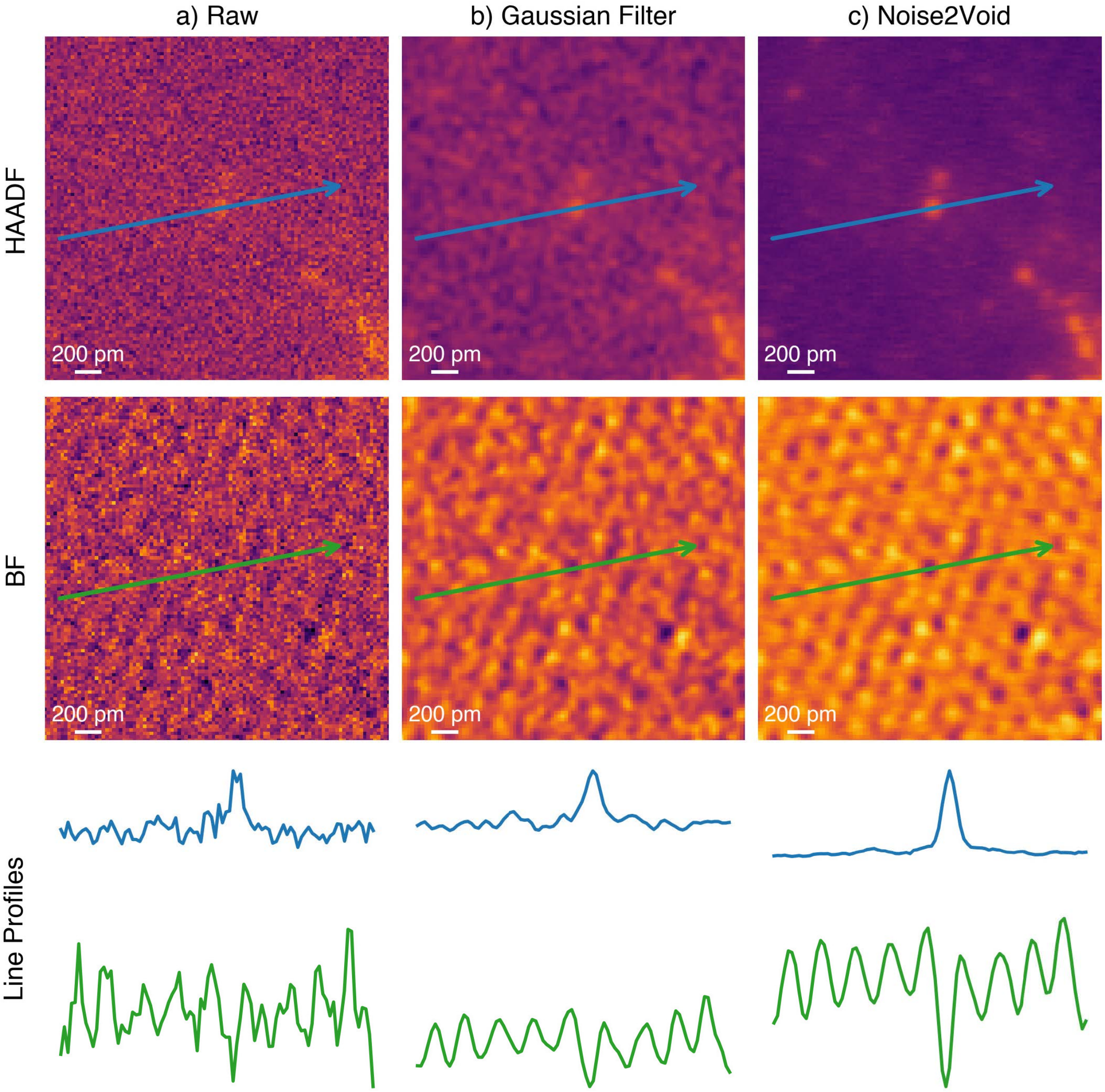

Figure S20: Denoising of the HAADF & BF STEM images from a vacuum environment. *An example cropped region of the HAADF & BF STEM images an isolated gold adatom, for the raw (a), gaussian filtered (b) & Noise2Void denoised (c). Line profiles are shown for the HAADF (blue) & BF (green) below to visualise the reduction in the noise in the images.*

5. Gold Statistics

5.1 Concentration Control

The concentration of the $HAuCl_4.3H_2O$ solutions were 16 mM. This concentration can be converted to a gold atom areal density on the windows by considering the total gold in the solution contained in the GLC (total volume of 5.9×10^6 nm^3, assuming the GLC to be cylindrical with a radius of 250 nm and a thickness of 30 nm) and the surface area of the graphene windows to be 4.4×10^5 nm^2. Assuming all the gold adsorbs to the surfaces of the cell gives an areal density of 0.144 nm^{-2}. In comparison, the gold adatom areal density measured from STEM images of the graphene windows is 0.274 adatoms nm^{-2}. One reason for this factor of ~1.9 difference may be a reduced liquid volume compared to the assumption of a perfect cylinder, resulting from inwards bowing of the windows, behaviour reported in our previous GLC work(*32*). Additionally, a higher than expected concentration could result as there is likely preferential adsorption of the Au to the graphite windows from the solution in the period prior to cell closure (~ 5 minutes). Nonetheless, our demonstrated concentration control is improved over all previous GLCs, which reported concentration differences of up to 3 orders of magnitude(*38*).

5.2 Gold Distribution Calculations

The clustering behaviour of identified Au adatoms was extracted from the coordinate data using the DBSCAN (Density-Based Spatial Clustering of Applications with Noise) clustering algorithm from the Python package scikit-learn(*82*) to group adatoms into clusters and record their size. The size distribution established from this clustering was used to identify the regimes of isolated adatoms, small amorphous clusters, and large amorphous clusters. The maximal separation distance for adatoms to be considered as part of a cluster is 0.4 nm, which was established from the one-dimensional pair distribution functions, as shown in Fig. S24. The cluster size is then used to filter the measured positions to only consider a certain category of the adatoms present (see Fig. S21). The randomly distributed control was simulated by taking the experimentally derived number of Au locations per frame and randomly positioning these within the field of view. This process was then repeated 1000 times and the results averaged. The same size distribution analysis is then performed for the simulated 'random' control adatom locations as for the experimentally derived positions. Three size schemes are highlighted from the size distribution, the isolated species at $n \leq 3$, small amorphous clusters at $4 \leq n \leq 30$ and large amorphous clusters at $n \geq 31$ (where n is the number of gold atomic species identified). Approximately 250,000 isolated adatom positions were measured per sample, with an additional ~300,000 atomic positions from the amorphous clusters across the four samples.

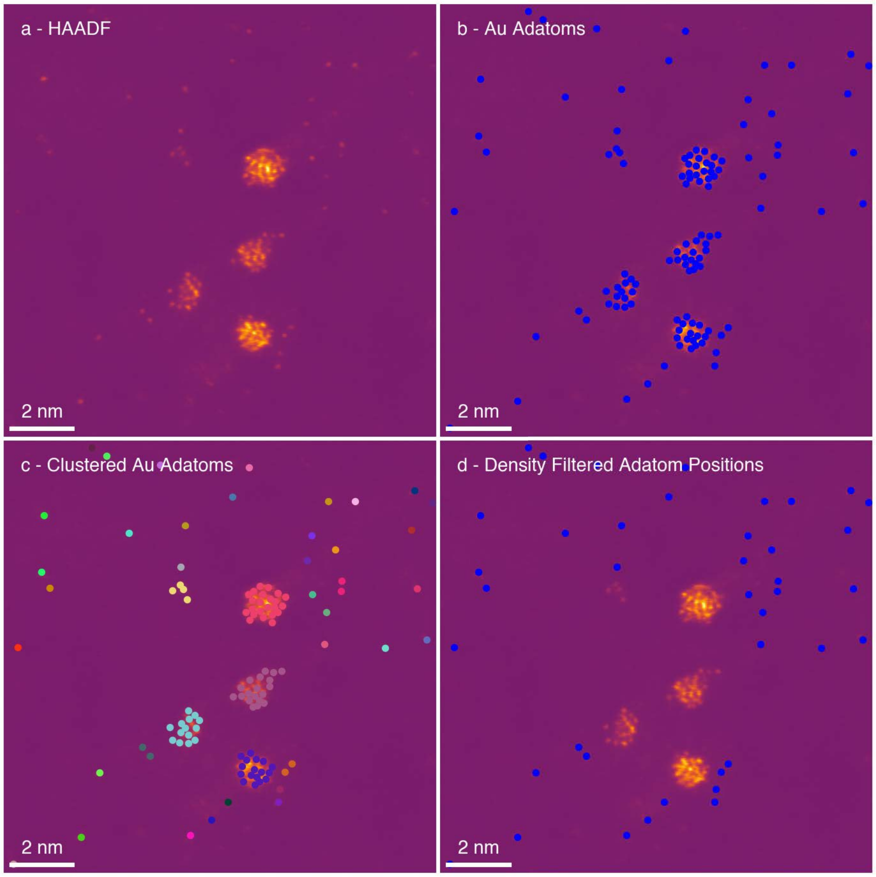

Figure S21: Procedure to remove the clustered Au species from the isolated Au adatom analysis. *(a) Denoised HAADF-STEM image. (b) Identified Au adatom positions. (c) Au positions clustered using a density based spatial clustering algorithm. The DBSCAN clustering package is from scikit-learn (25)(82). The maximum distance for atomic position consideration as part of a cluster is set as 0.4 nm. The clusters are depicted by groups of the same colour. (d) Filtered Au positions to only highlight the isolated Au positions. This analysis used a cluster threshold size of n=4 adatoms (restricting analysis to when n=1,2 or 3)., This threshold cluster range can be changed to extract the number of clusters in the data within different size ranges.*

The gold distribution histograms were determined through measurement of the isolated species, amorphous clusters, and crystalline particles. The numbers of isolated adatoms and amorphous clusters were calculated through the atom tracking from the high magnification HAADF-STEM images then performing size distribution analysis, as discussed previously. The crystalline particle distribution was established from the lower magnification HAADF-STEM images. The mean diameter of each of the crystalline particle was measured, and the volume is determined based on the assumption that these are spherical.

The measured pair distribution functions were obtained by calculating all Au-Au distances within single images and collating them over all images (see Fig. S24). They were normalised by comparison to the same metric measured for the simulated ‘randomly distributed control’ with a matching adatom density. The single frame jump distance was obtained by applying the Crocker-Grier linking algorithm to adatom locations with a conservative maximum distance of 0.7 nm. However, as it is impossible to correctly link indistinguishable atoms from frame-to-frame the distances measured here may underestimate the single-frame motion as the closest pairs are assumed to be linked. To test the importance of this effect, displacements were measured for completely isolated adatoms where there is no other atom within ~2 nm. This data showed similar (albeit noisier) results to data with higher areal density, suggesting minimal distortion is caused by the indistinguishability of adatom tracking, The calculated interaction lifetimes for the adatoms were obtained by taking the adatoms positions that have been linked in the image series and establishing the length of time that the same adatoms remain paired within the paired distance (0.4 nm) of each other, and hence are within a stable dimer or a trimer cluster (see Fig. S25).

The gold thickness at each measured atomic position was determined from the background-subtracted integrated signal intensity. For each tracked atomic coordinate, the signal, I_{loc}, was integrated within a 5-pixel disk ROI centred on the atomic peak; local background was estimated adaptively from an annular region surrounding the ROI and subtracted to minimise background contribution. A single isolated gold atom from the same image was employed as the calibration standard: its background-subtracted integrated intensity was averaged over multiple occurrences to yield the per-atom intensity I_{cal}, and the number of atoms at each site was calculated as $n = I_{loc} / I_{cal}$(*46-48*).

To validate the approach, we used the calibrated atom counts to build a model cluster at the measured positions, generated simulated intensities from that model, and compared experimental and simulated line profiles (Fig. S22). The simulated cluster contains 37 atoms with a maximum projected thickness of four gold atoms, and the close agreement of profiles supports the quantitative conversion from intensity to atom count. Previous studies demonstrate that HAADF intensity follows a linear relation to the atomic column thickness up to 10 atoms(*89*). Therefore, because our measured clusters are below this threshold, departures from strict linearity were not considered to be significant for the present dataset.

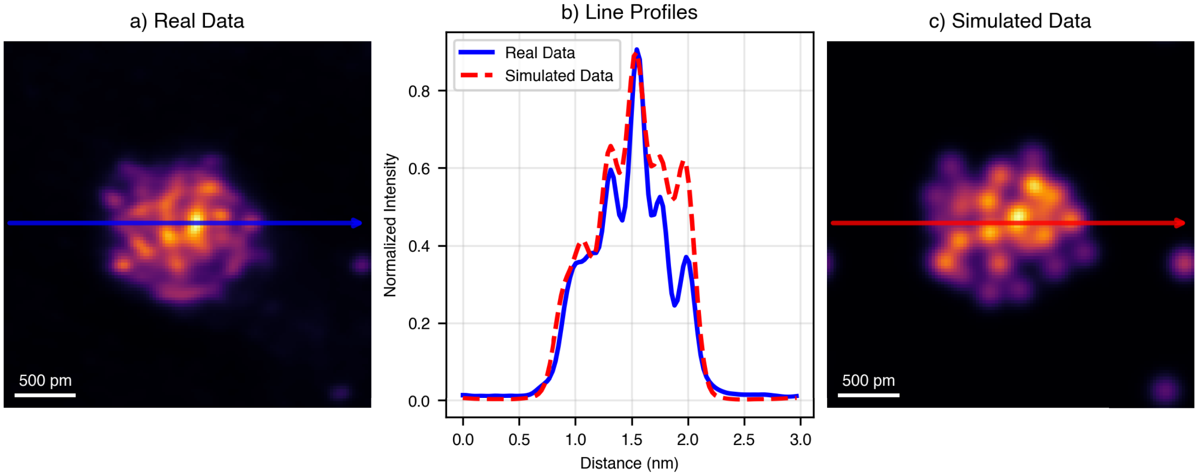

Figure S22: Amorphous cluster thickness mapping. *(a) HAADF STEM image of an amorphous cluster of gold in acetone. (b) Line profiles of the intensity of the cluster for the real (a) and simulated data (c) with the location shown on the respective images (line profile integrated over a width of 5 pixels or 0.13 nm). (c) Simulated HAADF STEM image for the amorphous cluster.*

5.3 Gold Adatom Behaviour

The time dependency of the gold behaviour is shown in Fig. S23 the impact of the electron beam is discussed in section 10.

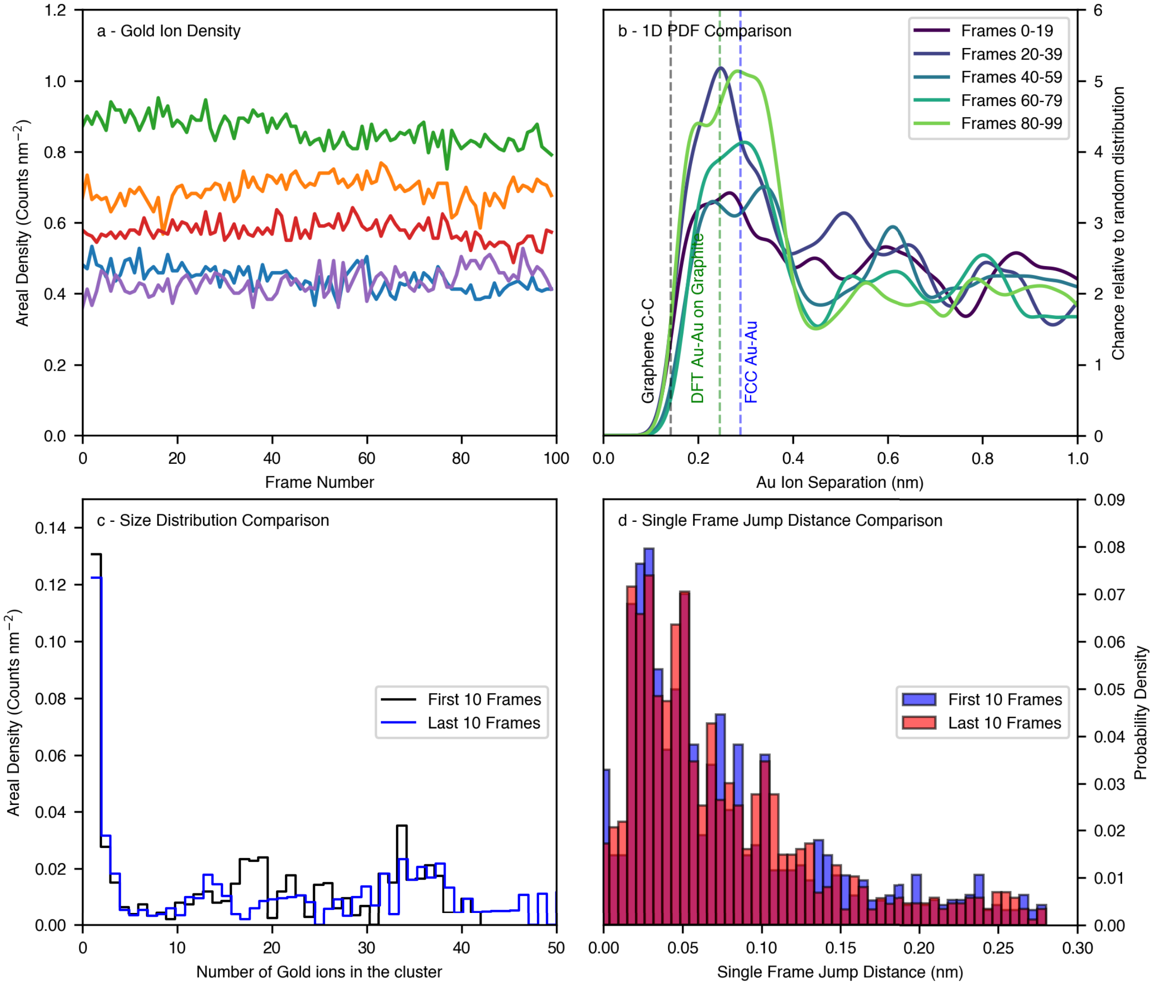

Figure S23: Imaging time dependency of the statistical data for adatom distribution, separation and jump distances. *(a) Comparison of the measured statistics with respect to imaging time are shown for 5 different videos, each of them is 190 s long (100 frames) in length, collected with a probe current oft 1.67 × 10^6 e^- s^{-1} nm^{-2}. Different videos are represented by distinct colours. (b) 1D pair distribution function shown for the average of all positions in the 5 videos in (a), binned into sets of 20 frames. (c,d) Gold cluster size distributions and single frame jump distances, respectively, for the 5 videos summed, comparing the first 10 (frames 0-10) and last 10 frames (frames 89-99).*

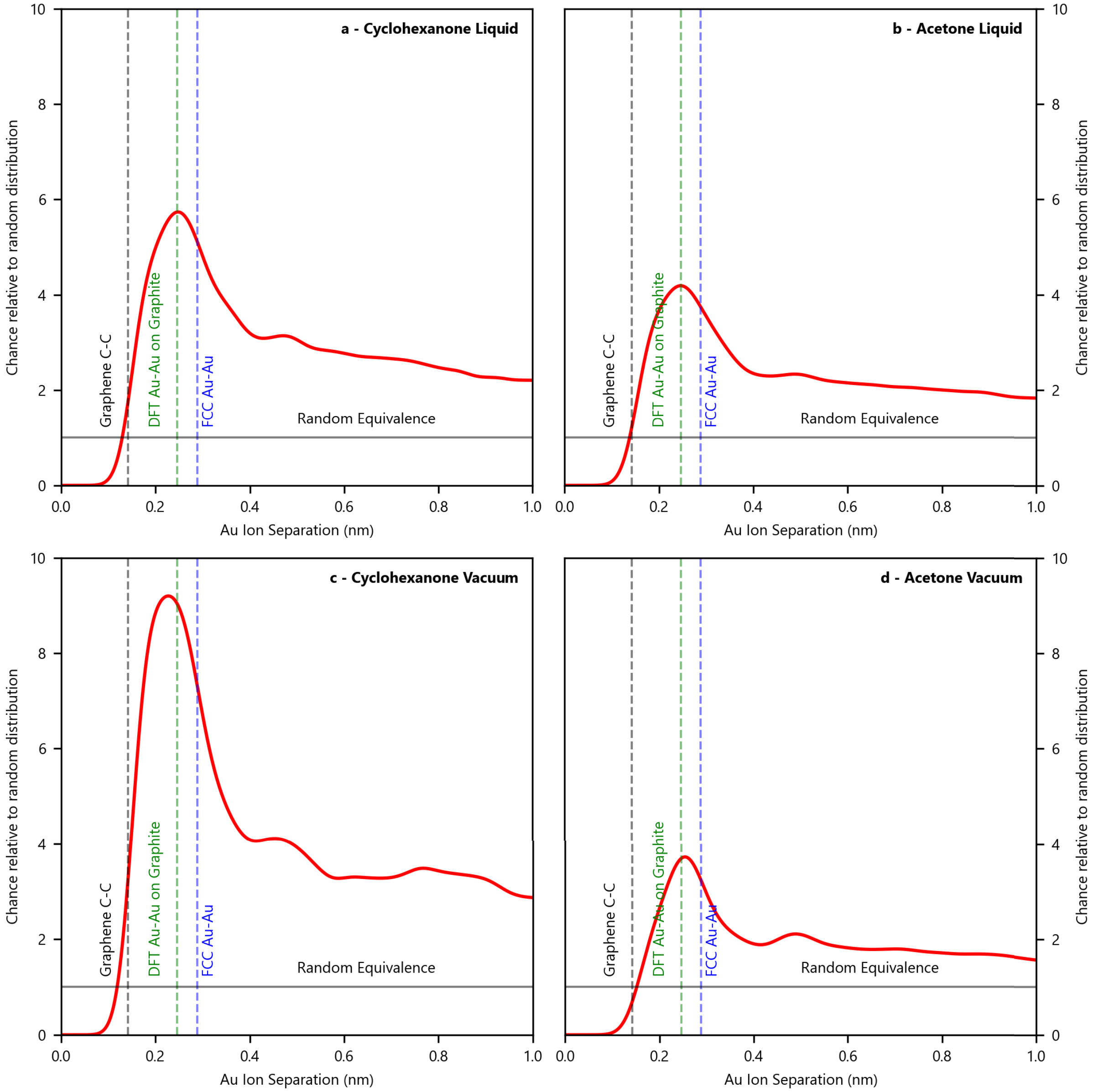

Figure S24: 1D pair distribution functions for the gold adatoms in the different samples. *(a,b) 1D PDFs shown for GLCs containing (a) cyclohexanone liquid and (b) acetone liquid. (c,d) 1D PDFs for unsealed GLC control samples filled with liquid then dried giving (c) cyclohexanone vacuum and (d) acetone vacuum data. The higher intensity for the cyclohexanone is a result of there being more clustered gold.*

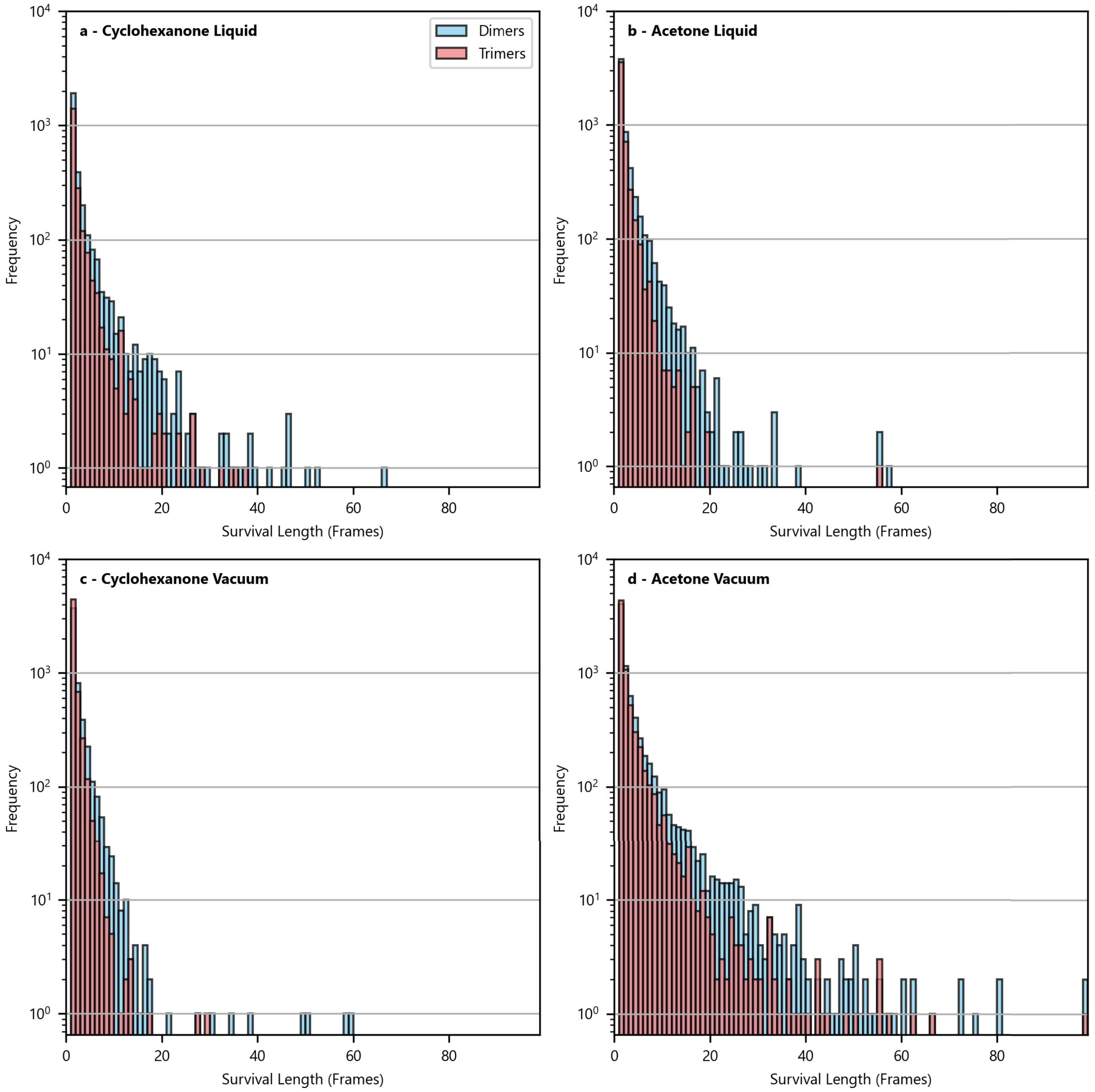

Figure S25: Lifetimes of gold dimer and trimer species within the image series expressed as histograms for the number of frames. *(a,b) Lifetime histograms for GLCs containing (a) cyclohexanone liquid and (b) acetone liquid. (c,d) Lifetime histograms for unsealed GLC control samples filled with liquid then dried giving (c) cyclohexanone vacuum and (d) acetone vacuum data.*

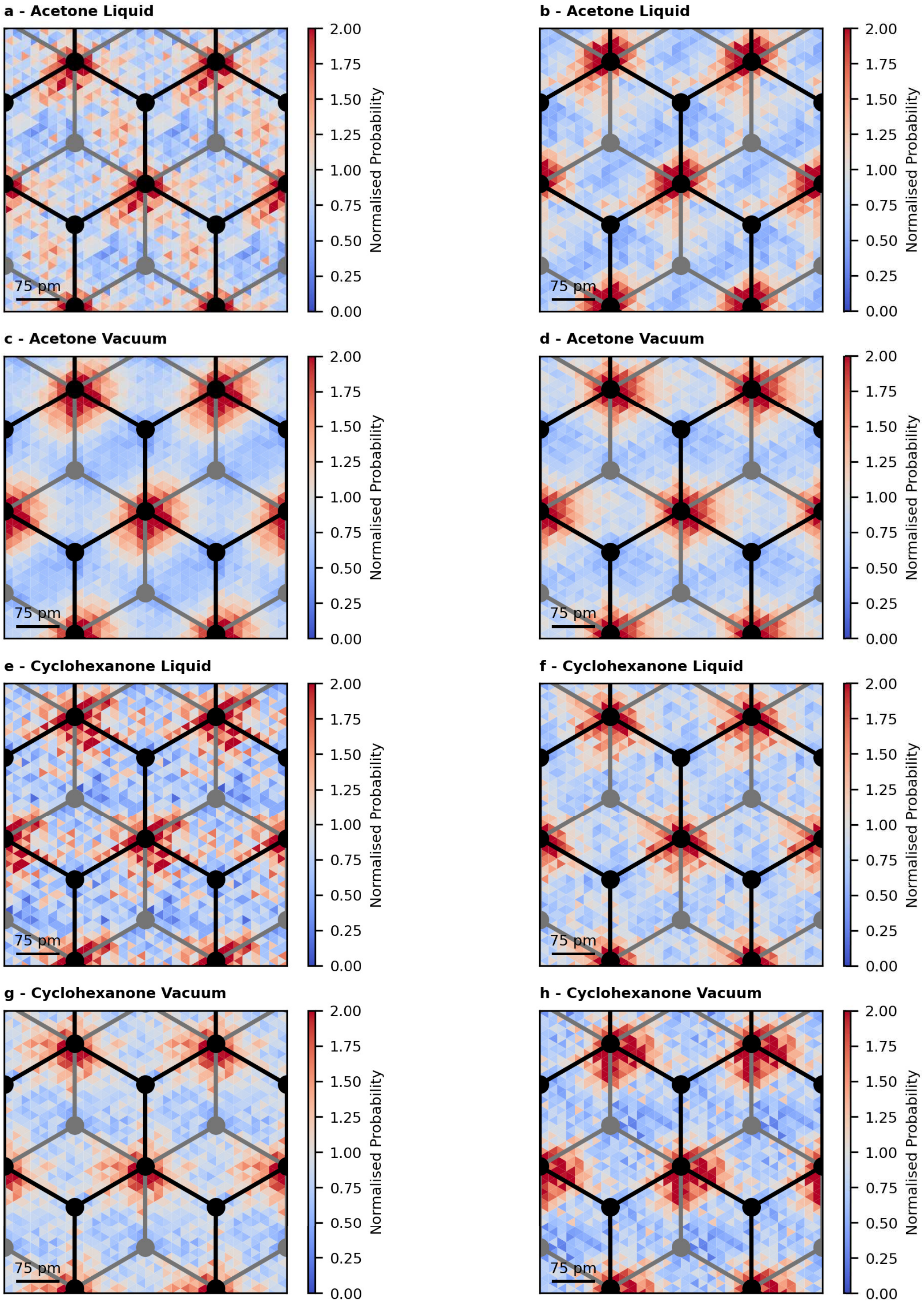

Figure S26: Au resting site probabilities. *The resting site probabilities for the gold on the graphite lattice, each panel represents the probabilities for a single video sequence from each sample type: (a,b) acetone liquid, (c,d) acetone vacuum, (e,f) cyclohexanone liquid and (g,h) cyclohexanone vacuum.*

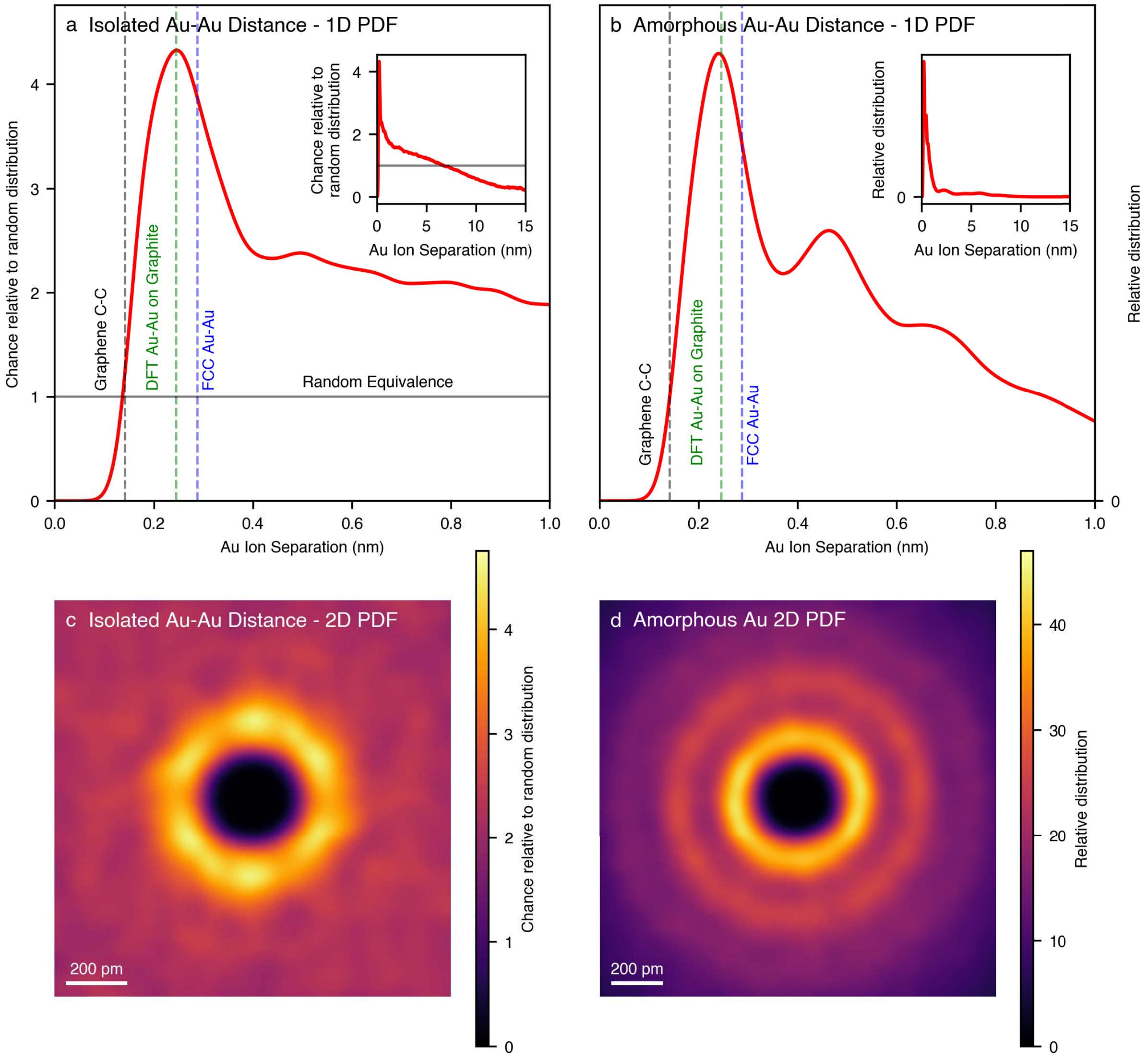

Figure S27: Au-Au pair distribution function. *The pair distribution functions for the Au-Au positions. The 1-dimensional PDFs (a&b), and the 2-dimensional PDFs (c&d). The 1D & 2D PDFs are shown for the isolated gold (a&c) and for the amorphous clusters of gold (b&d).*

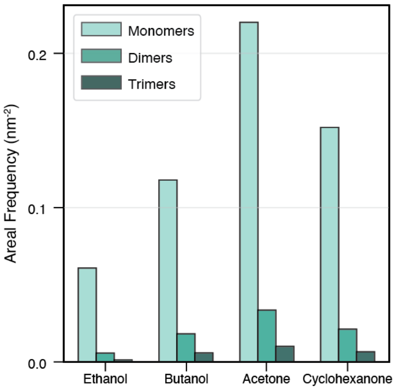

Figure S28: Areal frequency (nm^{-2}) of monomers, dimers, and trimers on the graphite surface in the different solvent systems. *GLCs isolated species were measured for ethanol, butanol, acetone, and cyclohexanone.*

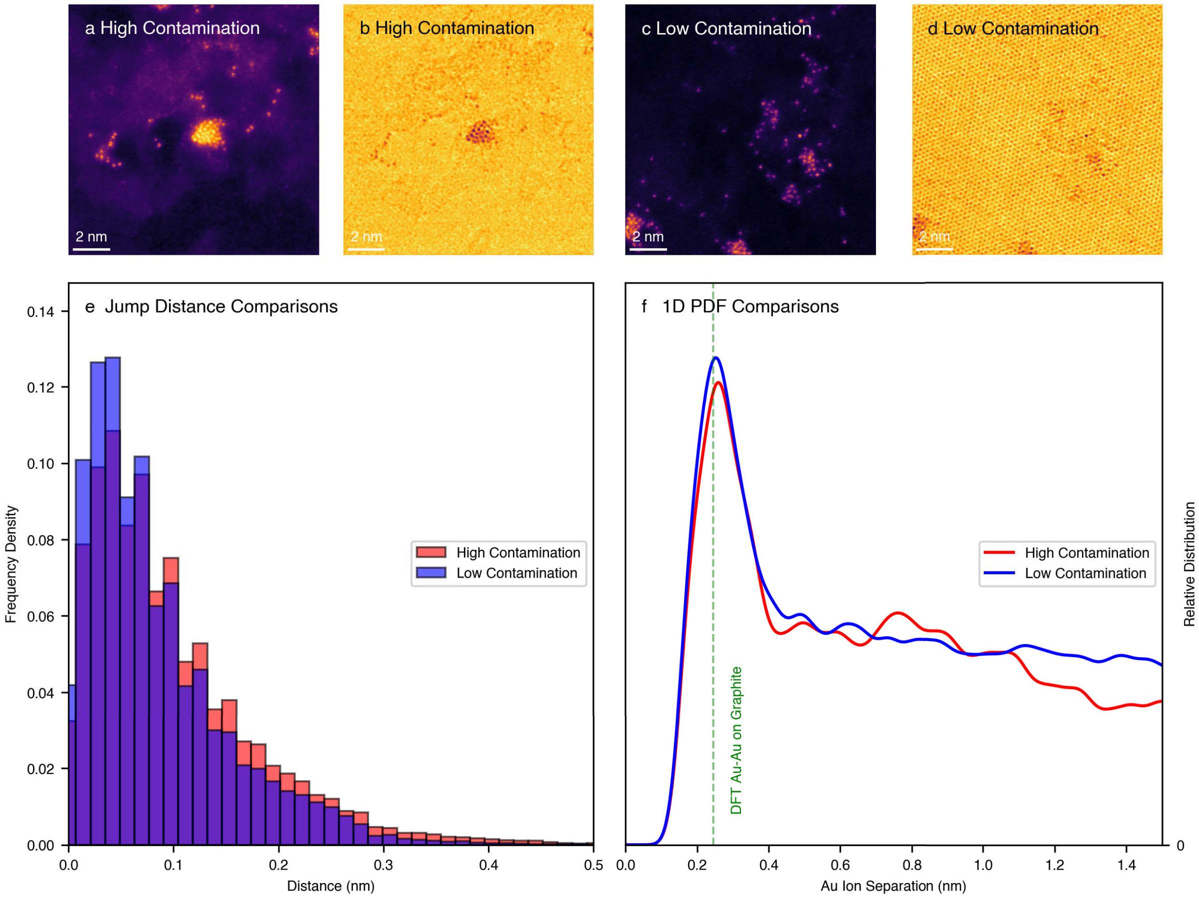

Figure S29: Contamination influence control. *High contamination example (a) HAADF & (b) BF STEM images. Low contamination example (c) HAADF & (d) BF STEM images. The atom tracking of the single frame jump distances (e) and the 1D pair distribution function (f) for the high and low contamination level.*

6. Catalysis

Samples for catalytic measurements were prepared by dissolving the gold salt (6.4 mM $HAuCl_4.3H_2O$, 10 mg in 4 mL of solvent) in the chosen solvent. This is then added to the appropriate weight of graphene powder (0.99 g) to produce an Au catalyst loading of 0.5 wt%, and stirred for 1 hour. The mixture was dried under N_2 for 2 hours at the corresponding temperature for solvent evaporation (acetone, 42 °C, water 105 °C, cyclohexanone 160 °C, ethanol 83 °C, propanol 102 °C, butanol 123 °C) with a ramping rate of 5 °C min^{-1}. HAADF-STEM images of the as-produced materials are shown in Fig. S30.

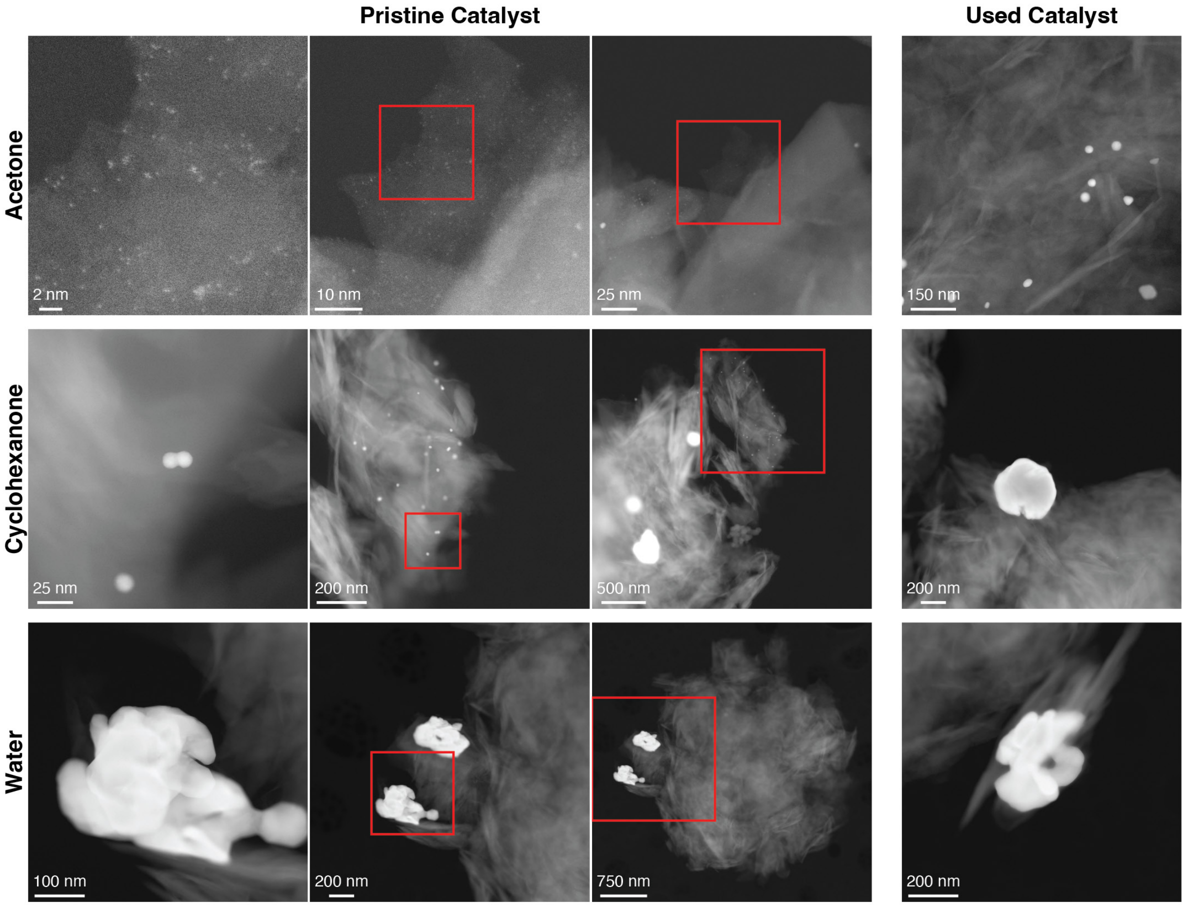

Figure S30: HAADF-STEM images at a range of magnifications for the gold on graphite used for catalytic measurements. *The pristine catalysts were prepared through wet impregnation of* $HAuCl_4$ *with either acetone (top row), cyclohexanone (middle row), or water (bottom row) as the solvent. The red boxes indicate the regions that the higher magnification images to the right are taken. The used catalysts (right column) are those after catalytic testing for the hydrochlorination of acetylene at 160 °C.*

The catalysts were tested for hydrochlorination of acetylene in a fixed bed microreactor. 500 mg of the prepared catalyst was used. The reaction was completed at 160 °C for 4 hours, with a gas flow rate of 5 ml min^{-1}, the gas mixture composed of 1:1.02 (C_2H_2 : HCl) at 1.08 bar (5% C_2H_2 balanced in Ar and 5% HCl balanced in Ar). The gas-phase products were analysed using a Varian CP-3800 GC equipped with a flame ionisation detector (FID) and a Poropak-N packed column. In all cases, VCM was confirmed as the only product. The conversion plot is shown in Fig. S31a.

The acetylene conversion for the cyclohexanone prepared catalyst is believed to be suppressed due to the presence of the cyclohexanone residue on the surface of the graphite. The residues remaining on the surface of the graphite is hypothesised to prevent the adsorption of the reactants to the Au active sites. This residue presence is confirmed via thermogravimetric analysis (TGA), see Fig. S37.

Additional catalysis testing was carried out after different drying temperatures for the water and acetone solvents to test the effect of drying versus the dispersion of metal in the liquid phase. For both solvents when the catalyst is dried at a higher temperature the activity is reduced (Fig. S31c), due to the thermal energy providing increased diffusion of the Au and resulting in an increased particle size. The low boiling point of acetone is therefore key to preserving the favourable atomic dispersion of Au in the liquid phase.

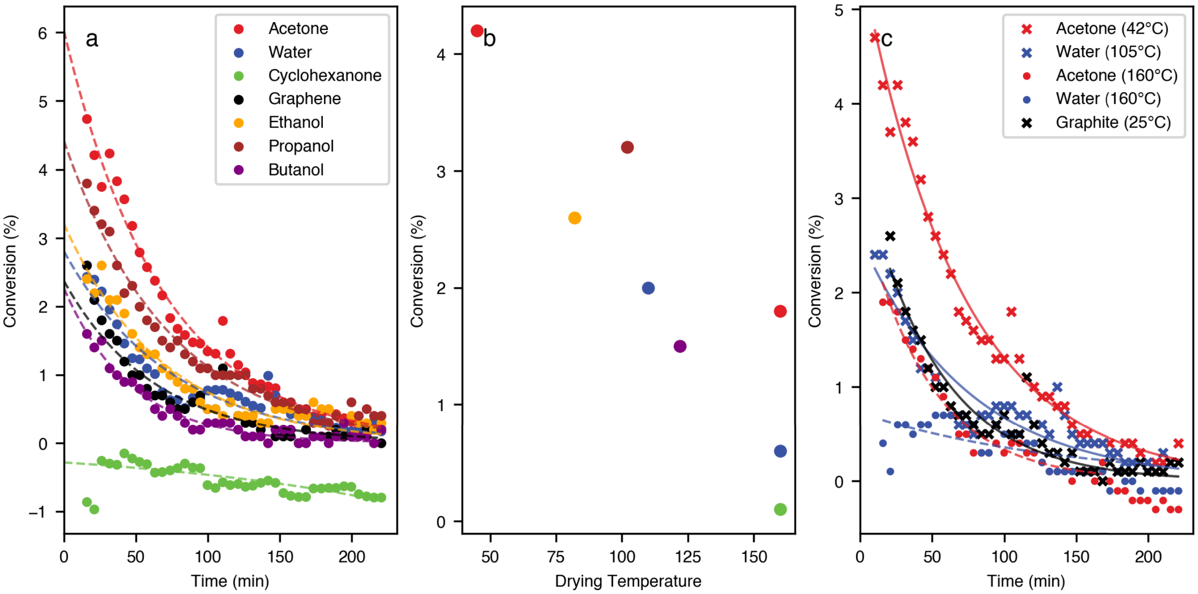

Figure S31: Catalytic performance of the Au/graphite catalyst prepared with different solvents for hydrochlorination of acetylene. *The solvents tested are acetone, water, cyclohexanone, ethanol, propanol, and butanol. The drying temperatures used were close to the boiling points of the solvents, specifically (acetone, 42 °C, water 105 °C, cyclohexanone 160 °C, ethanol 83 °C, propanol 102 °C, butanol 123 °C). Graphene without Au was used as a control (used as received, no heating). (a) The conversion trend has been fitted to a power law. (b) The drying temperature vs conversion at t=26.2 min. Legend is the same as (a). (c) The conversion trend fitted with a power law for catalysts prepared at different temperatures for acetone (42 & 160 °C) and water (110 & 160 °C). It wasn't possible to dry the cyclohexanone at lower temperature due to the high boiling point of this solvent and higher temperature is above the temperature of the reaction.*

7. Density Functional Theory Simulations

7.1 DFT – Au Graphite Sublattice Dependency

Adsorption Energy

We initially calculated the adsorption energy of a single Au atom using DFT total energies,

$$E_{\mathrm{ads}} = E_{\mathrm{cell}} - N^2\epsilon_{\mathrm{BLG}} - \mu_{\mathrm{Au,ref}}\ , (1)$$

where E_{cell} is the total energy of an $Na_0 \times Na_0$ bilayer graphene (BLG) supercell (which is used to approximate a graphite surface), containing a single Au adatom, ϵ_{BLG} is the energy of a single (4-atom) BLG unit cell, and $\mu_{\mathrm{Au,ref}}$ is a reference Au energy, which is taken as the energy of an isolated Au atom in a cubic cell of dimensions 20 Å × 20 Å. Au atoms were deposited on each of three distinct high-symmetry sites (A_1 – atop the carbon atom for the sublattice where there is another carbon immediately beneath it; A_2 – atop the carbon atom where there is no carbon in the layer directly beneath it; and H (hollow) – in the centre of the carbon hexagon), and subsequently fully relaxed to extract the corresponding DFT energy in the equilibrium geometry. The results are shown below, showing a significant preference for the A_1 and A_2 sites, in comparison to H, and with the hollow site as the energetic minimum for a single atom, with a small difference between A_1 and A_2 which reduces with decreasing cell size. Notably, there is a relatively flat energy dependence with increasing values of N.

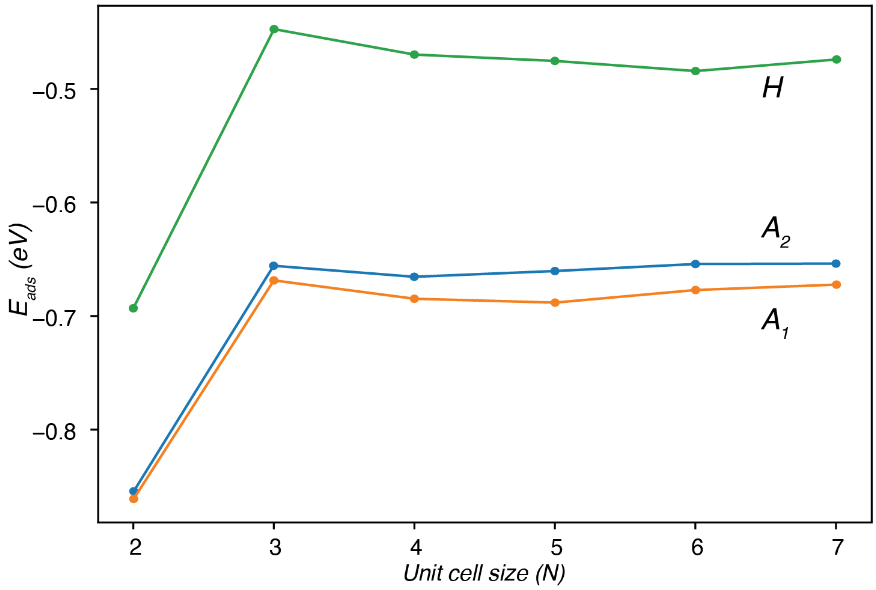

Figure S32: Single Au adatom adsorption energy vs cell size. *Adsorption energy E_{ads} (Eq. 1) vs cell size, N, at each of three high-symmetry sites on a BLG surface. Red and blue atoms are situated carbon atoms on the top and bottom layers, respectively.*

Bader charge analysis shows that, in contrast to alkali-metal decorated graphite surfaces there is very weak p-doping (~0.1 e^-/Au atom at all sites) of the graphite surface due to the large electronegativity of Au, suggesting relatively weak long-range Coulomb interactions between periodically-repeated Au adatoms. In the following we can therefore use an 8 × 8 cell to calculate the adsorption energy of pairs of Au atoms.

Bond breaking energy on BLG surface

The change in energy of an Au pair is taken as,

$$\Delta E = E_{\mathrm{pair}} - 2E_{ads} \ , (2)$$

where E_{ads} is the adsorption energy of an isolated Au atom on the dimer site and E_{pair} is the formation energy of the pair, (i.e., this is the cohesive or bond energy of the Au pair on BLG). This quantity was calculated using DFT, as a function of the in-plane distance between two Au atoms on the BLG surface. One Au atom fixed to an A_1 site while the second Au is moved along the zigzag direction, which crosses neighbouring double sites. Fig. S33 shows a plot of this energy vs Au-Au distance.

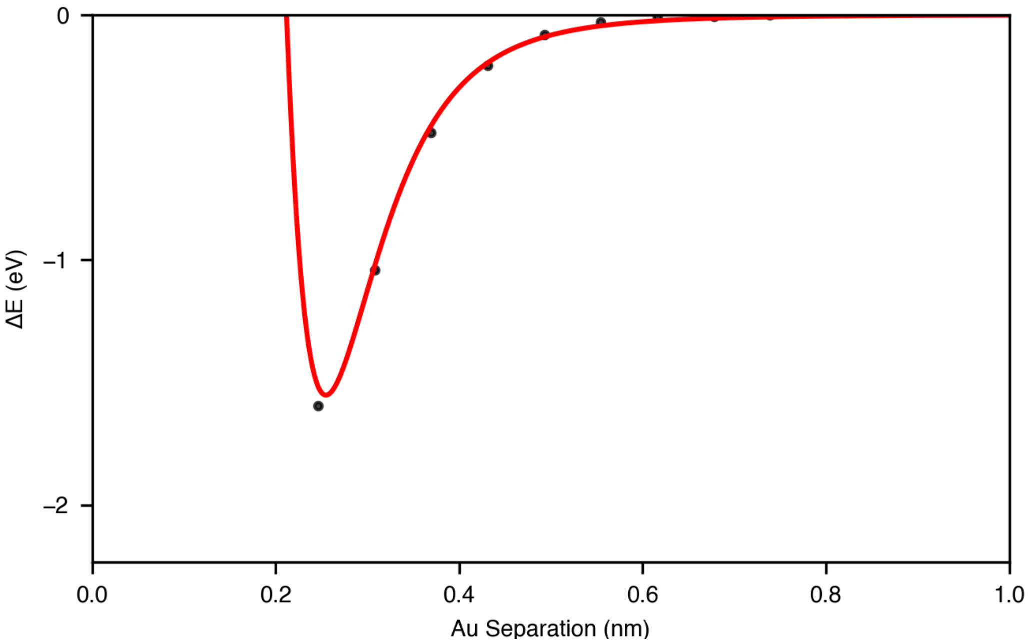

Figure S33: Energy potential as a function of Au-Au separation distance. *Values are plotted in black and the data has been fitted using Eq. 3 in red.*

This can be fitted using a Buckingham type potential,

$$\Delta E(r) = Ae^{-\alpha(r-r_0)} + Br^{-6} \ , (3)$$

with fitted values,

A (eV)	**B (eVÅ^6)**	**α (Å)**	**r_0 (Å)**
3.41097	-1300.90761	3.50217	2.53000

i.e., an exponential attractive term due to covalent bonding combined with short-range repulsion $\sim r^{-6}$. We note that the equilibrium Au-Au distance, for Au pairs which are oriented in-plane and out-of-plane are approximately commensurate with the BLG lattice (Au-Au distance ~2.48Å in all orientations). Bader analysis further confirms zero or very weak charge transfer to BLG, for Au pair positions close to the covalent bonds' minimum, suggestive of covalent Au-Au bonds.

Clustering

Subsequently, the clustering energy of pairs of Au atoms was calculated. This was taken as the difference in energy between a supercell containing both atoms, and twice the adsorption energy of an individual Au adatom at the corresponding cell size.

$$E_{\text{coh}} = E_{\text{cell}} - 2E_{ads}. \quad (4)$$

Au pairs were initially placed at each of two high-symmetry sites as shown in Fig. S34. One atom is placed at a given high-symmetry position, with another atom placed at neighbouring, high-symmetry sites at specified distances, resulting in three distinct relative positions for each of the three distances considered here. Calculated cohesive energies are shown in Table 1. In particular, we find that adsorption is most favourable when Au adatoms are closest together, for those positions there is significant Au-Au hybridization and subsequent tilting of one of the atoms out of the plane. At higher distances (where atoms may occupy the same high-symmetry sites), atoms remain largely flat after relaxation. Mutual occupation of pairs of closest double (A_1) sites, which are separated by one lattice spacing, is the overall lowest in energy, closely followed by Au atoms at top (A_2) sites, which is higher by ~0.6 meV per atom.

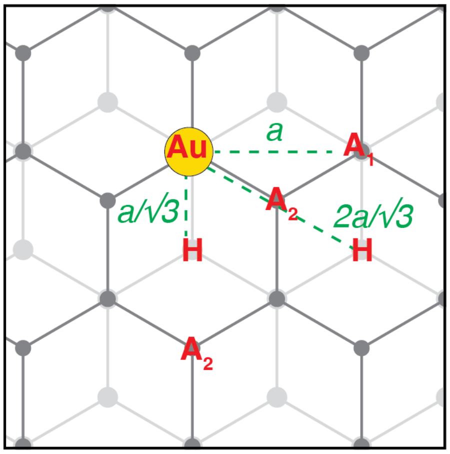

Figure S34: Au-Au adsorption sites. *Dark and light grey atoms are situated on the top and bottom layers, respectively. Pairs of Au atoms are initially placed on the BLG surface in an 8 x 8 supercell. One Au atom is placed on a high-symmetry site (A_2, A_1, H); the second Au atom is placed at neighbouring high-symmetry sites, which are situated at distances of* $\frac{\boldsymbol{a}}{\sqrt{3}}$, $\boldsymbol{a}$, *and* $\frac{2\boldsymbol{a}}{\sqrt{3}}$. *For the double site configurations shown here, these neighbours occupy A_2, H* ($\frac{\boldsymbol{a}}{\sqrt{3}}$)*, A_1* ($\boldsymbol{a}$)*, and A_2, H* ($\frac{2\boldsymbol{a}}{\sqrt{3}}$) *sites.*

Table 1: Au-Au adsorption energies at specified high-symmetry sites. *Sites are specified by the high-symmetry position of atoms 1 and 2 and the relative distance between pairs of atoms (see Fig. S34). At each site we calculate the relative distance (z_1, z_2) of each of the Au adatoms, the cohesive energy, E_{coh}, (i.e., bonding energy) of the Au pair and the relative energy difference between the A_1- A_1 configuration and others in meV. Mutual occupation of A_1 sites is preferred over all other flat configurations. This is also shown in Fig. S35.*

Site 1	Site 2	Distance	E_{coh}	z_1	z_2	ΔE (meV)
A_2	H	$a/\sqrt{3}$	-1.988	4.382	2.331	-419.871
A_2	A_1	$a/\sqrt{3}$	-1.971	4.396	2.341	-403.032
A_1	H	$a/\sqrt{3}$	-2.006	4.373	2.322	-438.130
A_2	A_2	a	-1.567	2.897	2.896	0.612
A_1	A_1	a	-1.568	2.897	2.897	0.000
H	H	a	-1.557	2.967	2.967	11.021
A_2	H	$2a/\sqrt{3}$	-1.168	2.880	2.720	400.107
A_2	A_1	$2a/\sqrt{3}$	-1.308	2.528	2.533	259.805
A_1	H	$2a/\sqrt{3}$	-1.165	2.927	2.746	402.530

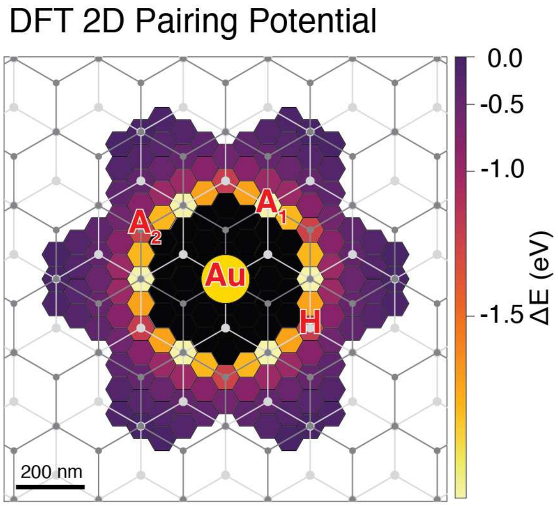

Figure S35: Au-Au adsorption energy. *Relative energy as a function of position for a pair of Au adatoms, with one atom fixed at the A_1 position, at a fixed distance above the BLG surface. Overlaid is a schematic of the BLG surface. Labels of the A_1: atop the carbon atom for the sublattice where there is another carbon immediately beneath it, A_2: atop the carbon atom for the sublattice where there is no carbon immediately beneath it, & H: hollow site.*

Finally, Fig. S35 shows the change in relative energy of the Au pair, as a function of the position of the second atom for both atoms at a fixed distance above the BLG surface. In this case, one Au atom is situated on the dimer sites, while the position of the second atom is varied across the BLG surface. Adsorption of the second Au adatom at an adjacent A_1 site is preferred over any other high-symmetry site when restricted to flat geometries.

7.2 DFT – Au, Graphite & Solvent Interactions

Adsorption of solvent (acetone, cyclohexanone, and water) molecules, single Au atoms and Au-solvent complexes on graphene was studied using DFT, using a single graphene layer as a model for FLG. The adsorption energies are shown in Table S2 and S3, and the optimised structures in Fig. S36.

The adsorption energies ΔE_{ads} of the solvent molecules, Au atoms and [Au(solvent)$_1$] complexes were calculated as:

$$\Delta E_{ads} = E(\mathrm{G+A}) - E(\mathrm{G}) - E(\mathrm{A}) \qquad (5)$$

where E(G+A) is the energy of graphene with adsorbate, E(G) is the energy of the isolated graphene sheet, and E(A) is the energy of the adsorbate (i.e. a single Au atom, a single solvent molecule, or an [Au(solvent)$_1$] complex).

The energies of solvent binding to Au adsorbed on graphene were calculated as:

$$\Delta E_{solv} = E(\mathrm{GAu+S}) - E(\mathrm{GAu}) - E(\mathrm{S}) \qquad (6)$$

where E(GAu+S) is the energy of graphene with an adsorbed Au atom and a co-adsorbed solvent molecule, E(GAu) is the energy of graphene with an adsorbed Au atom, and E(S) is the energy of an isolated solvent molecule.

Our DFT calculations show that a single Au atom adsorbs on graphene less strongly than acetone or cyclohexanone, but more strongly than water (Table S2). Therefore, in a water environment it is preferable to have Au atoms adsorbed on graphene than to have the graphene surface covered with water solvent. Table S2

However, [Au(acetone)$_1$] and [Au(cyclohexanone)$_1$] bind to graphene more strongly than single Au atoms or the solvent molecules alone, therefore solvated Au atoms are likely to adsorb on graphene. Moreover, acetone and cyclohexanone solvent molecules bind more strongly to adsorbed Au than to pure graphene. Therefore, adsorbed Au atoms or clusters are likely to be capped by solvent, providing some prevention against large crystal formation.

The acetone molecules can arrange in a more compact solvation shell around the adsorbed gold atoms compared to the cyclohexanone molecules, due to acetone's smaller size and smaller steric hindrance. This tighter packing is hypothesised to stabilise the small amorphous Au clusters in acetone more strongly than in cyclohexanone.

Table S2: Adsorption energy of single adsorbate on graphene.

System	**Adsorption Energy (eV)**
Au on graphene	-0.32
Water on graphene	-0.17
Acetone on graphene	-0.56
Cyclohexanone on graphene	-0.68

Table S3: Adsorption energy of Au atom and solvent on graphene.

System	**[Au(solvent)$_1$] complex binding to graphene (eV)**	**Solvent binding to graphene + Au (eV)**
Au + water on graphene	-0.44	-0.29
Au + acetone on graphene	-0.80	-0.72
Au + cyclohexanone on graphene	-0.92	-0.87

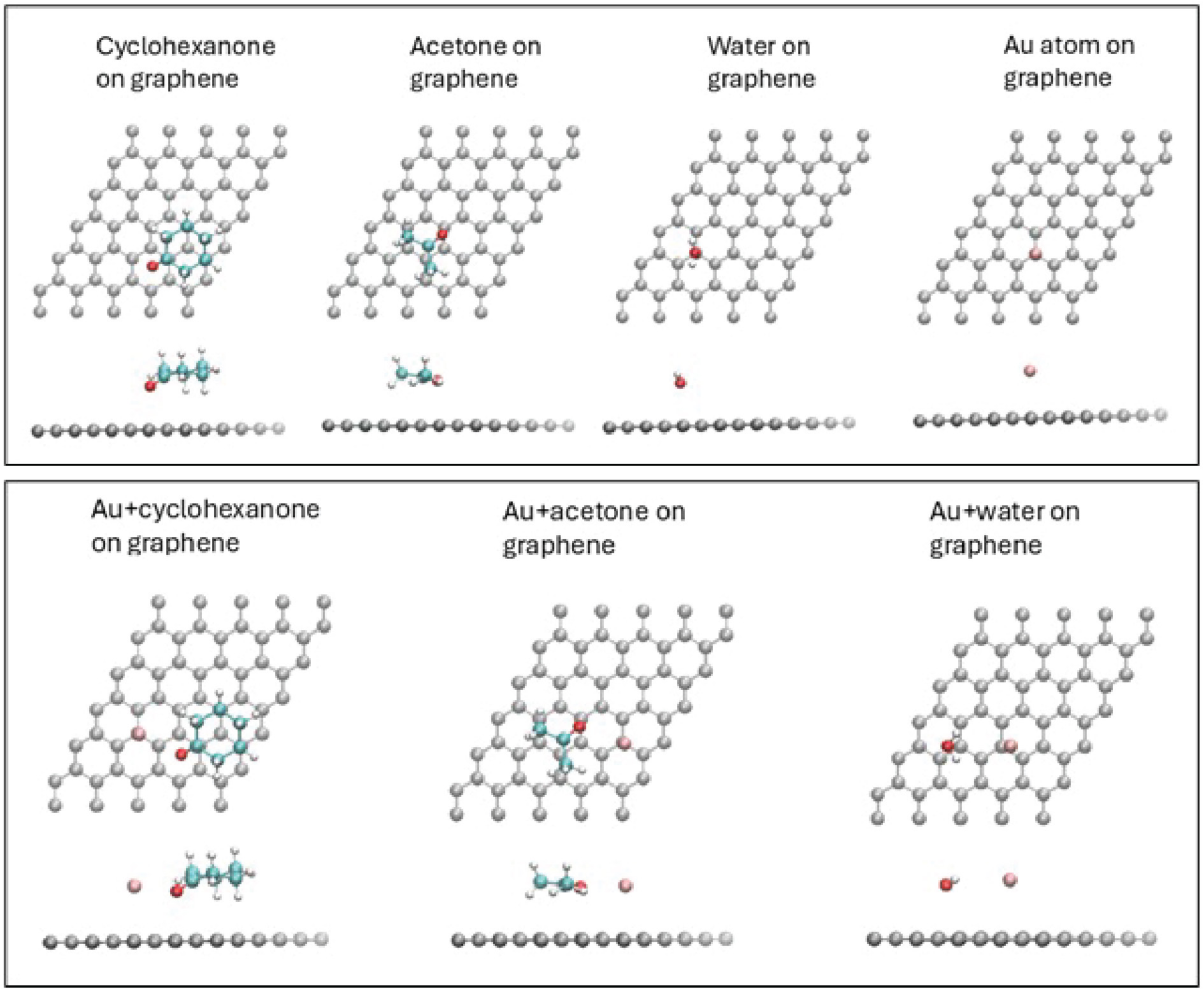

Figure S36: DFT calculation structures. *Upper panel: The structures of the single solvent molecules and single Au atom adsorbed on graphene used for the energy calculations in Table S2. Lower panel: The structures of the [Au(solvent)$_1$] complexes on graphene used for the energy calculations in Table S3. (Grey = carbon in graphene lattice, Blue = carbon in solvent molecule, red = oxygen, pink = gold).*

Additionally, the energies of solvent interaction with Au(I) and Au(III) ions were calculated in the implicit solvent environment, to investigate the possibility that the strength of solvation of Au ions in the solution phase is responsible for the observed differences in Au cluster sizes on graphene in different solvents.

The energies of binding of a solvent molecule to Au(I) (Table S4) were calculated as:

$$\Delta E = E(\mathrm{Au{+}S}) - E(\mathrm{Au}) - E(\mathrm{S}) \qquad (7)$$

where S stands for solvent, E(Au+S) is the energy of a [Au(I)(S)] complex, E(Au) is the energy of an Au(I) ion and E(S) is the energy of a solvent molecule.

The energies of replacing a Cl^- ligand in $[Au(I)Cl_2]^-$ and $[Au(III)Cl_4]^-$ complexes with a solvent molecule to form [Au(I)Cl(Solvent)] or $[Au(III)Cl_3(Solvent)]$ complexes (Table S5) were calculated as:

$$\Delta E = E(\mathrm{AuCl_nS}) + E(\mathrm{Cl}) - E(\mathrm{AuCl_{n+1}}) - E(\mathrm{S}) \qquad (8)$$

where S stands for solvent, n = 1 for Au(I) or n = 3 for Au(III), $E(\mathrm{AuCl_nS})$ is the energy of a [Au(I)Cl(S)] or $[Au(III)Cl_3(S)]$ complex, $E(\mathrm{AuCl_{n+1}})$ is the energy of a $[Au(I)Cl_2\text{-}]^-$ or $[Au(III)Cl_4]^-$ complex, E(Cl) is the energy of a Cl^- ion and E(S) is the energy of a solvent molecule.

The energies of dissociation of an AuCl species into Au^+ and Cl^- in the different solvent environments (Table S6) were calculated as:

$$\Delta E = E(\mathrm{AuCl}) - E(\mathrm{Au}) - E(\mathrm{Cl}) \qquad (9)$$

where E(AuCl), E(Au) and E(Cl) and the energies of AuCl, Au^+ and Cl^-, respectively. The energies of all species in equations (7-9) were calculated in the implicit solvent (acetone, cyclohexanone, or water) environment.

As shown in Tables S4-S6, the solvent binding energies, ligand replacement energies and energies of dissociation show no appreciable differences between the three solvents, hence this is unlikely to have a significant impact upon the atomic dispersion behaviour of the gold. Therefore, the primary reason for the different observed trends in Au cluster distributions is the difference in the strength of adsorption on graphene, rather than Au-solvent interactions in the solution phase.

Table S4: Binding energies of one solvent molecule to one Au(I).

Solvent	**Energy (eV)**
Cyclohexanone	-1.08
Acetone	-1.01
Water	-0.99

Table S5: Energy of replacing Cl in AuCl$_2^-$ or in AuCl$_4^-$ with solvent.

	Energy (eV)	
Solvent	**AuCl$_2^-$ + Solvent → [AuCl Solvent] + Cl$^-$**	**AuCl$_4^-$ + Solvent → [AuCl$_3$ Solvent] + Cl$^-$**
Cyclohexanone	0.86	0.97
Acetone	0.86	0.98
Water	0.73	0.90

Table S6: Energy of dissociating Au(I)Cl into Au$^+$ and Cl$^-$.

Solvent	**Energy (eV)**
Cyclohexanone	2.45
Acetone	2.39
Water	2.12

8. Thermogravimetric analysis

The samples for thermogravimetric analysis were prepared by dissolving $HAuCl_4$ salt in 1 mL of the solvent (acetone/cyclohexanone/water) to produce a 100 mM concentration and adding this to commercial graphite powder (~0.2 g). The samples were allowed to dry in ambient conditions for 2 days and then in a vacuum chamber for 7 days. A portion of each of these dried samples was taken for TGA analysis in the temperature range from room temperature to 500 °C. The temperature ramp rate was 10 °C min^{-1} under a nitrogen atmosphere. A reference sample was also measured consisting of a sample of the commercial graphite powder without any solution added. The result of the TGA is shown in Fig. S37. The much greater mass loss for the cyclohexanone exposed graphite compared to other solvents. and the controls, indicates the high level of adsorbed cyclohexanone left on the graphite even after drying. The mass change from the TGA experiment corresponds to the graphite powder having a surface coverage of over 100% prior to the heating.

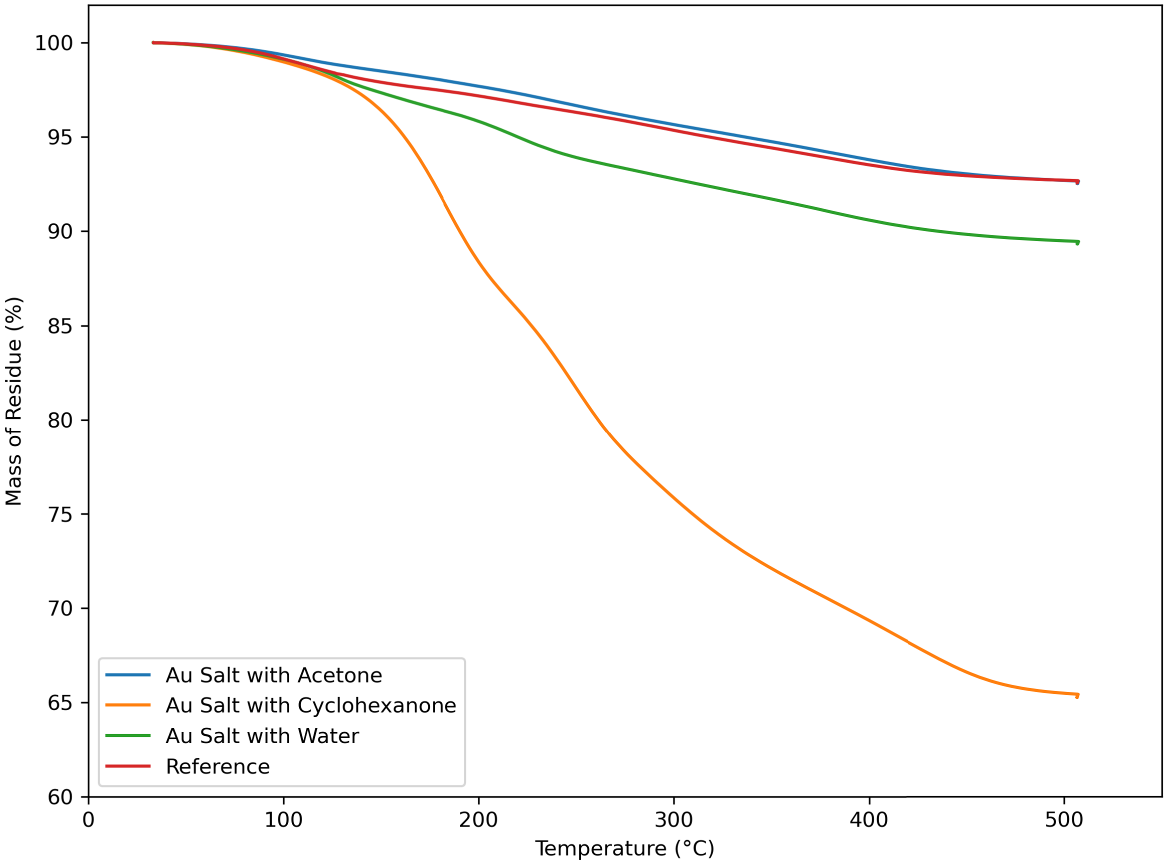

Figure S37: Thermogravimetric analysis. *Analysis of graphite powder exposed to gold salt dissolved in different solvents (acetone, cyclohexanone, and water). The reference sample is the commercial graphite powder which has not been exposed to solvents.*

9. Solvent Drying Effects

The gold salt ($HAuCl_4.3H_2O$) solution for each solvent was drop-cast on a Si substrate and allowed to dry at room temperature and under atmospheric conditions for 1 hour, before being placed into a vacuum chamber for an additional 1 hour, to ensure all the solvent had been removed. The substrates were then loaded into the SEM for the imaging of the patterns shown in Fig. S38.

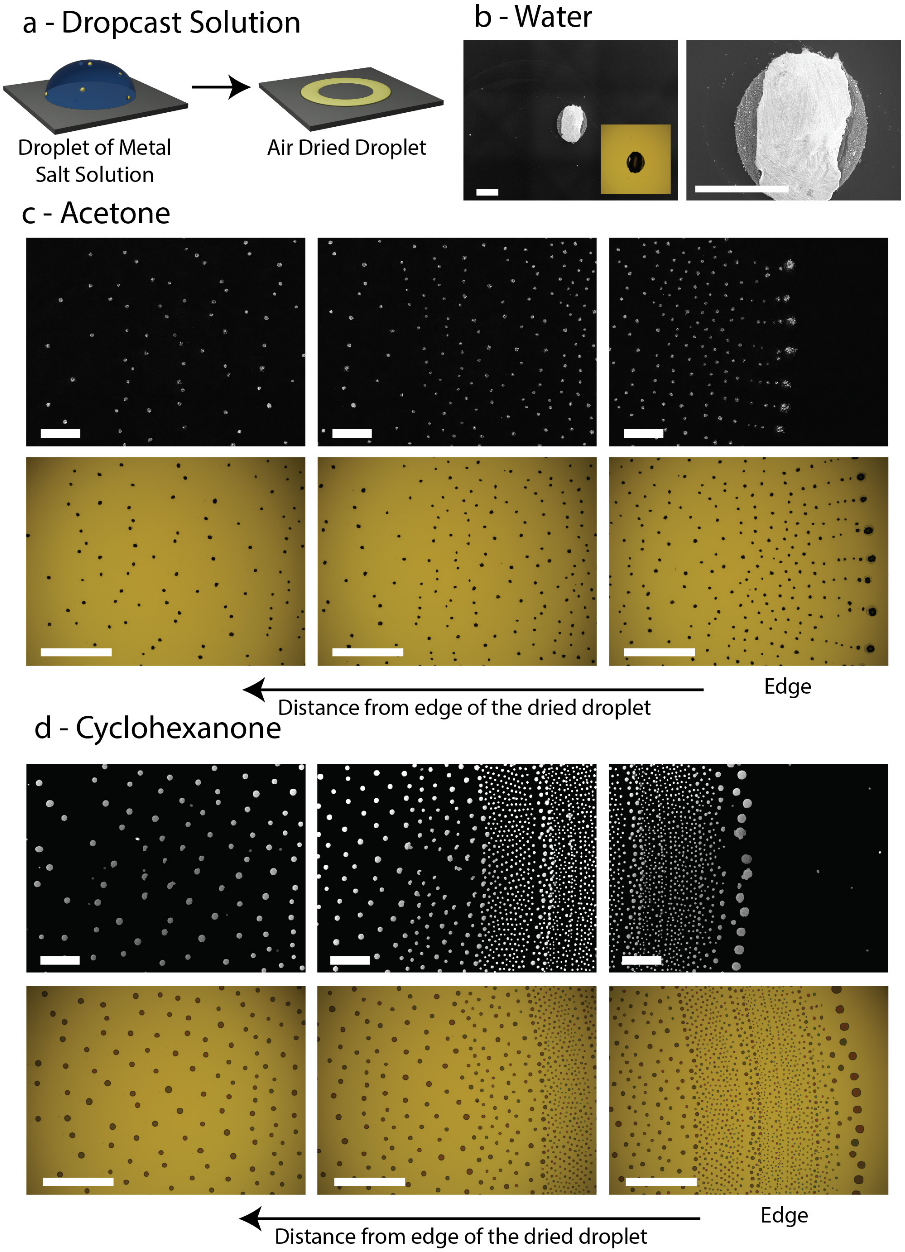

Figure S38: Images of the drying patterns left by the gold salt in the different solvents on a Si substrate. *(a) Schematic of the experimental set up. (b) SEM image of the pattern of dried salt produced from the water solution (inset shows an optical image). (c,d) The dried salt pattern from the acetone and cyclohexanone solutions, at varying distances from the centre of the dried droplet (SEM images top row, optical image bottom row). All the scalebars are 500 µm.*

10. Electron Beam Effects

Finally, we consider the effect of the electron beam on our results. The maximum typical energy that could be transferred from the electron probe to a gold adatom is 0.96 eV at 80 kV(*90*). The gold diffusion barriers on graphite in vacuum are low (0.02-0.05 eV(*49, 91*)) and although these are likely to be slightly higher in the presence of acetone or cyclohexanone adsorbed to the surface, energy transfer from the electron beam is likely contributing to the dynamic behaviour we observe. However, due to the relatively short acting nature of the electron beam, the dominant mechanics for adatom movement on graphite at room temperature is generally considered to be thermal excitation(*49*). Importantly, we see less dynamic motion in our dried controls compared to in the wet GLCs, suggesting the motion we observe at the solid-liquid interfaces is not purely electron beam induced. Furthermore, when acquiring 100s of images in the same cell we see no evolution in our systems, when considering either the adatom densities, distributions or dynamic motion (Fig. S23). This indicates that the experiments are at a steady, albeit excited, state within the first image frame. We appreciate that influence of electron beam can affect that equilibrium, but the presence of the grounded graphite layer in our system will provide the ability to continuously neutralise this non-equilibrium change. The exception to this stability is when the graphene window is significantly damaged or ruptured so that the liquid is lost, in which case the behaviour in the empty liquid cell closely resembles our vacuum phase data.

The rapidly achieved steady state (in a single frame) is not unexpected, as the concentration of electron beam generated radicals in pure water has been calculated to reach a steady state within milliseconds(*92*). The radiation induced changes in solution chemistry are much less well studied for organic systems and there are a large range of organic radical species that may be produced during irradiation with a high energy electron beam(*93*). Consequently, the radiation induced chemistry within the cell is challenging to define although the combination of the gold salt ($HAuCl_4.3H_2O$) and acetone solution with the electron beam irradiation is likely to produce a net oxidising environment(*94*) whereas in aqueous systems and vacuum conditions the electron beam is generally found to be reducing(*95, 96*). We see no bubble formation inside the liquid cells unless they are poorly sealed, for example due to a crease in the graphene window, which suggests that the hermetic sealing of the liquid cell may be supressing gas evolution(*32*) and helping to preserve the steady state conditions that allow prolonged imaging of the solid-liquid interface.

To further elucidate the impact of the electron beam on the behaviour of the gold adatoms we have performed an identical liquid cell experiment but with a significantly reduced electron flux (3.2 $x10^5$ e- $A^{-2}s^{-1}$ versus the 1.7 $x10^6$ e- $A^{-2}s^{-1}$ used in the original data). We then applied the same analysis and data processing to compare the effect of electron flux on jump distances in liquid and Au-Au atom pair distribution function (Fig. S39). We find no difference in the dynamics or pairing interactions. The flux values shown in Fig. S39 represent the full range of viable electron flux; higher values damage the graphene windows causing the liquid to escape, while lower values reduce the SNR for the cell so that it is not possible to confidently identify and track the Au atoms.

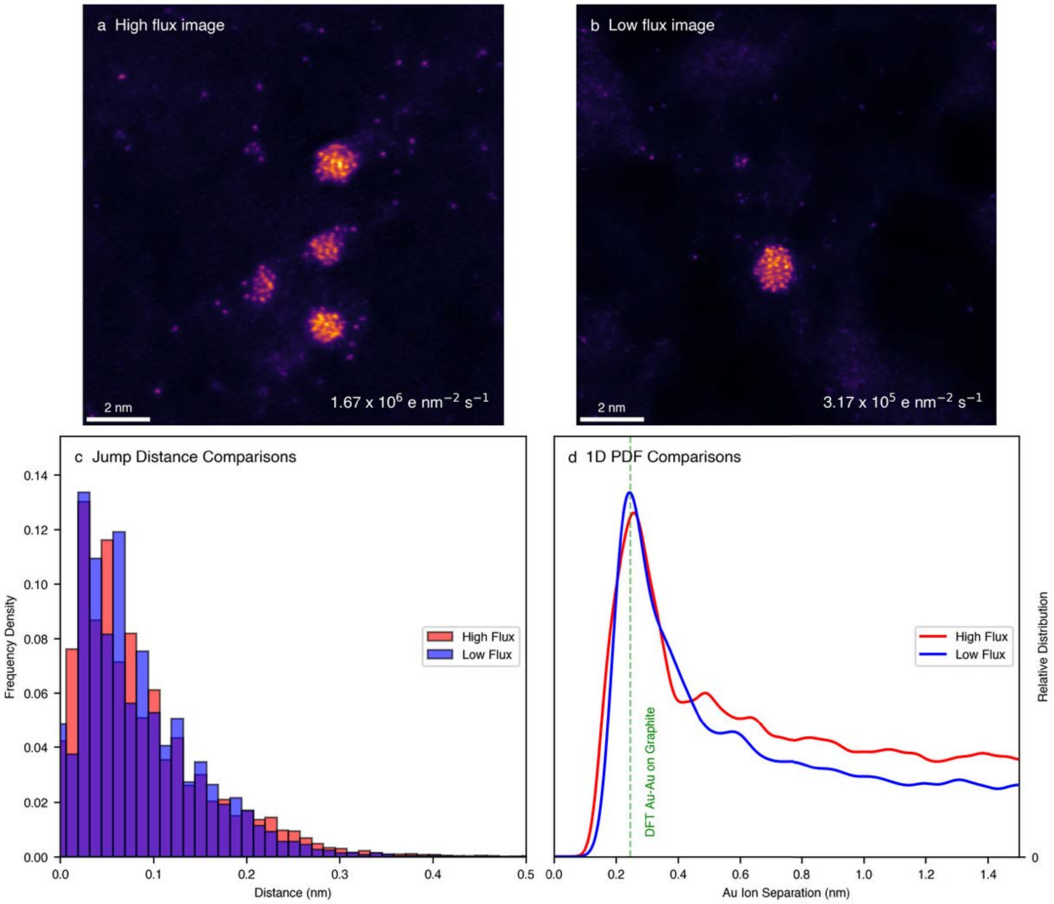

Figure S39: Electron flux dependency STEM experiment. *(a&b) Example denoised images from the high and low flux imaging conditions. The high flux is the typical imaging conditions that has been used within this work. When imaging above this electron flux damage to the GLC window was apparent. The atom tracking of the single frame jump distances (c) and the 1D pair distribution function (d) for the high and low electron flux.*